

DISSERTATION

A RESONANT ULTRASOUND SPECTROSCOPY STUDY OF  
NOVEL MATERIALS: NANOCRYSTALS, QUASICRYSTALS,  
AND HYDROGEN-STORAGE ALLOYS

Submitted by

Dennis Salvatore Agosta

Physics Department

In partial fulfillment of the requirements

for the degree of Doctor of Philosophy

Colorado State University

Fort Collins, Colorado

Summer 2006

UMI Number: 3233315

### INFORMATION TO USERS

The quality of this reproduction is dependent upon the quality of the copy submitted. Broken or indistinct print, colored or poor quality illustrations and photographs, print bleed-through, substandard margins, and improper alignment can adversely affect reproduction.

In the unlikely event that the author did not send a complete manuscript and there are missing pages, these will be noted. Also, if unauthorized copyright material had to be removed, a note will indicate the deletion.

**UMI**<sup>®</sup>

---

UMI Microform 3233315

Copyright 2006 by ProQuest Information and Learning Company.

All rights reserved. This microform edition is protected against unauthorized copying under Title 17, United States Code.

ProQuest Information and Learning Company  
300 North Zeeb Road  
P.O. Box 1346  
Ann Arbor, MI 48106-1346

COLORADO STATE UNIVERSITY

June 29, 2006

WE HEREBY RECOMMEND THAT THE DISSERTATION PREPARED UNDER OUR SUPERVISION BY DENNIS SALVATORE AGOSTA ENTITLED *A RESONANT ULTRASOUND SPECTROSCOPY STUDY OF NOVEL MATERIALS: NANOCRYSTALS, QUASICRYSTALS AND HYDROGEN-STORAGE ALLOYS* BE ACCEPTED AS FULFILLING IN PART REQUIREMENTS FOR THE DEGREE OF DOCTOR OF PHILOSOPHY.

Committee on Graduate Work

  
\_\_\_\_\_

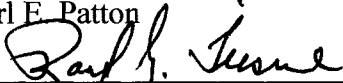
Martin P. Gelfand

  
\_\_\_\_\_

Paul R. Heyliger

  
\_\_\_\_\_

Carl E. Patton

  
\_\_\_\_\_

Adviser: Robert G. Leisure

  
\_\_\_\_\_

Department Chair: H. Dieter Hochheimer

## **ABSTRACT OF DISSERTATION**

### **A RESONANT ULTRASOUND SPECTROSCOPY STUDY OF NOVEL MATERIALS: NANOCRYSTALS, QUASICRYSTALS, AND HYDROGEN-STORAGE ALLOYS**

The experimental technique Resonant Ultrasound Spectroscopy (RUS) has been used to study the elastic properties and ultrasonic loss of several novel materials: a nanocrystalline form of palladium, a quasicrystal, a Laves phase C15 cubic material that undergoes a Martensitic phase transition when cooled, and a random alloy.

Resonant Ultrasound Spectroscopy (RUS) is an ideal technique for the characterization of the elastic properties of these types of materials since RUS is non-destructive and can work with very small sample sizes. The RUS technique is also sensitive to ultrasonic loss, and these measurements provide information on internal mechanisms that dissipate energy such as the movement of light interstitial atoms or the movement of dislocations.

Nanocrystalline materials have average grain sizes of 100 nm or less. The reduced grain size leads to physical properties that are different than the properties of the coarser grained forms of the same chemical composition, and many of these properties are the basis of new technological advances. The elastic constants of nanocrystalline palladium (nc-Pd) and silicon-stabilized nanocrystalline palladium (nc-PdSi) were measured in the temperature range 4-300K. The measured bulk

modulus for nc-Pd is 35.1-40.0% lower than corresponding values calculated for polycrystalline Pd. The measured shear modulus is 17.8-18.6% lower than pc-Pd. The elastic moduli for nc-Pd exhibit significant anelastic effects, while the elastic moduli for nc-PdSi do not. A loss peak centered near 264 K in nc-Pd is suppressed in nc-PdSi, indicating the loss mechanisms are due to grain boundary effects.

Quasicrystals are materials with an aperiodic structure, but which display perfect long-range order. While periodic crystalline structures can only display 2-fold, 3-fold, 4-fold and 6-fold rotational symmetries, quasicrystals display 5-fold, 8-fold, 10-fold and 12-fold rotational symmetries. RUS was used to measure the elastic constants of an icosahedral  $\text{Ti}_{39.5}\text{Zr}_{39.5}\text{Ni}_{21}$  quasicrystal over the temperature range 3-292K. The results were in general agreement with earlier ultrasonically-derived values for *i*-phase  $\text{Ti}_{41.5}\text{Zr}_{41.5}\text{Ni}_{17}$ . In comparison to many other *i*-phase materials, the ultrasonic measurements show that the TiZrNi materials have a low shear modulus to bulk modulus ratio, and a high Poisson's ratio, suggesting that the interatomic bonding in the TiZrNi materials differs substantially from that in many of the other *i*-phase materials. A Debye temperature of 316.7 K was calculated from the low-temperature elastic constants, and the internal friction increases rather strongly in the temperature range of 150 – 300 K, suggestive of a thermally activated process.

Laves-phase alloys are the largest subgroup of the topologically close-packed materials, and are characterized by low densities and high melting points. The Laves-phase C15 (cubic) materials can absorb hydrogen, making them useful in battery and fuel cell technologies. The temperature dependence of the elastic constants of polycrystalline  $\text{ZrV}_2$  was measured in the temperature range 100-300 K using the

RUS technique. The elastic constants exhibit anomalous behavior over this temperature range, and the lack of hysteresis in the temperature dependence of the resonant frequencies provides evidence that the phase transition from the C15 cubic to rhombohedral form is second-order. Ultrasonic loss was measured for the first resonant frequency and displays a peak centered at the transition temperature,  $T_m$ . Calculations of the Debye temperature using room temperature elastic constants agree well with results published by earlier studies.

Random alloys are metallic compounds which do not exhibit chemical ordering of their component atoms; any lattice position may be inhabited by any of the chemical species comprising the compound. The random alloy discussed in this study,  $Ta_{0.33}V_{0.67}$ , can absorb considerable amounts of hydrogen and the disordered nature of the local atomic environments leads to differences in the elastic properties. In this study, the temperature dependence and ultrasonic loss for a random alloy with the same chemical composition as the Laves-phase C15  $TaV_2$  compound was measured in the temperature range 5-300 K using the RUS technique, and compared to an earlier study of  $TaV_2$ . The temperature dependence of the bulk modulus of bcc  $Ta_{0.33}V_{0.67}$  exhibits strong agreement with the semi-empirical Varshni expression, while the shear modulus and Young's modulus deviate significantly from this theoretical curve. Laves-phase C15  $TaV_2$  also exhibits an anomalous temperature dependence of  $G$  and  $E$ , but where  $TaV_2$  exhibits a decreasing modulus with decreasing temperature, bcc  $Ta_{0.33}V_{0.67}$  exhibits an increasing modulus with decreasing temperature. The electronic effects which strongly impact the  $C_{44}$  elastic constant in C15  $TaV_2$  are highly suppressed in the random alloy form, resulting in a

temperature dependence of the shear and Young's moduli that are only slightly anomalous and which display a more normal behavior. Ultrasonic loss associated with the movements of hydrogen atoms between interstitial tetrahedral sites is observed for bcc  $\text{Ta}_{0.33}\text{V}_{0.67}\text{H}_{0.045}$  in the 170 K temperature region, and is not observed for bcc  $\text{Ta}_{0.33}\text{V}_{0.67}$ .

Dennis Salvatore Agosta  
Physics Department  
Colorado State University  
Fort Collins, CO 80523  
Summer 2006

## Acknowledgements

I would like to express my gratitude for the help and support of a number of people in the Physics Department at Colorado State University. First I need to thank the Graduate Admissions Committee for giving an unconventional student an opportunity to pursue his dream. Thank you to Marty Gelfand, Paul Heyliger and Carl Patton for serving on my committee. I also want to thank Richard Eykholt, Sandy Kern, Sui Au Lee, and Steve Robinson for always being available to answer my questions and providing advice and support in my graduate student career and in my job search. A student couldn't ask for a better advisor than Bob Leisure. His knowledge of condensed matter physics is awe-inspiring, and I credit his patience and guidance as the major reason that I've been able to accomplish what appears in this dissertation.

I would also like thank our collaborators who provided the materials used to make the samples for this study. Alexander Skripov provided the random alloy and the initial samples of  $ZrV_2$ , Ken Kelton provided the quasicrystal, and Keir Foster provided the nanocrystal and the  $ZrV_2$ .

I have been very fortunate to be able to interact with other graduate students who have accepted me as one of the group despite the differences in our ages. Jennifer Atteberry, Elijah Flenner, Tony Gorges, Sangita Kalarickal, Anitra Novy, Travis Olson, Kevin Smith, and Erica Snow are all people I count among my friends,

and I hope we'll stay in touch as time and distance separate us. A special thank you is extended to Jennifer for setting the high standard of excellence to which I tried to adhere .

On the non-academic side of my life, I want to thank Dave Duke, Greg Northrup, and Jim and Vickie Worthen for providing me the opportunity to relocate to Colorado and for being true friends who are always there when I need them. My parents Joseph and Theresa Agosta raised three sons in a moral and loving atmosphere, and no gratitude that I can express will ever be enough to thank them for what they've done for me. I would also like to thank my children, Eileen and Doug, for their support. They never complained about their father as a student on the same campus where they were pursuing their studies.

Finally, none of this would have been possible without the love and support of my wife Bernadette. When life became stressful, she urged me to make a change, and my decision to return to school was accepted with enthusiasm despite the added burden she had to shoulder in supporting the family. I hope she agrees that the rewards are worth the struggle.

# Contents

## Chapter 1: Introduction

1.1 Motivation for Study .....	1
1.2 Elasticity .....	5
1.3 Ultrasonic Loss .....	13
References .....	15

## Chapter 2: Experimental Details

2.1 Introduction .....	16
2.2 Resonant Ultrasound Spectroscopy .....	17
2.3 Sample Preparation .....	21
2.4 Measurements .....	26
2.5 Analysis .....	31
References .....	38

## Chapter 3: $\text{Ti}_{39.5}\text{Zr}_{39.5}\text{Ni}_{21}$ *i*-phase Quasicrystal

3.1 Introduction .....	39
3.2 Experimental Details .....	43
3.3 Results and Discussion .....	45
3.4 Conclusions .....	54
References .....	56

<b>Chapter 4: Nanocrystalline Palladium (nc-Pd)</b>	
4.1 Introduction .....	58
4.2 Experimental Details .....	60
4.3 Results and Discussion .....	61
4.4 Conclusions .....	71
References .....	72
<b>Chapter 5: bcc Ta<sub>0.33</sub>V<sub>0.67</sub> Random Alloy</b>	
5.1 Introduction .....	73
5.2 Experimental Details .....	75
5.3 Results and Discussion .....	75
5.4 Conclusions .....	85
References .....	86
<b>Chapter 6: ZrV<sub>2</sub></b>	
6.1 Introduction .....	88
6.2 Experimental Details .....	92
6.3 Results and Discussion .....	93
6.4 Conclusions .....	102
References .....	103
<b>Chapter 7: Conclusions</b> .....	104
<b>Appendix 1: Derivation of the Modulus Defect</b> .....	109
<b>Appendix 2: Isotropy of <i>i</i>-phase Quasicrystals</b> .....	114
<b>Appendix 3: Transducer Assembly Construction</b> .....	117

# Chapter 1

## Introduction

- 1.1 Motivation for study
- 1.2 Elasticity
- 1.3 Ultrasonic loss
- References

### 1.1 Motivation for study

The elastic and attenuation properties of the materials studied for this dissertation were measured using the technique of Resonant Ultrasound Spectroscopy (RUS)<sup>1</sup>. This experimental technique is described in Chapter 2. The elastic properties of a material, as characterized by the elastic constants, are directly related to the atomic structure of the material. As the second derivative of the free energy with respect to strain, the elastic constants are related to the interatomic potentials and equations of state. The thermal properties of a material are linked to the elastic constants through the Debye theory, and thermodynamic quantities such as specific heat, thermal expansion, Debye temperature and Grüneisen's constants are also related to the elastic constants. Elastic properties are also useful in measuring the characteristics of phase transitions<sup>2,3</sup>. In a perfectly harmonic crystal, the elastic constants would not depend upon temperature. In a real crystal, anharmonic terms in the interatomic potentials cause frequency changes in the various lattice vibration

modes due to the amplitude of the strain. The temperature dependence of the elastic constants is therefore related to the anharmonicity of the crystal <sup>4,5</sup>.

A perfect crystal, displaying perfectly elastic properties, will not exhibit internal friction. When external stress is applied to a real crystal, mechanisms such as ferromagnetic effects and dislocation movement will lead to energy loss. In addition, anelastic relaxation effects such as thermoelasticity, stress relaxation across grain boundaries, movement of interstitial atoms and stress-induced ordering will lead to a portion of the elastic strain response to be out of phase with the stress. This time difference between stress and strain response causes the conversion of ultrasonic vibrational energy into thermal energy of the lattice, resulting in ultrasonic loss <sup>6</sup>. The RUS technique is sensitive to some of these loss mechanisms and is valuable in probing their details.

This dissertation deals with the study of elastic constants and ultrasonic loss of several novel materials: a nanocrystalline form of palladium, a quasicrystal, a Laves phase C15 cubic material that undergoes a Martensitic phase transition when cooled, and a random alloy. Many unusual materials such as quasicrystals and nanocrystals are difficult to produce and the raw material used to fabricate samples is often received in small quantities. Resonant Ultrasound Spectroscopy (RUS) is an ideal technique for the characterization of the elastic properties of these types of materials since RUS is non-destructive and can work with very small samples. Some of the samples produced for this study have dimensions on the order of several tenths of a millimeter, and produced excellent data sets when processed with the RUS technique.

Nanocrystalline materials have average grain sizes of 100 nm or less. The reduced grain size leads to physical properties that are different than the properties of the coarser grained forms of the same chemical composition, and many of these properties are the basis of new technological advances. Nanocrystalline films, nanocrystalline particles and bulk nanocrystals have possible applications in medical technologies, solar energy applications, computer processor technology and enhanced strength materials to name a few <sup>7</sup>. The determination of the elastic constants of nanocrystalline materials, and their dependence on temperature, are an important contribution to the understanding of the properties of these materials, and RUS is an ideal technique for measuring these quantities because of its ability to work with samples of very small size.

Quasicrystals are materials with an aperiodic structure, but which display perfect long-range order. While periodic crystalline structures can only display 2-fold, 3-fold, 4-fold and 6-fold rotational symmetries, quasicrystals display 5-fold, 8-fold, 10-fold and 12-fold rotational symmetries. Quasicrystals can absorb considerable amounts of hydrogen, making them useful in battery and fuel cell technology, and also have thermoelectric properties with possible application to power generation, cooling and computer processors <sup>8,9,10,11</sup>. As in the case of nanocrystals, RUS is an ideal experimental technique for determining the temperature dependence of the elastic constants and details of the ultrasonic loss in quasicrystals because these materials are difficult to make resulting in very small sample sizes.

Laves-phase alloys are the largest subgroup of the topologically close-packed (TCP) materials, and are characterized by low densities and high melting points.

Laves-phase compounds are formed in three crystalline forms: C14 (hexagonal), C15 (cubic) and C36 (mixed). The C15 materials can absorb hydrogen, making them useful in battery and fuel cell technologies. Some Laves-phase C15 materials, such as  $\text{TaV}_2$  and  $\text{ZrV}_2$ , show an anomalous temperature dependence of their elastic constants; others, such as  $\text{ZrV}_2$  and  $\text{HfV}_2$  undergo Martensitic phase transitions when cooled; some of these compounds are superconducting at the appropriate temperature (for example,  $\text{ZrV}_2$  at about 8 K). In addition to their hydrogen absorption capabilities, some of these compounds that undergo phase transitions also exhibit the properties of shape memory alloys. The RUS technique is suitable for probing the details of the phase transition in these materials, both through measurement of the softening of the shear modes as the transition temperature is approached and through analysis of the ultrasonic loss curves.

Random alloys are metallic compounds which do not exhibit chemical ordering of their component atoms; any lattice position may be inhabited by any of the chemical species comprising the compound. The random alloy discussed in this study,  $\text{Ta}_{0.33}\text{V}_{0.67}$ , can absorb considerable amounts of hydrogen, and actually can absorb more hydrogen per formula unit than the ordered forms of the same chemical composition,  $\text{TaV}_2$ . The disordered nature of the local atomic environments leads to differences in the elastic properties. In this study, the temperature dependence and ultrasonic loss for a random alloy with the same chemical composition as the Laves-phase C15  $\text{TaV}_2$  compound was measured using the RUS technique, and compared to an earlier study of  $\text{TaV}_2$ .

## 1.2 Elasticity

An important characteristic of matter in the solid form is that, left undisturbed, a solid retains its shape. Under the influence of forces (pressures), that are not strong enough to permanently deform the solid body, a solid will deform and the deformation will be resisted by internal forces. If we define *stress* as the force per unit area acting on a solid body and *strain* as the fractional displacement (i.e.,

$\varepsilon_i = \frac{\partial u_i}{\partial x_i}$  where for the  $i^{\text{th}}$  direction,  $\varepsilon_i$  is the strain and  $u_i$  is the displacement from

equilibrium, giving the degree of deformation), then the stress is proportional to the strain (Hooke's Law) for small strains. Hooke's Law may also be extended to include liquids.

In one dimension, Hooke's Law is given by

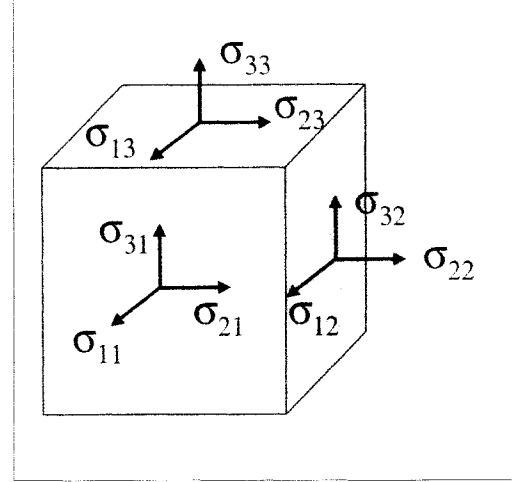
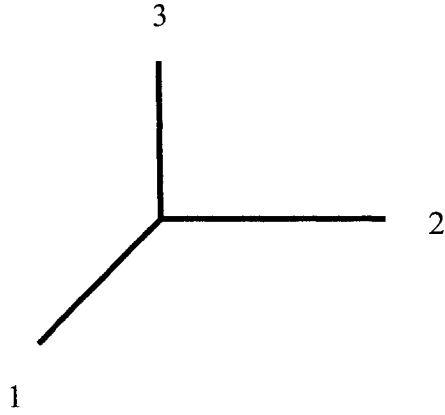
$$\sigma = C\varepsilon \quad (1)$$

where  $\sigma$  is the applied stress,  $\varepsilon$  is the resulting strain, and  $C$  is an elastic constant.

Equation 1 is valid under the following conditions: <sup>5</sup>

1. The strain response to the applied stress has a unique equilibrium value, and the response is completely recoverable upon removal of the stress.
2. The equilibrium response is instantaneous.
3. The response is linear.

We can extend Hooke's Law to three dimensions. Defining a Cartesian coordinate system



equation 1 becomes

$$\sigma_{ij} = \sum_{kl} C_{ijkl} \varepsilon_{kl} \quad (2)$$

The stress tensor  $\sigma_{ij}$  represents the force in the  $i$  direction on a unit area with normal in the  $j$  direction.  $C_{ijkl}$  the complete set of elastic constants and is represented by a 4<sup>th</sup> rank tensor. The strain tensor is given by

$$\varepsilon_{kl} = \frac{1}{2} \left[ \frac{\partial u_k}{\partial x_l} + \frac{\partial u_l}{\partial x_k} \right] \quad (3)$$

where  $u_k$  is the displacement from equilibrium <sup>12</sup>.

The elastic constant tensor has 81 elements. If  $\sigma_{ij}$  is not equal to  $\sigma_{ji}$ , there is a net torque on the solid body and the body will rotate. The conditions  $\sigma_{ij} = \sigma_{ji}$  and  $\varepsilon_{ij} = \varepsilon_{ji}$  reduces the number of stress components from nine to six, the strains are reduced to three compressional strains ( $\varepsilon_{11}, \varepsilon_{22}, \varepsilon_{33}$ ) and three shear strains ( $\varepsilon_{12}, \varepsilon_{23}, \varepsilon_{31}$ ), and the elastic constant tensor elements from 81 to 36 <sup>13</sup>. If  $U$  is the internal energy acquired by the solid due to the work done by the external stresses, and if the process is assumed to be isothermal or reversible adiabatic, then

$$\sigma_{ij} = \frac{\partial U}{\partial \varepsilon_{ij}} = \sum_{kl} C_{ijkl} \varepsilon_{kl} \quad (4)$$

and

$$\frac{\partial^2 U}{\partial \varepsilon_{ij} \partial \varepsilon_{kl}} = \frac{\partial^2 U}{\partial \varepsilon_{kl} \partial \varepsilon_{ij}} = C_{ijkl} = C_{klij} \quad (5)$$

which shows that the elastic constant tensor is symmetric and in general only 21 independent elastic constants are required for an anisotropic material <sup>14</sup>.

The elastic constants are usually represented with a reduced subscript notation: 11 ↔ 1 22 ↔ 2 33 ↔ 3 23=32 ↔ 4 13=31 ↔ 5 12=21 ↔ 6 <sup>12</sup>.

Using this notation, the elastic constant tensor for the least symmetric of the seven crystal systems, triclinic, can be represented by the matrix

$$C_{triclinic} = \begin{pmatrix} C_{11} & C_{12} & C_{13} & C_{14} & C_{15} & C_{16} \\ C_{12} & C_{22} & C_{23} & C_{24} & C_{25} & C_{26} \\ C_{13} & C_{23} & C_{33} & C_{34} & C_{35} & C_{36} \\ C_{14} & C_{24} & C_{34} & C_{44} & C_{45} & C_{46} \\ C_{15} & C_{25} & C_{35} & C_{45} & C_{55} & C_{56} \\ C_{16} & C_{26} & C_{36} & C_{46} & C_{56} & C_{66} \end{pmatrix} \quad (6)$$

For crystal systems with higher symmetries, the number of independent elastic constants is reduced. Crystals with monoclinic symmetry, 13 independent elastic constants are required, with  $C_{15}=C_{16}=C_{25}=C_{26}=C_{35}=C_{36}=C_{45}=C_{46}=0$ . Orthorhombic symmetry requires 9 independent elastic constants, with  $C_{orthorhombic}$  differing from  $C_{monoclinic}$  by  $C_{14}=C_{24}=0$ . Trigonal and tetragonal systems require 6 or 7 independent elastic constants, with the elements depending upon the symmetry point group. Hexagonal symmetries require 5 independent elastic constants, with  $C_{44}=C_{55}$ ,  $C_{13}=C_{23}$ ,  $C_{11}=C_{22}$ , and  $C_{66}=\frac{1}{2}(C_{11}-C_{12})$ . The highest crystal symmetry, cubic, requires

3 independent elastic constants with  $C_{11}=C_{22}=C_{33}$ ,  $C_{44}=C_{55}=C_{66}$ , and  $C_{12}=C_{13}$ . For elastically isotropic materials, 2 independent elastic constants are required with  $C_{11}=C_{22}=C_{33}=C_{44}=C_{55}=C_{66}$ ,  $C_{44}=\frac{1}{2}(C_{11}-C_{12})$ , and  $C_{12}=C_{13}$ <sup>13</sup>. In an elastically isotropic material, compression stresses will only produce compression strains and shear stresses will only produce shear strains<sup>12, 14</sup>. Some polycrystalline materials are elastically isotropic. A polycrystal is composed of microscopic crystallites, each with the same periodic crystal structure. The crystallites in a polycrystal may be randomly oriented, or may have a preferred orientation (textured materials). In the case of randomly oriented polycrystals, the microscopic crystallites produce crystalline axes that vary over all possible orientations, and this isotropic averaging leads to elastically isotropic behavior<sup>4</sup>.

Quantities that describe the elastic properties of solids may be calculated from the elastic constants. The experimental results reported in this dissertation are for materials which are either polycrystalline or quasicrystalline. The quasicrystalline materials studied for this thesis have randomly oriented crystallites like a polycrystal, but the individual crystallites are composed of aperiodic structures. Quasicrystals display rotational symmetries that are forbidden to normal crystal structures, but are elastically isotropic (see Appendix 2). The discussion that follows pertains to elastically isotropic materials unless indicated otherwise. The elastic properties of these materials have been characterized by the shear modulus ( $G$ ), the bulk modulus ( $B$ ), Young's modulus ( $E$ ), and Poisson's ratio ( $\nu$ ).

The shear modulus, illustrated in Fig. 1.1, describes the stiffness of a solid to forces that do not change its volume.

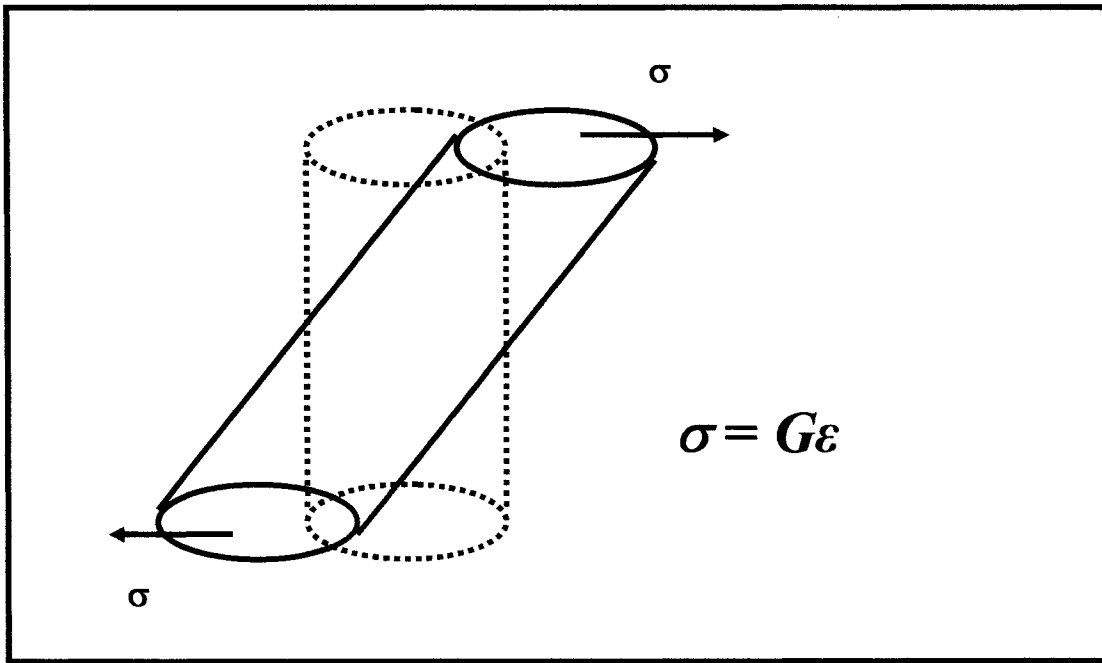


Fig. 1.1 Illustration of the shear modulus,  $G$ , where  $\sigma$  is the stress and  $\epsilon$  is the strain. It is assumed that the object is clamped in such a way as to prevent rotation.

For cubic crystal lattice symmetry, two shear moduli exist and are given by

$$G_1 = \frac{1}{2}(C_{11} - C_{12}) \quad \text{and} \quad G_2 = C_{44} \quad (7)$$

For elastically isotropic materials, only one shear modulus exists,  $G_1 = G_2 = G = C_{44}$ .

The difference between  $G_1$  and  $G_2$  in two dimensions is illustrated in Fig. 1.2. Note that in the case of  $G_2$ , both a simple shear and a pure shear can be defined. A simple shear plus a rotation can produce the same deformation as the pure shear.

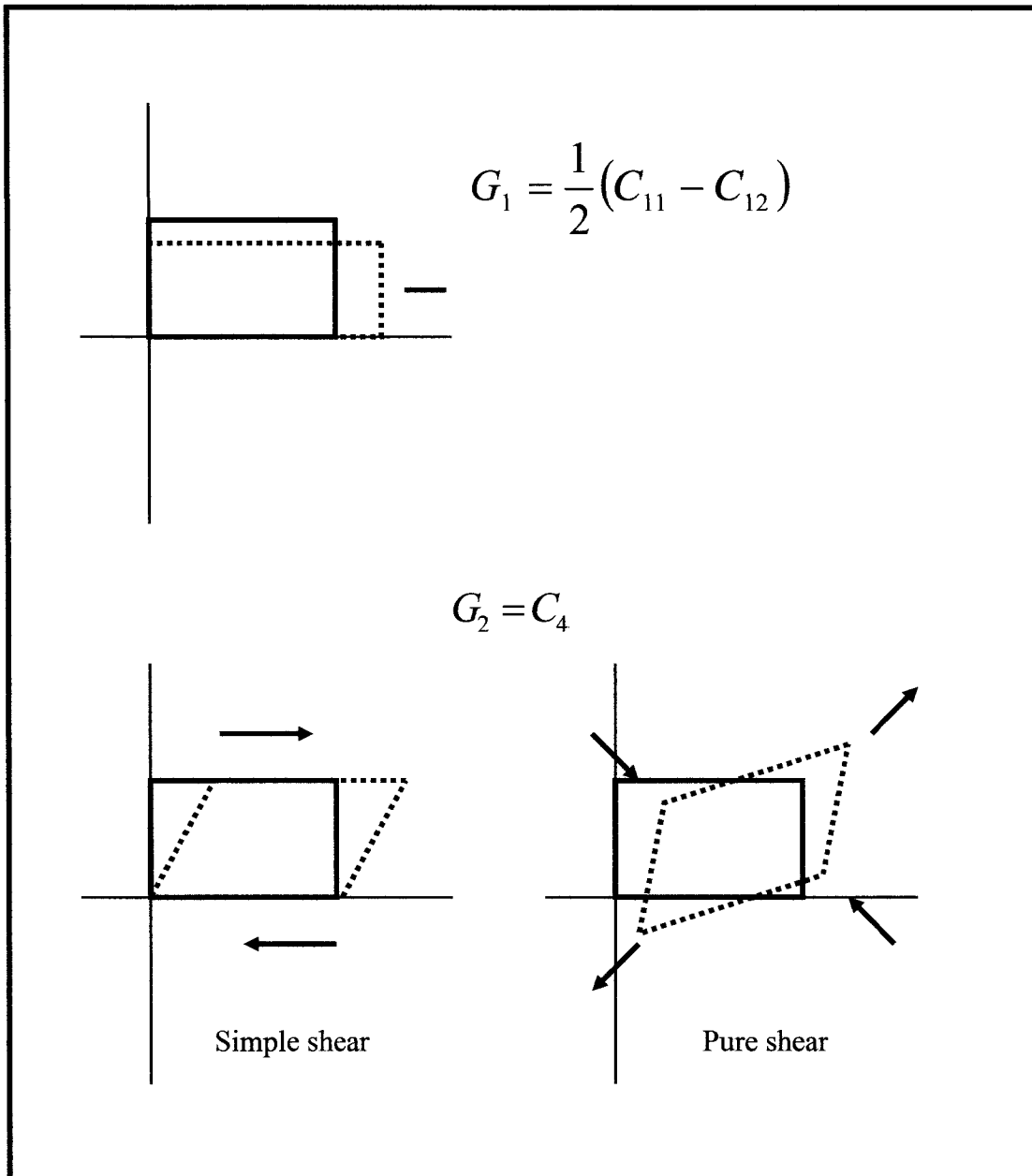


Fig. 1.2 Shear modulus in two dimensions. The solid arrows indicate the direction of the applied stress. Rotating the result of the pure shear will give exactly the same deformation as the simple shear.

The bulk modulus, illustrated in Fig. 1.3, describes the resistance of a solid to volume changes.

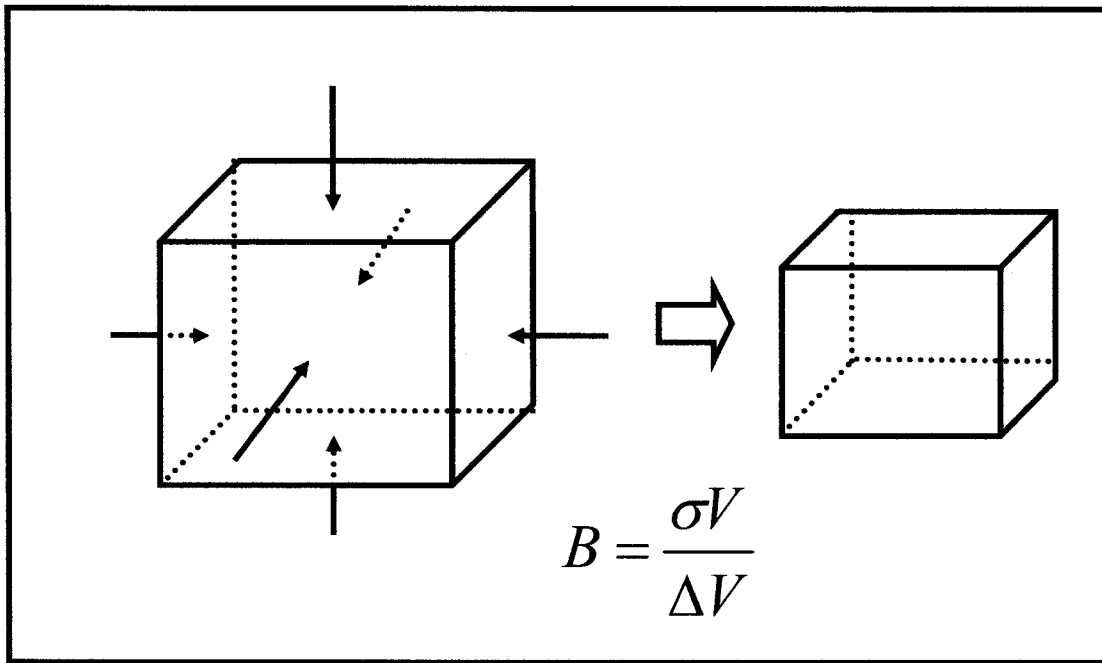


Fig. 1.3 Illustration of the bulk modulus,  $B$ , where  $\sigma$  is the stress and  $V$  is the volume. For an isotropic material,

$$B = \frac{1}{3}(C_{11} + 4C_{44}) \quad (8)$$

Young's modulus, illustrated in Fig. 1.4, is the ratio of the stress along an axis of the material to the accompanying strain along that axis.

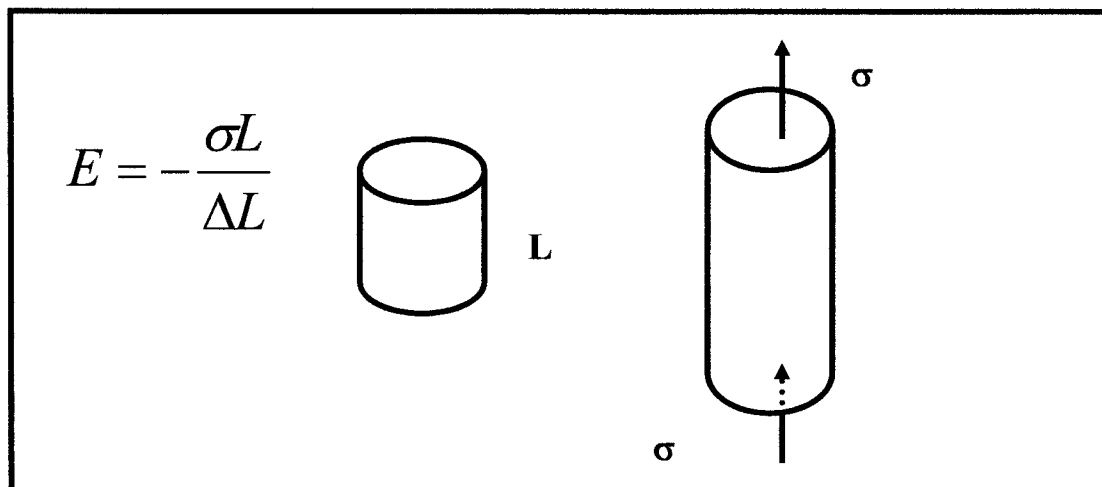


Fig. 1.4 Illustration of Young's modulus,  $E$ , where  $\sigma$  is the stress and  $L$  is the length.

Young's modulus for isotropic materials is calculated from the elastic constants using

$$E = C_{44} \frac{(3C_{11} - 4C_{44})}{(C_{11} - C_{44})} \quad (9)$$

Poisson's ratio, illustrated in Fig. 1.5, is the ratio of the transverse to the longitudinal normal strains produced by a stress along the longitudinal axis.

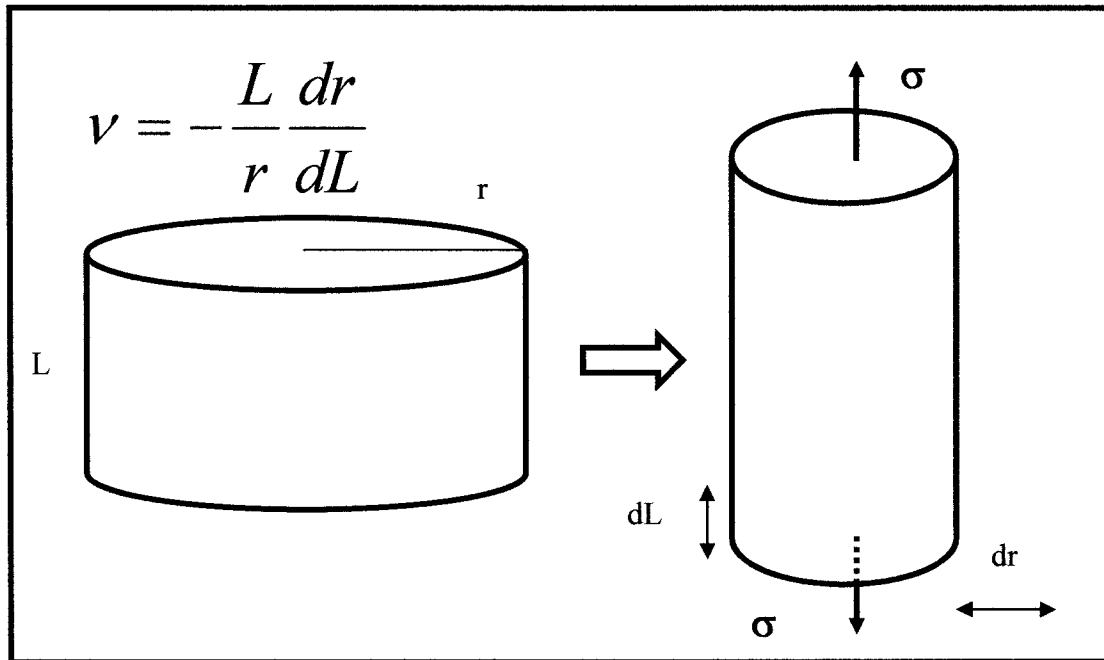


Fig. 1.5 Illustration of Poisson's ratio,  $\nu$ , where  $r$  is the undeformed radius and  $L$  is the undeformed length.

Poisson's ratio for an isotropic material is calculated from the elastic constants using

$$\nu = \frac{C_{11} - 2C_{44}}{2(C_{11} - C_{44})} \quad (10)$$

In the perfect crystal, the strain reacts instantaneously to the stress. In a real material this condition must be modified to include a time dependent anelastic response in addition to the elastic (instantaneous) response. This condition combined with the unique equilibrium value of strain in response to stress and the linearity of

the response defines anelasticity. The modulus defect is defined as the change in the elastic moduli due to anelasticity, and is derived in Appendix 1.

### 1.3 Ultrasonic loss

Vibrations applied to a real material will attenuate over time due to internal processes which dissipate energy. The movement of dislocations, phase changes, superconductivity and ferromagnetic effects are processes which will produce ultrasonic loss. Anelastic relaxation can occur when a time-dependent stress produces strains which affect neighboring interstitial sites differently. Light atoms such as hydrogen which occupy interstitial sites will move to sites with lower energy, producing loss. RUS measures both elastic constants and ultrasonic loss through the analysis of the resonant vibrations of solid bodies.

We can introduce loss into the equation of motion for the driven, damped oscillator by defining a complex force constant,  $k^* = k_1 + ik_2$ . The equation of motion is

$$m \frac{d^2x}{dt^2} + k^* x = F(t) = F_0 e^{i\omega t} \quad (11)$$

where  $m$  is the mass,  $x$  is the displacement from equilibrium, and  $F(t)$  is the applied driving force. The solution to the homogeneous equation is

$$x = x_0 e^{i(\omega t - \theta)} \quad (12)$$

where  $x_0$  is the equilibrium position and  $\theta$  is a phase shift. Substituting Eq. (12) into Eq. (11) and setting  $k_2$  and  $F(t)$  equal to zero, yields the undamped resonant frequency,

$$\omega_0 = \sqrt{\frac{k_1}{m}} \quad (13)$$

Substitution of Eq. (12) and Eq. (13) into Eq. (11) results in

$$x_0 = \frac{F_0}{m \left[ (\omega_0^2 - \omega^2)^2 - \left( \frac{k_2}{m} \right)^2 \right]^{1/2}} \quad (14)$$

and

$$\theta = \tan^{-1} \left[ \frac{k_2/m}{(\omega_0^2 - \omega^2)} \right] \quad (15)$$

Loss is expressed as  $Q^{-1}$ , where  $Q$  is the quality factor defined as the width of the resonant line shape at the half power points, and calculated from

$$Q = \frac{\omega_0}{\Delta\omega} \quad (16)$$

It can now be shown from Eq. (13), Eq. (16) and the definition of the half power point that

$$Q^{-1} = \frac{k_2}{k_1} \quad (17)$$

The extension of the theory of elasticity to include an anelastic component results in a complex form for the elastic constants (see Appendix 1). Using Eq. (17), we can write the loss in terms of the elastic constants (Debye-time relaxation function) as

$$Q^{-1} = \frac{\Delta c}{c} \frac{\omega\tau}{1 + \omega^2\tau^2} \quad (18)$$

where  $\tau$  is a relaxation time,  $c_U$  is an unrelaxed elastic constant (the elastic constant in the  $\omega\tau \gg 1$  region),  $c_R$  is a relaxed elastic constant (the elastic constant in the  $\omega\tau \ll 1$  region),

$\Delta c = c_U - c_R$ , and  $\Delta c/c$  is called the relaxation strength.  $Q^{-1}$  approaches zero in the limits  $\omega\tau \ll 1$  and  $\omega\tau \gg 1$ , and is a maximum for  $\omega\tau = 1$ .

## References

- 
- <sup>1</sup> A. Migliori, J.L. Sarrao, W.M. Visscher, T.M. Bell, M. Lei, Z. Fisk, R.G. Leisure, *Physica B* **183** 1 (1993).
  - <sup>2</sup> R.G. Leisure and F.A. Willis, *J. Phys.: Condens. Matter*, **9**, 6001-6029 (1997).
  - <sup>3</sup> J. Maynard, *Physics Today*, January 1996, 26-31.
  - <sup>4</sup> N.W. Ashcroft and N.D. Mermin, *Solid State Physics*, 489 (Saunders, Philadelphia, 1976).
  - <sup>5</sup> A.S. Nowick and B.S. Berry, *Anelastic Relaxation in Crystalline Solids*, 510-511 (Academic Press, New York, 1972).
  - <sup>6</sup> A.S. Nowick in *Progress in Metal Physics*, vol. 4, B. Chalmers. ed. (Pergamon Press LTD, London, 1953).
  - <sup>7</sup> <http://www.e-drexler.com/>
  - <sup>8</sup> R.M. Stroud, A.M. Viano, P.C. Gibbons, K.F. Kelton, S.T. Mixture, *Appl. Phys. Lett.* **69** (20), 2998 (1996).
  - <sup>9</sup> P.C. Gibbons, R.G. Henning, V.T. Huett, K.F. Kelton, *J. Non-Cryst. Solids* **334&335**, 461-465 (2004).
  - <sup>10</sup> T.M. Tritt, M.L. Wilson, A.L. Johnson, S. LeGault, R. Stroud, 16<sup>th</sup> Int. Conf. on Thermoelectrics (1997).
  - <sup>11</sup> Y.K. Kuo, J.R. Lai, C.H. Huang, C.S. Lue, S.T. Lin, *J. Phys.: Condens. Matter* **15**, 7555-7561 (2003).
  - <sup>12</sup> A. Migliori, J.L. Sarrao, *Resonant Ultrasound Spectroscopy*, (Wiley, New York, 1997).
  - <sup>13</sup> M. Levy in *Handbook of elastic properties of solids, liquids, and gases*, Vol. II, M. Levy, H.E. Bass, and R.R. Stern, eds. (Academic Press, San Diego, 2001), Chapter 1.
  - <sup>14</sup> A.S. Saada, *Elasticity Theory and Applications*, (Pergamon Press Inc., New York, 1974).

## **Chapter 2**

### **Experimental details**

- 2.1 Introduction
- 2.2 Resonant Ultrasound Spectroscopy
- 2.3 Sample preparation
- 2.4 Measurements
- 2.5 Analysis
- References

#### **2.1 Introduction**

The elastic constants of materials studied for this dissertation were measured using the technique of Resonant Ultrasound Spectroscopy (RUS)<sup>1,2</sup>. In the RUS technique, a sample of known geometry, dimensions and density is mounted between two transducers. A signal generator vibrates one transducer, sweeping through an interval of frequencies in the 0.5-3.0 MHz range, and the resulting vibrations of the sample are detected by the second transducer. A set of normal mode frequencies is measured, and a figure of merit is formulated and minimized from the measured resonant frequencies and the expected frequencies calculated from the initial elastic constants, dimensions, density and geometry of the sample<sup>3</sup>. The RUS technique yields highly accurate results for the complete elastic constant tensor from a single set

of measurements. RUS spectra are also useful for measuring ultrasonic loss (internal friction),  $Q^{-1}$  <sup>2,3</sup>.

The samples used in this study were cooled in a commercial cryostat for measurements below room temperature. Temperature control was accomplished using a Lake Shore temperature controller, with temperature measurements made with a silicon diode. A commercial spectrometer was used for signal generation and detection.

## **2.2 Resonant Ultrasound Spectroscopy**

The Resonant Ultrasound Spectroscopy technique is an experimental method that is able to determine the complete set of elastic constants of a crystalline material, by exciting and detecting the vibrational eigenmode frequencies of a sample of known density and dimensions. RUS is an improvement over earlier techniques which involved time of flight measurements of sound pulses to determine sound velocities in materials, because RUS does not need to reorient or cement the sample to the transducers and can perform its measurements in a single run on samples of very small size. An early form of the technique was used by geophysicists analyzing seismic data to determine the structure and composition of the interior of the Earth. Improvements to the technique produced the Resonant Sphere Technique (RST), which was used to determine sound velocities and Poisson's ratio for glass spheres in lunar rock samples from the Apollo 11 mission <sup>4</sup>.

The problem of directly determining the elastic constants from the density, dimensions, geometry and resonant frequencies has never been solved analytically

(with the exception of the isotropic sphere). The problem that has been solved is the calculation of the resonant frequencies from the density, dimensions, geometry and elastic constants. This problem was first solved by Gabriel Lamé and Horace Lamb around 1880 for isotropic, noncrystalline cubes and spheres. In 1971, Harold Demarest extended the solution set to include anisotropic, crystalline parallelepipeds and isotropic crystalline spheres (Rectangular Parallelepiped Resonance (RPR) method). In 1976, Ichiro Ohno published extensions to Demarest's work to include lower crystalline symmetries<sup>5</sup>. The experimental techniques were refined, and the calculations made feasible through the development of computer algorithms, by Albert Migliori and William M. Visscher in 1988, producing the technique currently in use, Resonant Ultrasound Spectroscopy<sup>3,5</sup>.

Most of the samples investigated with RUS are parallelepipeds because they are the easiest to produce and don't suffer from degeneracy of resonant frequencies. Cylindrical and spherical samples are also used. Following the development in reference 3, the algorithm for calculating the vibrational eigenmodes is developed from Hamilton's principle, which requires that the free vibrations of an elastic solid will result in a stationary Lagrangian<sup>6</sup>. The Lagrangian for the elastic energy of an arbitrarily shaped elastic solid is given by

$$L = \int_V (KE - PE) dV \quad (1)$$

where  $KE$  is the kinetic energy,  $PE$  is the potential energy and  $V$  is the volume of the solid that is bounded by the surface  $S$ . For a sample vibrating with an angular frequency  $\omega$ ,

$$KE = \frac{1}{2} \sum_{i=1}^3 \rho \omega^2 u_i^2 \quad (2)$$

and

$$PE = \frac{1}{2} \sum_{i,j,k,l} C_{ijkl} \frac{\partial u_i}{\partial x_j} \frac{\partial u_k}{\partial x_l} \quad (3)$$

where  $\rho$  is the density,  $u_i$  is the displacement from equilibrium,  $C_{ijkl}$  is the elastic constant tensor, and  $x_1, x_2$  and  $x_3$  are the Cartesian coordinates. The displacement vector is assumed to have a harmonic time dependence given by  $u(t) = u_0 e^{i\omega t}$ .

We apply the technique of the calculus of variations to find the minimum of the Lagrangian by letting  $u$  vary arbitrarily in  $V$  and on  $S$ .

$$L + \delta L = \int_V \frac{1}{2} \left[ \sum_i \rho \omega^2 (u_i + \delta u_i)^2 - \sum_{ijkl} C_{ijkl} \frac{\partial (u_i + \delta u_i)}{\partial x_j} \frac{\partial (u_k + \delta u_k)}{\partial x_l} \right] dV \quad (4)$$

Expanding terms and keeping terms that are first order in  $\delta u_i$  yields

$$\delta L = \int_V \left[ \sum_i \rho \omega^2 u_i \delta u_i - \sum_{ijkl} C_{ijkl} \frac{\partial (\delta u_i)}{\partial x_j} \frac{\partial u_k}{\partial x_l} \right] dV \quad (5)$$

Integrating by parts and transforming the second volume integral into a surface integral gives

$$\delta L = \int_V \left[ \sum_i \rho \omega^2 u_i \delta u_i + \sum_{ijkl} C_{ijkl} \frac{\partial^2 u_k}{\partial x_j \partial x_l} \delta u_i \right] dV - \int_S \sum_{ijkl} \vec{n}_j C_{ijkl} \frac{\partial u_k}{\partial x_l} \delta u_i dS \quad (6)$$

The condition that the Lagrangian is stationary,  $\delta L = 0$ , implies that the integrands for the volume integral and the surface integral must each be equal to zero. The volume integral yields the elastic wave equation

$$\rho \omega^2 u_i + \sum_{jkl} C_{ijkl} \frac{\partial^2 u_k}{\partial x_j \partial x_l} = 0 \quad (7)$$

and the surface integral gives the free-surface boundary conditions

$$\sum_{jkl} \vec{n}_j C_{ijkl} \frac{\partial u_k}{\partial x_l} = \sum_j \vec{n}_j \sigma_{ij} = 0 \quad (8)$$

where  $\sigma_{ij}$  is a component of the stress tensor and  $\vec{n}_j$  is a unit vector normal to the surface.

The Rayleigh-Ritz method is used to expand the displacement vectors in a complete set of functions. In the current implementation, powers of the Cartesian coordinates are used as the set of functions.

$$u_i = \sum_{lmn} a_{lmn} x^l y^m z^n \quad (9)$$

This expansion is combined with the Lagrangian to form an eigenvalue problem in which the resonant frequencies are the eigenvalues.

The symmetry of the Lagrangian must have the same symmetry as the geometry and elastic constant matrix of the sample. For a parallelepiped, there are three intersecting mirror planes perpendicular to the Cartesian coordinate axes. This allows us to split the matrix representations of the components of the eigenvalue problem into eight smaller matrices to facilitate computations. The splitting operation is based upon the symmetries of the displacement vector,  $\mathbf{u}$ , with respect to the mirror planes, and each of these smaller matrices corresponds to a vibrational mode of the parallelepiped<sup>6,7</sup>. Figure 2.1 illustrates a symmetric displacement and an antisymmetric displacement.

Since the problem of determining elastic constants from measured frequencies is not solvable directly, an indirect method is required. In RUS, a set of resonant frequencies for a sample is measured. A set of predicted resonant frequencies is then

calculated from the sample density, dimensions, geometry, crystal symmetry and estimated values for the elastic constants. A nonlinear optimization method is then applied to find the set of elastic constants that is in the best agreement with the measured resonant frequencies <sup>3</sup>. A figure of merit,  $F$ , is formed from the measured frequencies,  $f_m$ , and the calculated frequencies,  $f_c$ ,

$$F = \sum_{i=1}^N w_i (f_c - f_m)^2 \quad (10)$$

where  $w_i$  is a weighting factor and  $N$  is the number of frequencies measured. The Levenberg-Marquardt algorithm is then applied to minimize  $F$ .

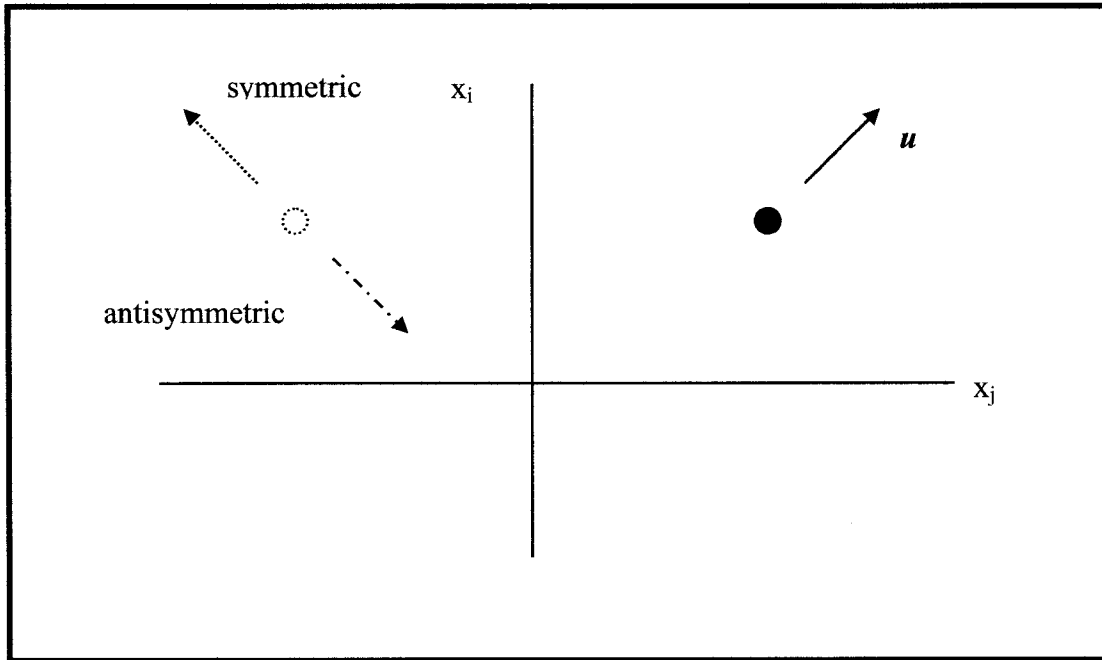


Fig. 2.1 A symmetric and an antisymmetric response to a displacement  $u$ .

### 2.3 Sample preparation

The materials studied in the Ultrasonics Laboratory at Colorado State University are obtained through collaborations with labs in Los Alamos, St. Louis, Russia, Israel, and Germany. The raw materials arrive in various forms: small

ingots, cylinders, thin disks, and irregular shapes. Lattice parameters and crystal structure have usually been determined by X-ray diffraction or other means prior to being shipped to Colorado State University.

The initial step in sample preparation is to form a rough parallelepiped by cutting the material on a low speed diamond saw. In theory, the RUS technique should be able to handle any sample geometry. In practice, spheres, cylinders and parallelepipeds have been successfully used, with parallelepipeds the preferred shape due to ease of preparation of accurate samples and elimination of resonance degeneracy due to sample symmetries. The material to be cut is cemented to an aluminum block with mounting wax that is melted on a hot plate. The minimum requirement from this step is a single flat surface on the rough parallelepiped. This is sufficient to insure that a polished sample with parallel and perpendicular sides can be produced, although if a pair of parallel cuts can be made on the saw, the polishing step is easier. Most materials are cut using a high density diamond saw blade, although brittle materials require the use of a low density blade. The saw blade is kept cool during the cutting process with water-based coolant or oil. The dimensions of the rough sample are measured with a micrometer.

The next step is to hand polish the rough sample into a highly accurate parallelepiped. Assuming a single flat surface, the rough sample is placed on an optical flat and a set of four shims of identical thickness are set against the sample sides, in a specific pattern as illustrated by figure 2.2.



Fig. 2.2 RUS sample mounted on optical flat. The first sample side has been hand polished to the level of the supporting shims.

The shim/sample assembly is held in place with mounting wax, and the sample is wet polished by hand with polishing disks of varying grit size and distilled water. After the first side is polished, the optical flat is placed on the hot plate to melt the mounting wax, the sample is rotated 180° and a shim set of slightly smaller thickness is used so that the polished face is flat on the optical flat surface and the unpolished face protrudes past the shim level. This insures that the second polished face is parallel to the first. The sample is remounted for the polishing the third face in such a way that the shims are flat against the two existing polished faces, regardless of how the sample sits on the optical flat. This will insure that the third polished face is perpendicular to the first two polished faces. The fourth face is polished in the same

manner as the second face. The fifth and sixth faces are polished with all four shims flat against the sample.

The completed sample is cleaned by baths of acetone, alcohol and distilled water to remove all traces of dirt and mounting wax. The sample is examined under a microscope to insure that large flaws do not exist. Flat corners, deep scratches or pits on edges will have a measurable impact on the accuracy on the RUS measurements. Significant flaws require re-polishing of the affected sides.

The mass of the completed sample is measured on a highly accurate electronic scale. Between 12 and 15 measurements are made and averaged to arrive at the mass parameter used in the analysis, and these values are used in the error analysis. The linear dimensions of the sample are measured on a micrometer, and as with the mass, 12 to 15 measurements of each dimension are made and averaged.

Some materials require special handling in the sample preparation process. The nanocrystalline samples discussed in this dissertation were stored in liquid nitrogen to suppress grain growth when not in use. In addition, grain growth would have occurred if the normal process of heating the optical flat and mounting wax was used. To prevent this, several room temperature adhesives were tested for the gluing of samples and shims to the optical flat. Elmer's library paste was selected as the best of those adhesives that were tested. The mounted shim/sample assembly required 2-4 hours of drying time for each polished face, as compared to 15 minutes per face to cool the mounting wax for a "normal" material. Since the room temperature adhesives were water soluble, the initial polishing steps were done without distilled water using moderate grit polishing disks. The final polishing was completed with

3  $\mu\text{m}$  diamond paste spread on aluminum foil; the foil was flattened on an oiled, granite block to provide a flat polishing surface.

The quasicrystal samples were very brittle and it was not possible to obtain clean saw cuts. Polishing was performed using very fine grit polishing disks, and the diamond paste used for the nanocrystals was also used here. The nanocrystals and quasicrystals which I worked with arrived as very thin disks. These disks were thinner than the thinnest shim in our polishing set and purchasing new shims was not feasible due to their high cost. I was able to extend the shim set to smaller thicknesses (0.1 – 0.6 mm) by cutting inexpensive gage strips in the Physics Department shop. The resulting sample size was very small as illustrated in Fig. 2.3.

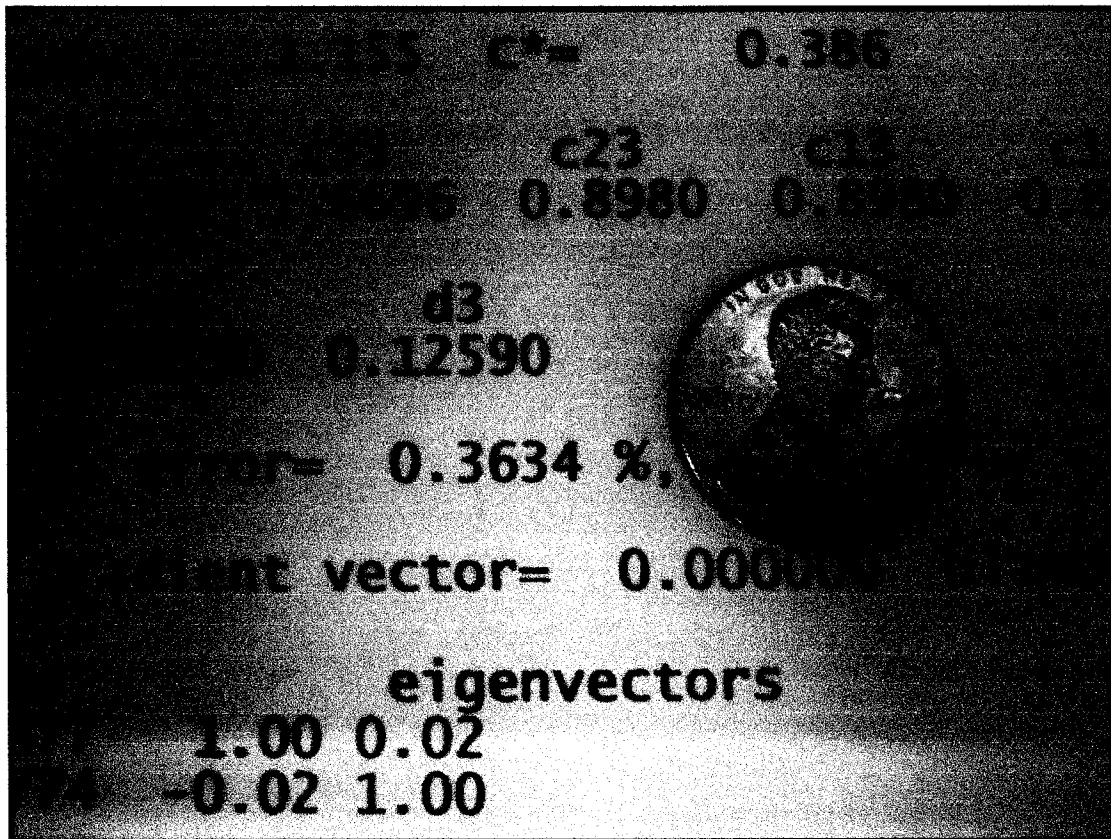


Fig. 2.3 A finished sample of nanocrystalline Pd. The dimensions of the sample on the penny are 0.51mm x 0.13 mm x 0.10 mm.

## 2.4 Measurements

The resonances measured by RUS are modeled as a damped, driven oscillator.

$$m \frac{d^2x}{dt^2} + 2b \frac{dx}{dt} + kx = F e^{-i(\omega t + \theta)} \quad (11)$$

where  $k$  is a “spring” constant,  $b$  is a damping factor,  $m$  is the mass,  $F$  is the driving force and  $\theta$  is a phase shift. The solution to the undamped, homogeneous equation (steady state solution) is

$$x(t) = x_0 e^{-i\omega t} \quad (12)$$

and the resonant frequency is given by

$$\omega_0 = \sqrt{\frac{k}{m}} \quad (13)$$

From reference 3

$$\frac{1}{Q} = \frac{2b}{m\omega_0} \quad (14)$$

Substituting equations (12), (13) and (14) into equation (11) yields

$$x_0 = \frac{\left(\frac{F}{m}\right) e^{-i\theta}}{\left(\omega_0^2 - \omega^2\right) - \frac{i\omega\omega_0}{Q}} \quad (15)$$

Equation (15) is a Lorentzian response function. Multiplying top and bottom by the complex conjugate of the denominator gives

$$x_0 = \frac{\left(\frac{F}{m}\right) (\cos \theta - i \sin \theta) \left[ \left(\omega_0^2 - \omega^2\right) + i \frac{\omega\omega_0}{Q} \right]}{\left[ \left(\omega_0^2 - \omega^2\right)^2 + \left(\frac{\omega\omega_0}{Q}\right)^2 \right]} \quad (16)$$

Separating the real and imaginary parts, we define

$$U = \text{Re}(x_0) = \frac{\left(\frac{F}{m}\right) \left[ (\omega_0^2 - \omega^2) \cos \theta + \frac{\omega \omega_0}{Q} \sin \theta \right]}{\left[ (\omega_0^2 - \omega^2)^2 + \left( \frac{\omega \omega_0}{Q} \right)^2 \right]} \quad (17)$$

$$V = \text{Im}(x_0) = \frac{\left(\frac{F}{m}\right) \left[ -(\omega_0^2 - \omega^2) \sin \theta + \frac{\omega \omega_0}{Q} \cos \theta \right]}{\left[ (\omega_0^2 - \omega^2)^2 + \left( \frac{\omega \omega_0}{Q} \right)^2 \right]} \quad (18)$$

The RUS system detects both  $U$ , which is referred to as the real or in-phase portion of the signal, and  $V$ , which is referred to as the quadrature portion of the signal. RUS also detects a frequency dependent background signal. Figure 2.4 is a typical RUS scan displaying both the in-phase and quadrature signals.

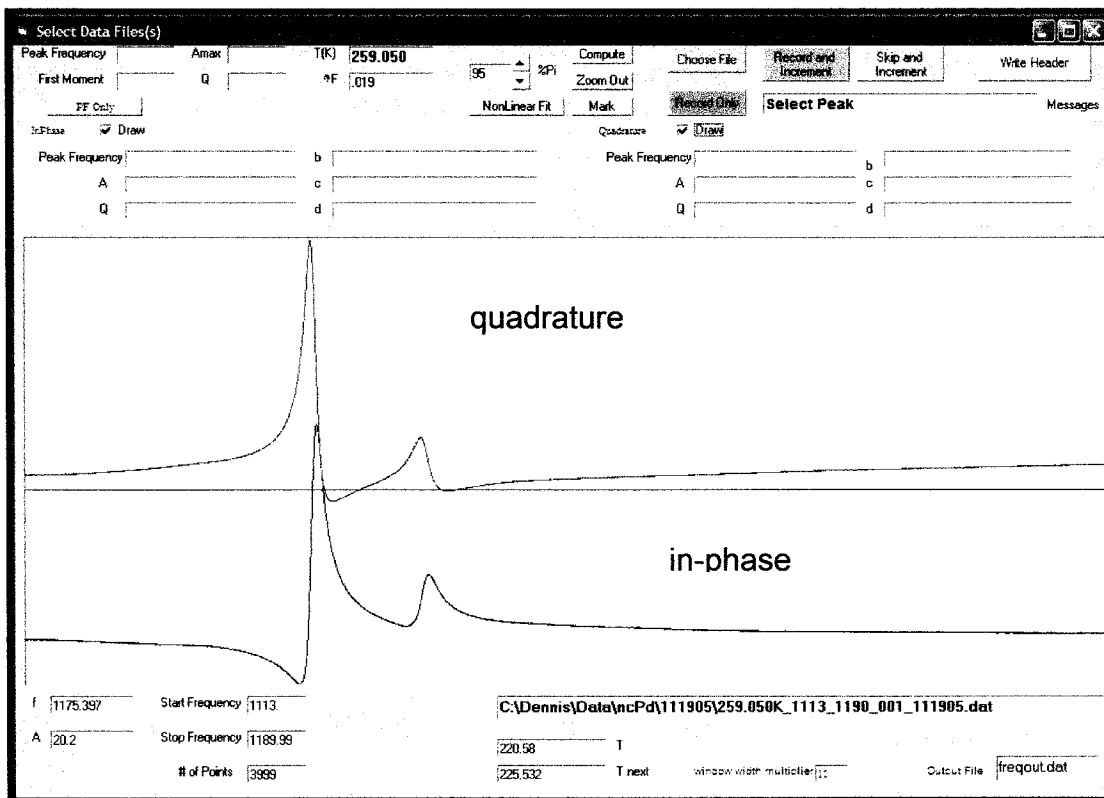


Fig. 2.4 A typical RUS scan showing two resonant frequencies.

The RUS scans for room temperature measurements, oven runs and cryostat runs are all controlled with a Labview program. The original program was developed at Los Alamos, and modified by Dr. Jennifer Atteberry and myself to communicate with the equipment at Colorado State University. The Labview software controls the parameters of signal generator, as well as the cryostat heater and temperature controller. There is currently no interface to the oven controller, so manual temperature control is required for oven runs. The main control screen is displayed in Fig. 2.5

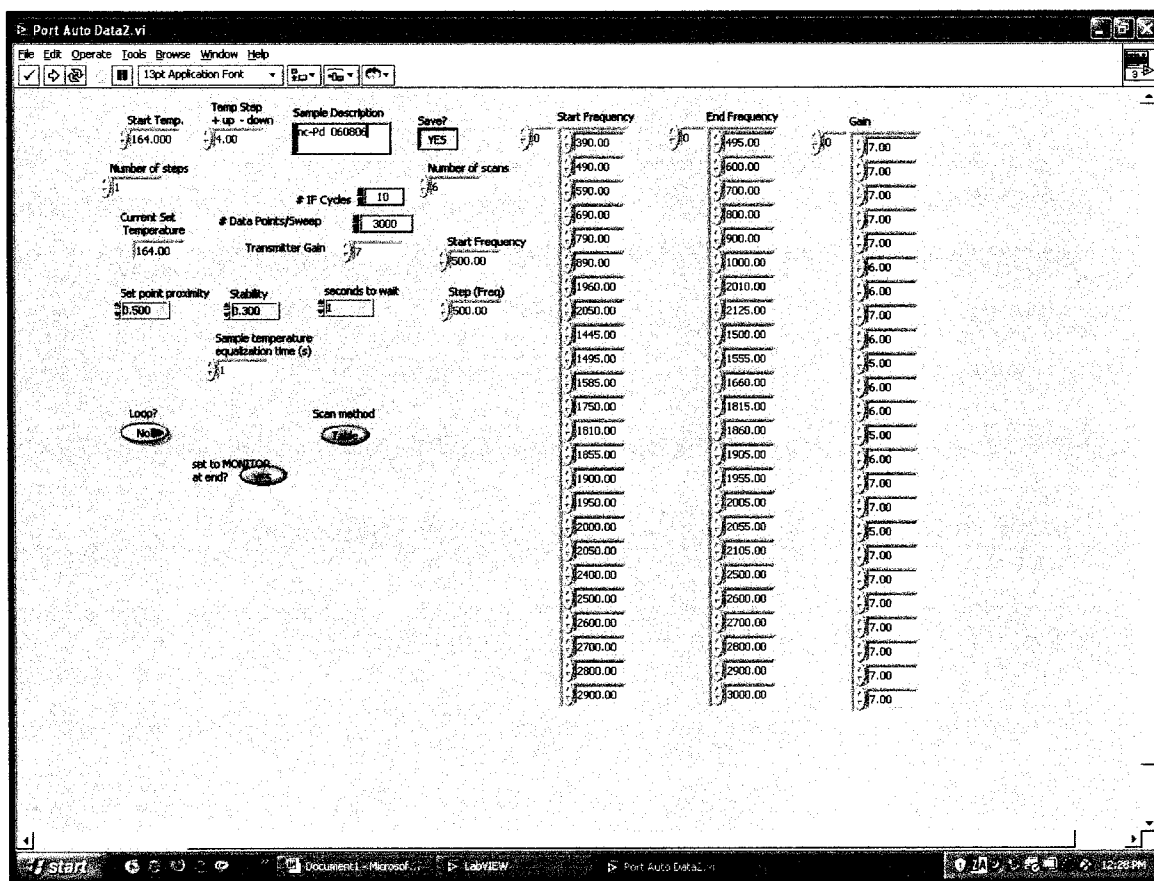


Fig. 2.5 Main Labview screen for RUS scan control.

The Labview program allows automatic control of RUS experiments when used with a temperature controller. The *Start Temp.* field sets the initial temperature

set point, in degrees Kelvin. The *Temp. Step* field allows the set point for consecutive scan sets to be increased or decreased by the number of degrees specified. The *Number of scans* field determines how many frequency scans are in a scan set, and the frequency ranges in each scan is determined by the *Start frequency* and *End frequency* values in kilohertz. It is recommended that an overlap of 5 KHz for adjacent scans be entered in these fields to handle resonant line shapes that are at the edges of the scan range. In addition, the gain of each scan can be controlled by the *Gain* field, with maximum gain triggered by a value of 7. The *Number of steps* field determines how many times the scan set is repeated. The *# Data Points/Sweep* field determines the number of measurements taken in each scan. A value of 500 for every 100 KHz in the scan is sufficient for test runs when looking for background signals, resonances, etc. The program will handle a maximum value of 4200 for this field. For RUS experiments that are going to measure ultrasonic loss, a scan range of 50-60 KHz and 4200 points per scan is recommended.

The control screen also controls how close to the temperature set point the sample temperature has to be and how stable the temperature needs to be before the scans are initiated. The temperature must be within the number of degrees specified in the *Set point proximity* field, and must stay within the number of degrees specified in the *stability* field for the number of seconds specified in the *seconds to wait* field before the scans are initiated. In addition, a fixed amount of wait time can be programmed to delay scan initiation to allow sample stabilization by entering a time interval in the *Sample temperature equalization time* field.

Occasionally, the signal generator needs to be initialized. If the signal generator operation fails, the red light will come on. In addition, if the sample is moved to a different position on the transducers, if the gain is reset on any of the scan ranges, or if the frequencies in a scan range are changed, the controller should be initialized. The initialization program will return information from the signal generator if successful. The initialization screen is displayed in Fig. 2.6.

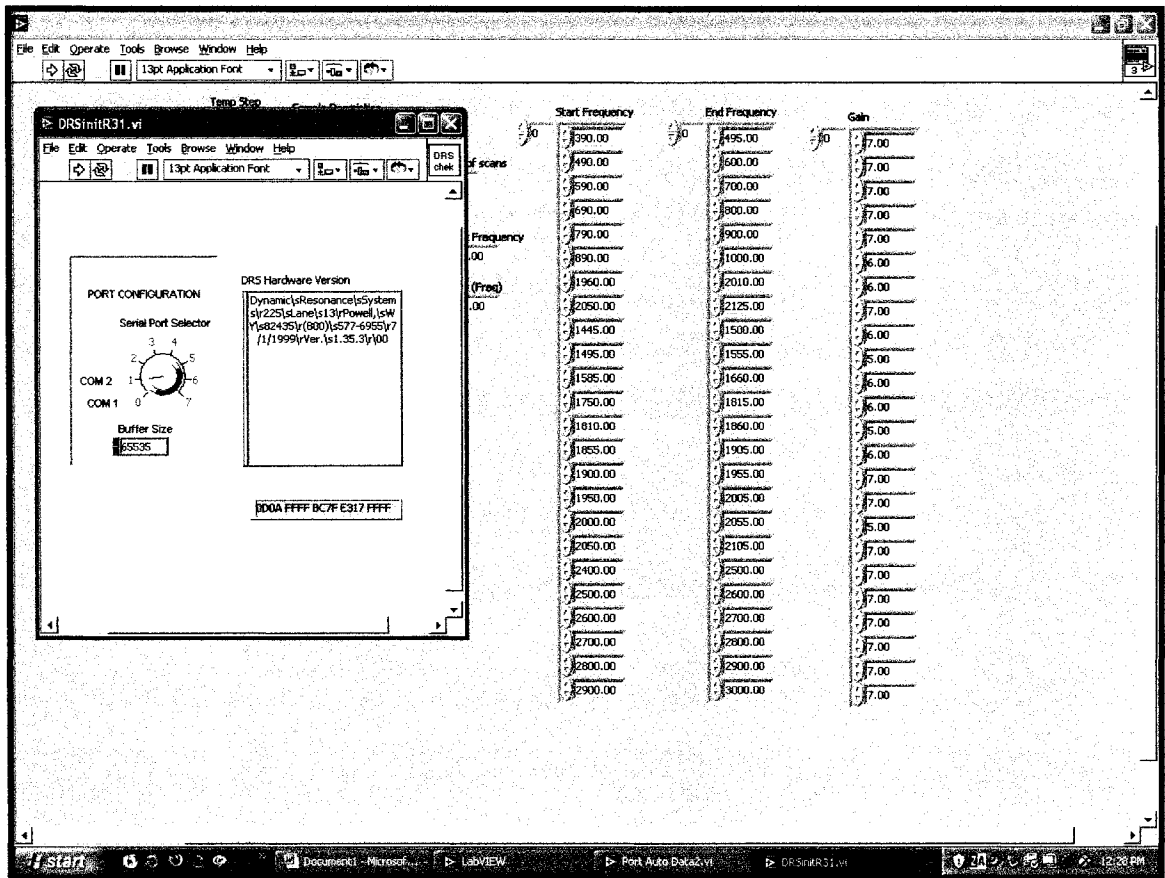


Fig. 2.6 Signal generator initialization program control screen.

After a RUS scan set has been initiated, a screen will appear that graphs the measured control sensor temperature as it approaches the set point. Adjustments to the heater power output, temperature PID parameters or cryogen gas flow may be needed if the temperature change is too slow, or if the control temperature

consistently overshoots the control point and does not stabilize. Once the scans are initiated, a blue progress bar will appear as the input frequency is swept through the specified range. A stalled progress bar indicates that the signal generator needs to be initialized. A typical RUS can is displayed in Fig. 2.7.

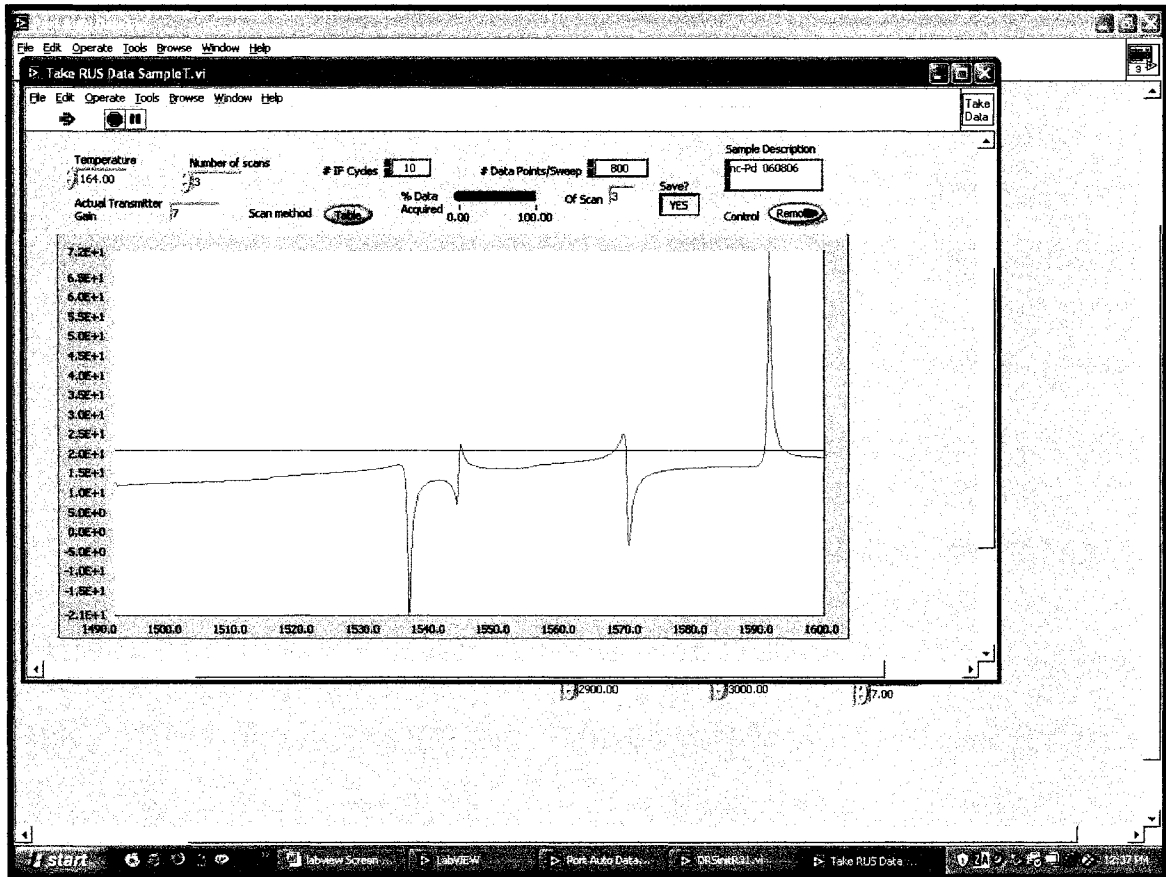


Fig. 2.7 A typical RUS scan. The output files of the scans are placed in the directory C:\Data\RUS\Month Year\mmddyy, where the Month Year and mmddyy are determined by the date of the run.

## 2.5 Analysis

RUS data is analyzed with either the LineFit program or the QFit program.

Both programs are controlled in the same way. LineFit, developed by Albert

Migliori, is useful for doing elastic constant data fits when there is no interest in the  $Q$

of the resonance, since this program is more stable than QFit and does not require an initial step to calculate starting values. The QFit program will capture the  $Q$  value as well as the frequency data needed to determine elastic constants. Both programs start with a file selection dialog and the input file format is that written by the Labview control program.

A typical LineFit scan is displayed in Fig. 2.8.

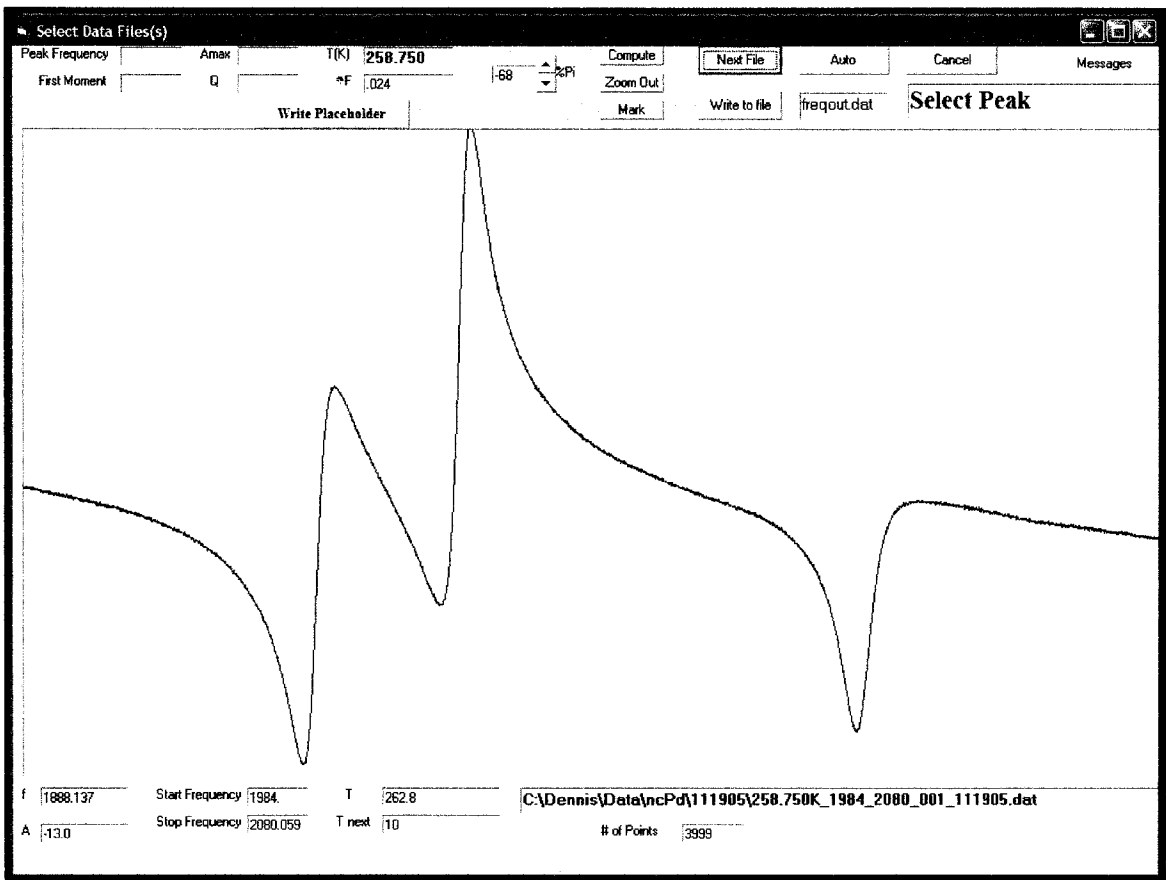


Fig. 2.8 A typical LineFit scan.

The user can zoom in on the scan of interest using the left and right mouse buttons. Clicking the left mouse button will reset the left margin at the location of the cursor, and the right mouse button will reset the right margin at the location of the cursor. The *Zoom out* button will reset the display to the full scan. The *Compute*

button will calculate the center frequency of the resonance. The *Write to file* button will record the frequency in the data file specified in the field next to the button; *freqout.dat* is the default file name. If a resonance is known to be missing, the *Write Placeholder* button will record a zero value which the fitting program will recognize as a missing resonance. After all of the resonances have been processed, the *Next File* button will start the file selection dialog so that the next file in the scan set can be read.

Figure 2.9 displays a typical Qfit scan. The algebra for the QFit program was developed by R.G. Leisure, K. Foster, J.E. Hightower, and D.S. Agosta in Ref. 8, and the non-linear fitting code was developed by Frank Willis. I tested the program operation and added some basic functionality to facilitate the use of the program in the Ultrasonics Lab at Colorado State University. Screen navigation, file input and file output is identical to that as described for the LineFit program. After selecting a resonance to analyze, the *Compute* button is used to generate initial values for the nonlinear fit routine. The *Non-Linear Fit* button is used to fit a curve to the resonant line shape, as illustrated in Fig. 2.9.

In some cases, the curve fitting portion of the software will cause the QFit program to crash. Adjustments to the peak frequency to move the generated center frequency for very sharp resonances may resolve this problem. The usual cause for this problem is a starting  $Q$  value that is too high, or in some cases too low. If adjustments to these values do not result in a viable curve fit, the *PF Only* button may be used to record the peak (resonant) frequency in the output file for elastic constant determination.

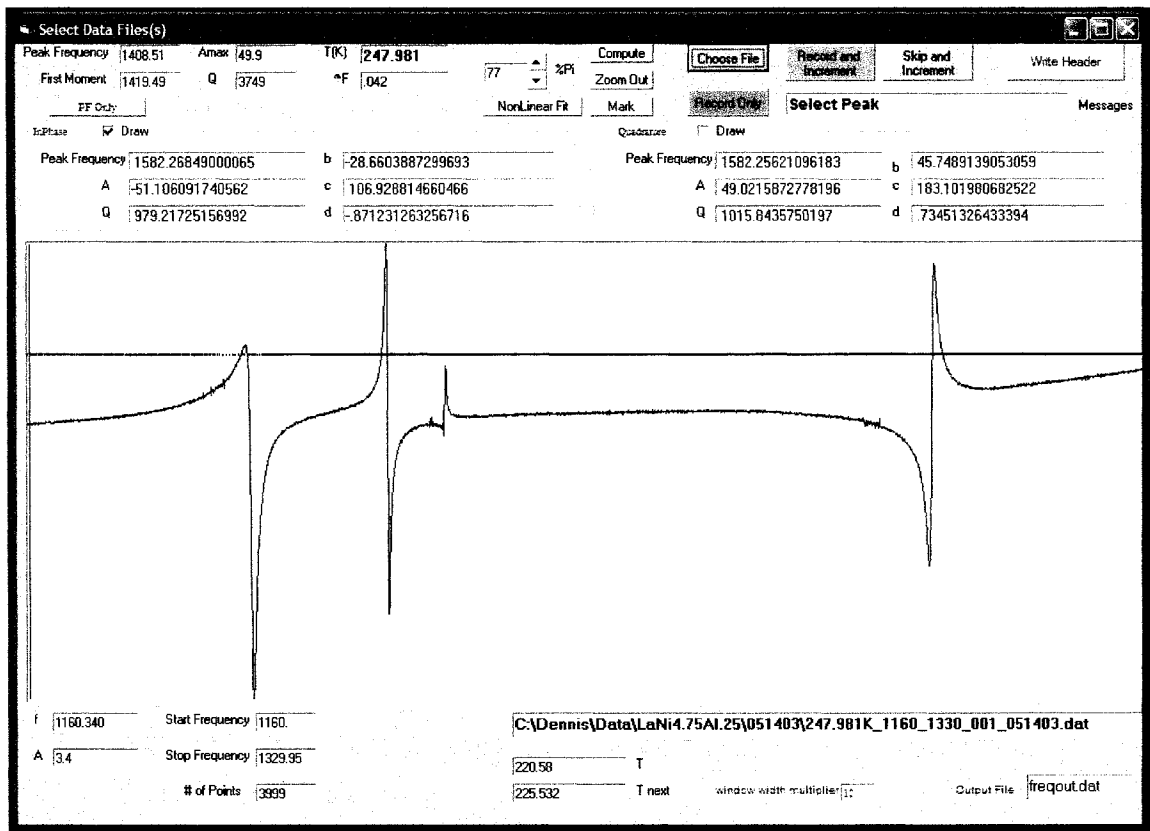


Fig. 2.9 A typical QFit scan.

The determination of the elastic constants from a set of resonant frequencies is accomplished using the RPR program. The rusin.dat file is edited to include the fitting parameters, and the resonant frequencies, as illustrated by Fig. 2.11. The first line of this file contains descriptive text for the output report. The second line contains the following parameters: number of independent elastic constants (2); a zero to indicate fit with the given dimension, or a 3 indicating that the linear dimensions will be allowed to be changed (but conserving volume) as a part of the fit algorithm; a number, usually 12, to indicate the order of the polynomials used for the complete function set; a zero to indicate that the data is to be fit to the theoretical values or a number to indicate how many theoretical resonant frequencies should be

generated and placed in the rusio.dat file; the mass of the sample in grams; the remainder of the line is a string of ones and zeroes.

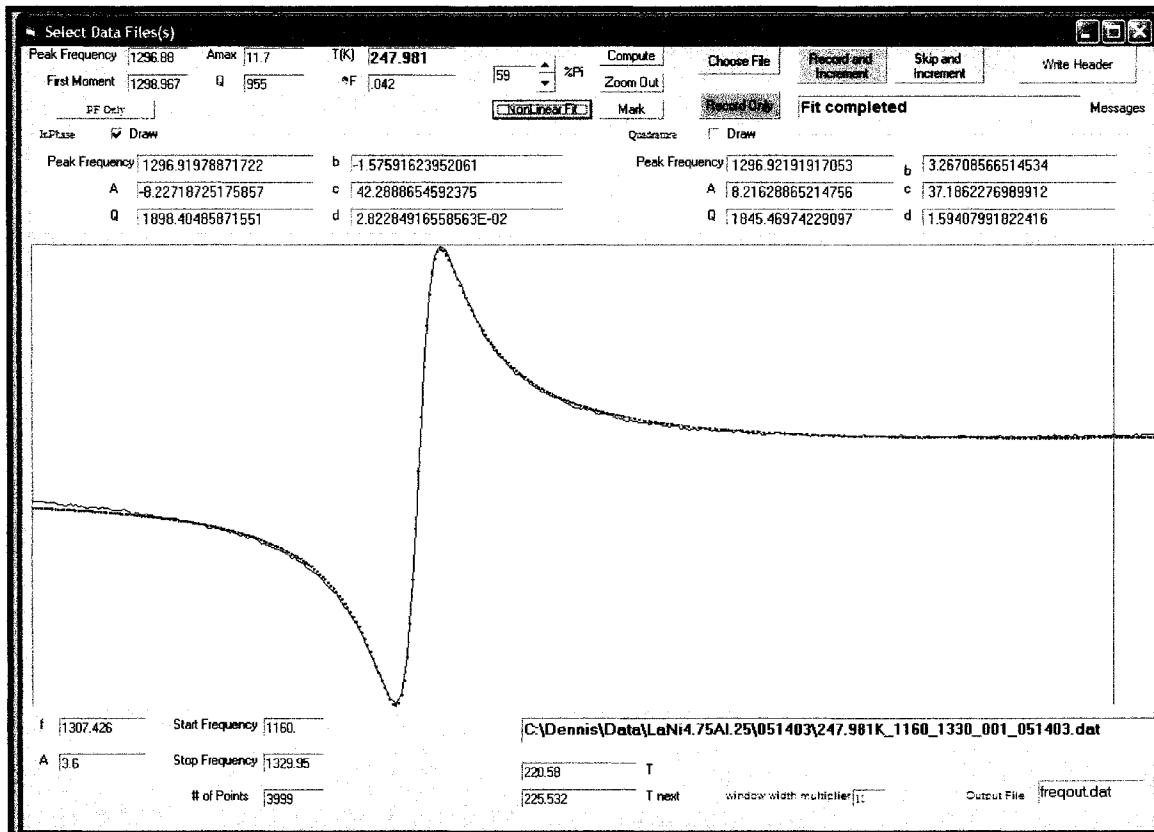


Fig. 2.10 A curve fit for a typical RUS resonance.

```

nc-Pd DSA08 6/17/06
2 0 12 0 0.1821 0.1000E+01 1 0 0 0 0 0 0 0 0 0
2.49 0.54
0.1158 0.1866 0.2271
0.529604247 0 0
0.697820382 0 1
0.943812851 0 1
1.00574846 0 1
1.028466694 0 1
1.036872225 0 1
1.128646473 0 1
1.135210041 0 1
1.247750097 0 1
1.33910598 0 1
1.384570963 0 1
1.461267423 0 1
1.573311072 0 1
1.611170178 0 1
1.613561356 0 1
1.628305 0 1
1.63087524 0 1
1.793653563 0 1
1.799279 0 1
1.834489041 0 1
2.035610885 0 1

```

Fig. 2.11 The rusin.dat file containing the input fitting parameters.

The third line contains the initial guesses for the elastic constants, in this example  $C_{11}$  and  $C_{44}$ . The fourth line contains the sample dimension in centimeters. The remaining lines contain the measured resonant frequencies, followed by a zero and a weighting factor. The first resonance rarely fits well and is usually assigned zero weight<sup>3</sup> and the rest of the frequencies a 1 for 100%. The RPR program will process the data in rusin.dat and rusio.dat and place its results in rusout.dat, as illustrated by Fig. 2.12. The quality of the fit is determined by the rms error value. A value of 0.4% or less is considered a good fit resulting in accurate elastic constants.

```

nc-Pd DSA07 290.4K
free moduli are c11, c44
using 12 order polynomials      mass= 0.0073 gm  rho=11.086 gm/cc

```

n	fex	fr	%err	wt	k	i	df/d(moduli)
1	0.529604	0.517977	-2.20	0.00	4	1	0.00 1.00
2	0.697820	0.696403	-0.20	1.00	1	2	0.09 0.91
3	0.943813	0.946624	0.30	1.00	7	2	0.11 0.89
4	1.005749	1.001549	-0.42	1.00	1	3	0.22 0.78
5	1.028467	1.026251	-0.22	1.00	8	2	0.01 0.99
6	1.036872	1.032814	-0.39	1.00	3	2	0.04 0.96
7	1.128646	1.128176	-0.04	1.00	5	1	0.03 0.97
8	1.135210	1.138750	0.31	1.00	2	2	0.05 0.95
9	1.247750	1.255623	0.63	1.00	6	2	0.10 0.90
10	1.339106	1.339320	0.02	1.00	5	2	0.11 0.89
11	1.384571	1.387659	0.22	1.00	2	3	0.13 0.87
12	1.461267	1.444523	-1.15	1.00	4	2	0.02 0.98
13	1.573311	1.570435	-0.18	1.00	5	3	0.22 0.78
14	1.611170	1.613016	0.11	1.00	3	3	0.06 0.94
15	1.613561	1.616719	0.20	1.00	7	3	0.02 0.98
16	1.628305	1.630822	0.15	1.00	1	4	0.06 0.94
17	1.630875	1.634736	0.24	1.00	6	3	0.03 0.97
18	1.793654	1.793638	0.00	1.00	4	3	0.09 0.91
19	1.799279	1.811592	0.68	1.00	8	3	0.05 0.95
20	1.834489	1.833187	-0.07	1.00	3	4	0.05 0.95
21	1.999421	1.994894	-0.23	1.00	1	5	0.05 0.95

Bulk Modulus= 1.143

c11	c22	c33	c23	c13	c12	c44	c55	c66
1.6573	1.6573	1.6573	0.8861	0.8861	0.8861	0.3856	0.3856	0.3856

d1	d2	d3
0.05067	0.10341	0.12584

loop# 3 rms error= 0.3907 %, changed by 0.0000004 %

length of gradient vector= 0.000001 blamb= 0.000000

eigenvalues	eigenvectors
0.01411	1.00 0.02
57.61024	-0.02 1.00

chisquare increased 2% by the following % changes in independent parameters

1.78	-0.14
0.00	0.12

Fig. 2.12 Output of an elastic constant fit.

## References

- 
- <sup>1</sup> A. Migliori, J.L. Sarrao, W.M. Visscher, T.M. Bell, M. Lei, Z. Fisk, R.G. Leisure, *Physica B*, **183** 1 (1993).
  - <sup>2</sup> R.G. Leisure and F.A. Willis, *J. Phys.: Condens. Matter*, **9** 6001 (1997).
  - <sup>3</sup> A. Migliori, J.L. Sarrao, *Resonant Ultrasound Spectroscopy*, (Wiley, New York, 1997).
  - <sup>4</sup> E. Schreiber, O.L. Anderson, N. Soga, N. Warren, and C. Sholtz, *Science*, **167**, 732-734 (1970).
  - <sup>5</sup> J. Maynard, *Physics Today*, January 1996, 26-31.
  - <sup>6</sup> H.H. Demarest Jr., *J. Acoust. Soc. Am.*, **49**, 768 (1971).
  - <sup>7</sup> I. Ohno, *J. Phys. Earth*, **24**, 355-379 (1976).
  - <sup>8</sup> R.G. Leisure, K. Foster, J.E. Hightower and D.S. Agosta, *Mat. Sci. and Eng, A*, **370**, 34 (2004).

## Chapter 3

### $\text{Ti}_{39.5}\text{Zr}_{39.5}\text{Ni}_{21}$ *i*-phase Quasicrystal

- 3.1 Introduction
- 3.2 Experimental details
- 3.3 Results and discussion
- 3.4 Conclusions
- References

#### 3.1 Introduction

In 1984, a new form of condensed matter was discovered, which is neither amorphous nor crystalline<sup>1</sup>. Quasicrystals have an aperiodic structure, but display perfect long-range translational order. These structures produce rotational symmetries (5-fold, 8-fold, 10-fold, 12-fold) that are forbidden by standard periodic structures, and can be represented as the projection onto three dimensions of higher-dimensional order periodic structures<sup>2,3,4</sup>. Early forms of quasicrystalline materials were metastable, but later forms have been developed that are thermodynamically stable<sup>5</sup>. These materials are interesting from a basic physics viewpoint, but they may have technological importance because of their ability to absorb considerable amounts of hydrogen<sup>6,7</sup>. The thermoelectric properties of quasicrystals are also

being studied for possible application to power generation, cooling, and computer processors <sup>8,9</sup>.

Actual quasicrystal structures are related to Penrose tilings. In one dimension, we can illustrate this concept with a two tile set, a long tile denoted by  $L$  and a short tile denoted by  $S$ . We build up a quasiperiodic structure by applying a set of tiling rules, applied to the current construction, to add components to the one-dimensional material.

$$S \longrightarrow L \qquad L \longrightarrow LS$$

If we start the construction with  $S$ , table 3.1 lists the first nine components to add to the structure <sup>4</sup>.

Table 3.1 One dimensional tiling set for quasiperiodic structure.

Tile set to add	Number of elements
S	1
L	1
LS	2
LSL	3
LSLLS	5
LSLLSLSL	8
LSLLSLSLLSLLS	13
LSLLSLSLLSLLSLSLLSLSL	21
LSLLSLSLLSLLSLSLLSLSLLSLSLLSLLS	34

This structure exhibits short-range and long-range order, since application of the tiling rules can determine the type of tile in any lattice position. The second column of table 3.1 lists the number of basic tiles in each tile set and may be recognized as the Fibonacci sequence.

In two dimensions, a Penrose tiling is a pattern of tiles which could completely cover an infinite plane, but would do so in an aperiodic pattern. A common Penrose tiling set is a thick rhombus and a thin rhombus of equal length sides.

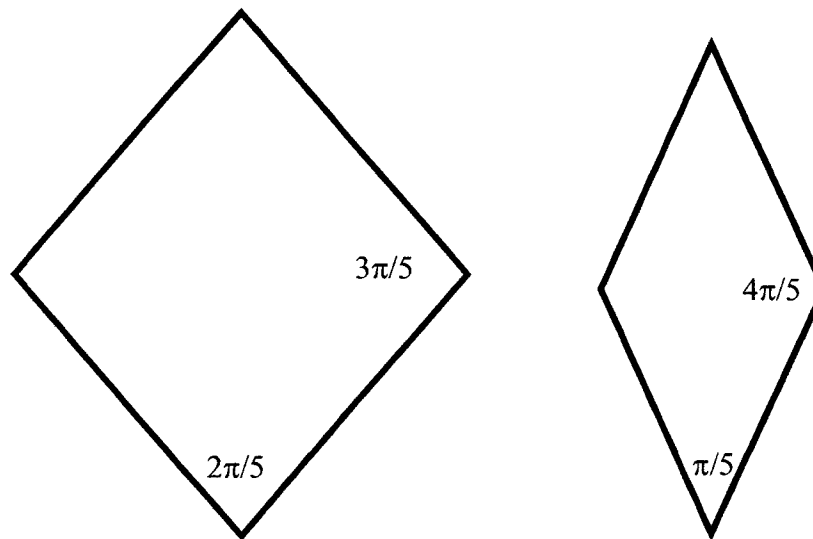


Fig. 3.1 Two-dimensional Penrose tiling set.

The tiles in Fig. 3.1 are used to cover the infinite plane using one construction rule: no two tiles can be touching to form a single parallelogram<sup>10</sup>. The aperiodic tiling accomplished by using the tiles of Fig. 1.3 is not unique, and the number of Penrose tilings is uncountable. In addition, a new tiling is accomplished by a process called deflation, in which each existing tile in the pattern is split into an adjacent cluster of tiles that are rescaled to the size of the original tiles and that satisfy the construction rule. For example, starting with a thick rhombus, the principle axis is divided in such

a way that the ratio of the two segments is  $\tau$ , the golden ratio, and the point of division is connected to the other two vertices, as illustrated in Fig. 3.2. The resulting tile segments are referred to as “dart” and “kite” tiles, and these segments may be further divided, moved and re-scaled to accomplish the deflation process.

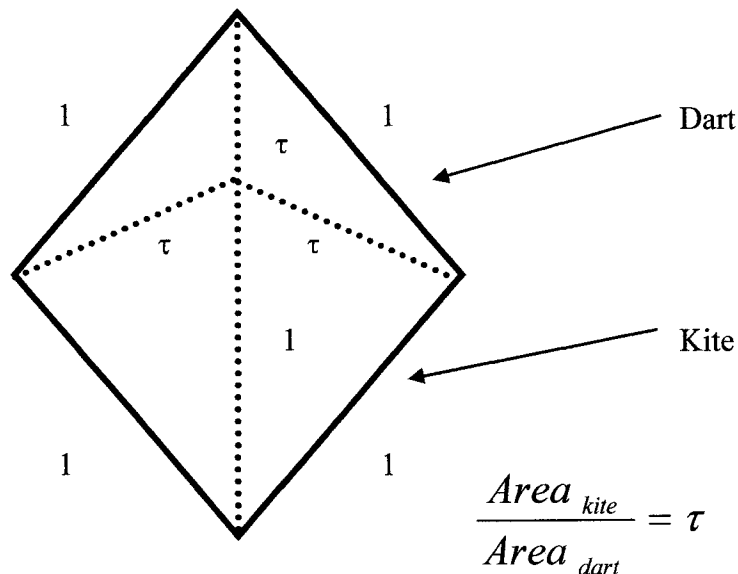


Figure 3.2 Deflation of a thick rhombus tile.

Penrose tilings have been extended to three dimensions by substituting prolate and oblate rhombohedra for the thick and thin rhombi. Computer simulations of the Fourier transform of these tilings have reproduced the electron diffraction patterns of real quasicrystals<sup>4</sup>.

A large body of work has been devoted to these novel materials, including several studies of their elastic properties<sup>11, 12, 13, 14, 15, 16, 17, 18, 19, 20, 21, 22</sup>. Elastic constants are of fundamental importance. The adiabatic elastic constants are the second derivatives of the internal energy with respect to strain, and thus depend sensitively on the interatomic potentials. The temperature dependence is related to anharmonic interactions. An interplay of structure determination and quantum

mechanical calculations based on interatomic potentials will likely be needed to answer some of the fundamental questions regarding quasicrystals<sup>23</sup>, such as the nature of the ground state at 0 K. Elastic constant measurements provide a stringent constraint on the forms of the interatomic potentials used. Also, elastic constants are related to thermal properties through the Debye theory, and are related to practical engineering parameters.

A large class of quasicrystals is formed from rapidly-quenched titanium-based alloys<sup>5, 24</sup>. Of the various ultrasonic studies of elastic constants referenced above, only one, Ref. 18, on  $\text{Ti}_{41.5}\text{Zr}_{41.5}\text{Ni}_{17}$ , was for the Ti-based quasicrystals. Since Ref. 18 appeared, other studies, not based on ultrasound, on similar quasicrystalline materials ( $\text{Ti}_{40}\text{Zr}_{40}\text{Ni}_{20}$  and  $\text{Ti}_{52.8}\text{Zr}_{26.2}\text{Ni}_{21}$ ) have reported unusually low values for the shear and Young's moduli, and values for Poisson's ratio that are very close to the theoretical upper limit<sup>25,26,27</sup>. The present results, on  $\text{Ti}_{39.5}\text{Zr}_{39.5}\text{Ni}_{21}$  prepared by a different method than the samples of Ref 18, are in general agreement with the earlier ultrasonic results, but do not support the unusual values for the shear and Young's moduli, and for Poisson's ratio.

### **3.2 Experimental details**

Ti-Zr-Ni samples of approximately 1g mass were prepared by first arc-melting high-purity, commercially-available, elements (Ti 99.995%, Zr 99.95% and Ni 99.995%) on a water-cooled copper hearth in a high purity (99.995%) Ar atmosphere and then injecting the melt into a copper mold. The resulting ingots were approximately 60 mm long and 3 mm wide; they tapered from a maximum thickness

of 3 mm at the top to 0.35 mm at the bottom. X-ray diffraction patterns taken from different regions of the ingots showed that they contained only the quasicrystal phase with no other contaminating phases.

The ultrasonic samples were cut from a small ingot of material on a low speed diamond saw. The material is brittle, and clean saw cuts were not possible. The rough cubes resulting from the saw cuts were carefully hand polished into highly accurate parallelepipeds using fine grit polishing disks and 3  $\mu\text{m}$  diamond paste. Three samples were prepared; their dimensions are listed in Table 3.2. Sample A was used to measure the elastic constants and ultrasonic loss from 3-292 K. Sample B was used to confirm the room temperature results. Sample C was used for additional ultrasonic loss studies.

Table 3.2 Dimensions and masses of  $\text{Ti}_{39.5}\text{Zr}_{39.5}\text{Ni}_{21}$  samples used in the present study.

	A (cm)	B (cm)	C (cm)	Density (gm/cm <sup>3</sup> )
Sample A	$0.1158 \pm 1.2 \times 10^{-4}$	$0.1866 \pm 1.8 \times 10^{-4}$	$0.2271 \pm 1.1 \times 10^{-4}$	$6.207 \pm 0.08$
Sample B	$0.0937 \pm 1.0 \times 10^{-4}$	$0.1354 \pm 1.3 \times 10^{-4}$	$0.2084 \pm 2.1 \times 10^{-4}$	$6.177 \pm 0.11$
Sample C	$0.0706 \pm 1.2 \times 10^{-5}$	$0.1086 \pm 7.9 \times 10^{-6}$	$0.1759 \pm 1.5 \times 10^{-5}$	$6.619 \pm 0.03$

The sample of *i*-phase  $\text{Ti}_{39.5}\text{Zr}_{39.5}\text{Ni}_{21}$  used in this study is multi-grained. This situation would usually lead to a loss of information as compared to measurements on single-grains. However, the icosahedral symmetry results in elastic isotropy<sup>28</sup>; only two independent elastic constants are required to describe the linear elasticity (see Appendix 2). These two elastic constants are obtained from measurements on multi-grained materials.

### 3.3 Results and discussion

The lowest twenty-two resonant frequencies were measured to determine the elastic constants  $C_{11}$  and  $C_{44}$  of  $\text{Ti}_{39.5}\text{Zr}_{39.5}\text{Ni}_{21}$ . The temperature-dependent results are presented in terms of the bulk modulus  $B$  (Fig. 3.3), and the shear modulus  $G$  (Fig. 3.4), where  $B = C_{11} - \frac{4}{3}C_{44}$  and  $G = C_{44}$ .

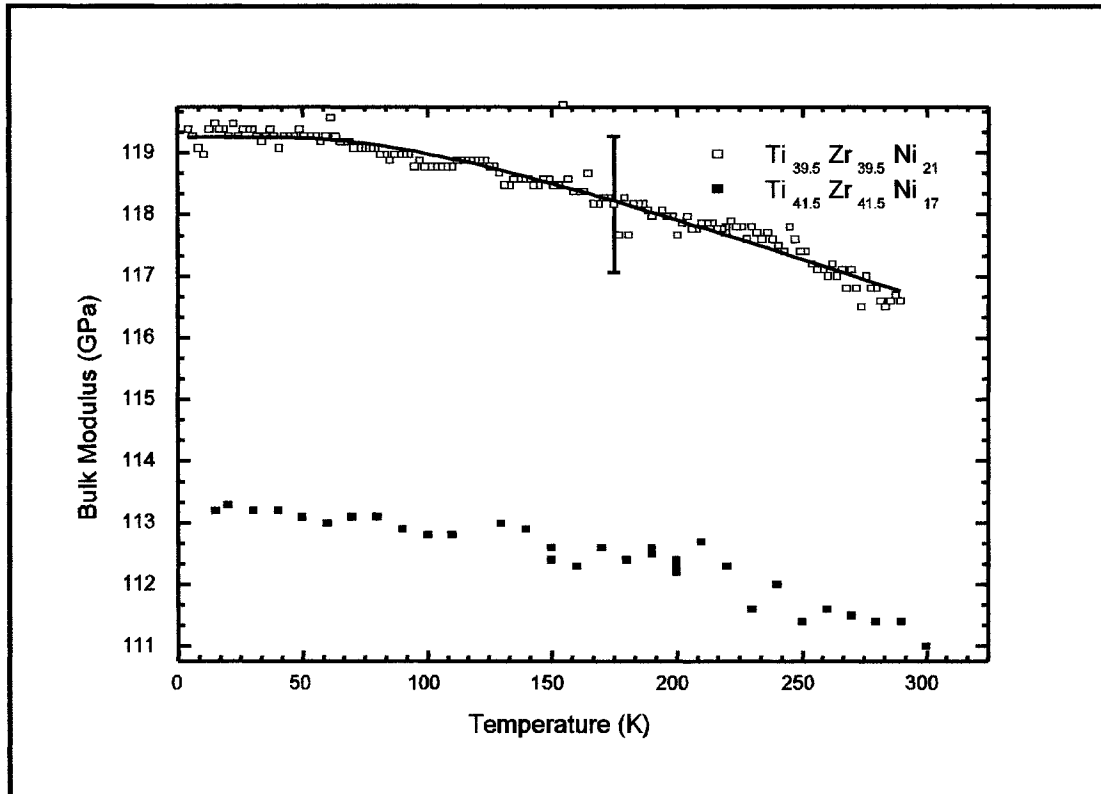


Figure 3.3 Bulk modulus of *i*-phase  $\text{Ti}_{39.5}\text{Zr}_{39.5}\text{Ni}_{21}$  versus temperature. The open symbols are the present results. The filled symbols are for Ref. [18]. The solid line represents a fit of the Varshni expression as described in the text. A representative error bar for the absolute accuracy is shown. The error was computed based on the quality of the fits and errors in mass and dimension measurements. The relative error is much smaller and represented by the scatter in the data.

The elastic constants were not corrected for thermal contraction because thermal expansion data are not available for this material; room temperature

dimensions were used in the analysis. Taking into account the direct dimensional effects as well as the indirect effects through the density, the elastic constants found from the measured frequencies depend inversely on the linear dimensions of the sample<sup>29</sup>. Metals such as Ti, Ni and Zr have a total thermal contraction between room temperature and 0 K between 0.1 and 0.2 %<sup>28</sup>. Assuming a comparable thermal contraction for the quasicrystal, the effect of the thermal contraction would be to increase the elastic constants approximately 0.10-0.20 % at 4 K over that reported in Figs. 3.3 and 3.4.

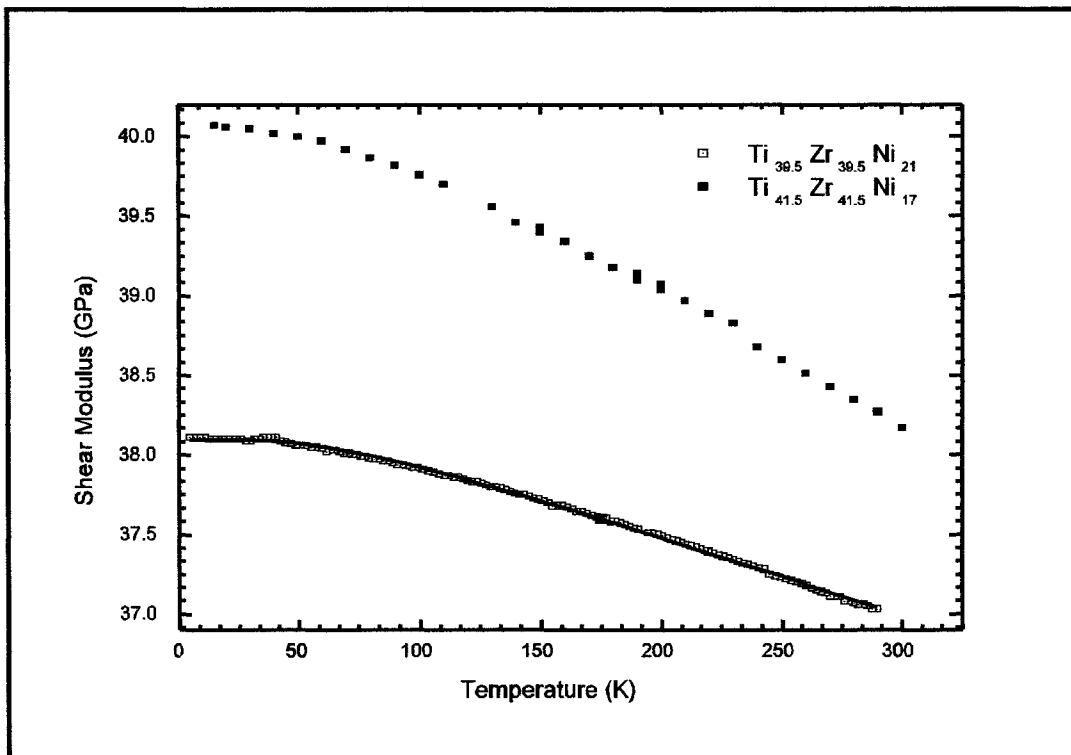


Figure 3.4 Shear modulus of *i*-phase  $\text{Ti}_{39.5}\text{Zr}_{39.5}\text{Ni}_{21}$  versus temperature. The open symbols are the present results. The filled symbols are for Ref. [18]. The solid line represents a fit of the Varshni expression as described in the text. The absolute error of 0.1% is too small to show on the plot.

The accuracy of the shear modulus is higher than that for the bulk modulus because 20 of the first 22 resonances have a dependence on  $C_{44}$  of 91 % or higher.

The fifth and fourteenth resonances in this set have the strongest  $C_{11}$  dependence, 19.2 % and 12.5 % respectively.

Other useful elastic quantities can be calculated from the elastic constants. Figure 3.5 displays the temperature dependence of Young's modulus  $E$ , given by

$$E = C_{44} \left[ \frac{3C_{11} - 4C_{44}}{(C_{11} - C_{44})} \right]. \quad (1)$$

Young's modulus exhibits the same general temperature dependence as the shear modulus. Poisson's ratio  $\nu$ , given by

$$\nu = \frac{C_{11} - 2C_{44}}{2(C_{11} - C_{44})} \quad (2)$$

is displayed in Fig. 3.6. It is fairly constant (increasing slightly with increasing temperature) over the temperature range reported here, and is consistent with the behavior of most metals.

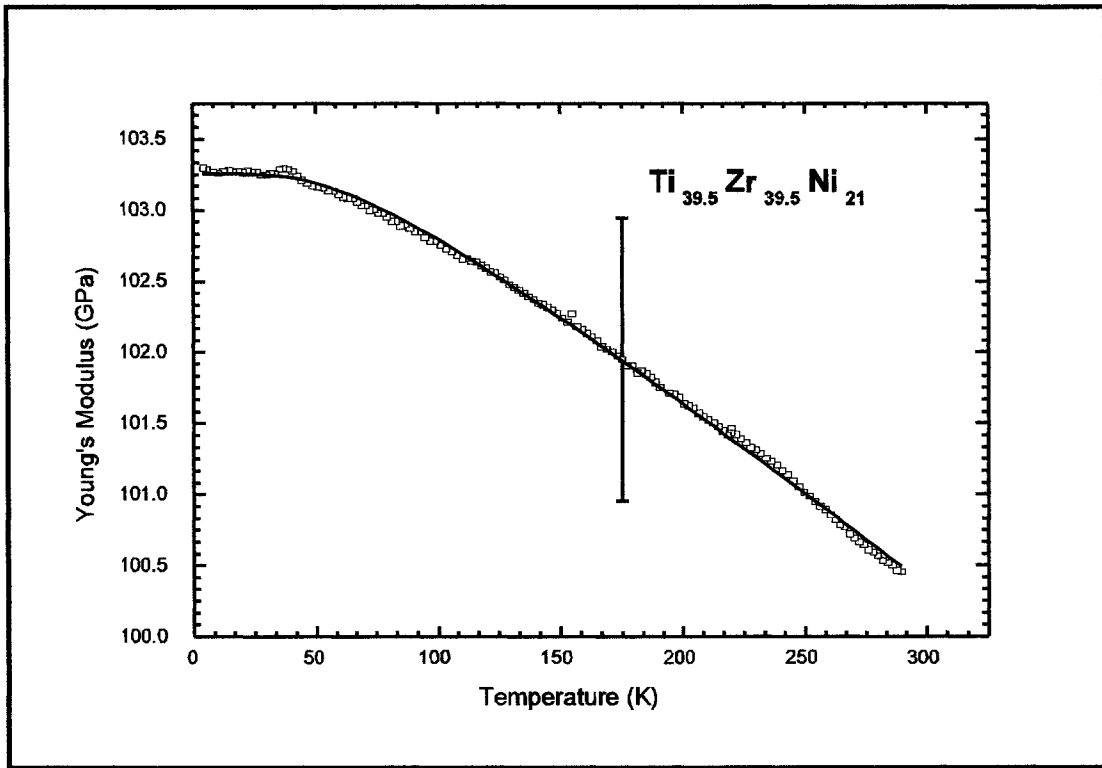


Figure 3.5 Young's modulus of *i*-phase  $\text{Ti}_{39.5}\text{Zr}_{39.5}\text{Ni}_{21}$  versus temperature. The absolute error is based on the errors for Figs. 1 and 2.

The temperature dependence of the elastic constants can be modeled by the Varshni expression<sup>30,31</sup>

$$C(T) = C(0) - \frac{s}{\exp\left(\frac{T_E}{T}\right) - 1} \quad (3)$$

where  $C(0)$  is the value of the elastic constant at zero temperature,  $T_E$  the effective Einstein temperature, and  $s$  an adjustable parameter related to the strength of the anharmonic interactions. This expression is based on the assumption that the thermal phonons responsible for the anharmonic effects can be represented approximately by

$T_E$ . The solid lines in Figs. 3.3, 3.4 and 3.5 represent a fit of Eq. 3 to the data. The fit parameters are given in table 3.3.

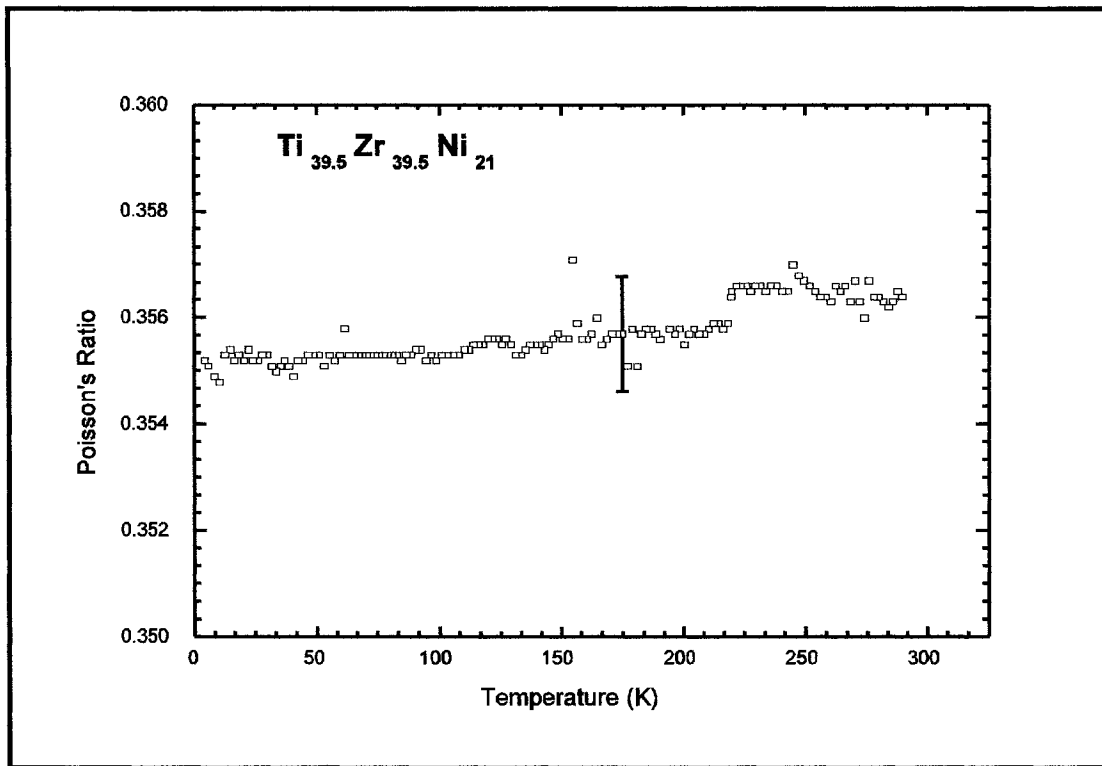


Figure 3.6 Poisson's ratio of *i*-phase  $\text{Ti}_{39.5}\text{Zr}_{39.5}\text{Ni}_{21}$  versus temperature. A representative error bar is displayed.

Table 3.3 Varshni expression fitting parameters for Bulk Modulus ( $B$ ), Shear Modulus ( $G$ ) and Young's Modulus ( $E$ ).

	$C(0)$ (GPa)	$s$ (GPa)	$T_E$ (K)	$Chi^2$
$B$	$119.26 \pm 0.03$	$4.0 \pm 0.58$	$277 \pm 25$	0.03564
$G$	$38.094 \pm 0.003$	$0.9773 \pm 0.023$	$189.6 \pm 3.3$	0.00013
$E$	$103.253 \pm 0.006$	$2.4885 \pm 0.063$	$186.2 \pm 3.5$	0.00101

The elastic constants provide insight into the nature of the bonding. It has been pointed out that the ratio of the shear to the bulk modulus for many icosahedral-phase quasicrystals is more similar to tetrahedrally-bonded semiconductors than to typical metals<sup>15,22</sup>. Such is not the case for the Ti-based quasicrystals. Figure 3.7

illustrates the difference of the Ti-based materials from the other quasicrystals (most of which are Al-based) for which elastic constant data are available. Poisson's ratio is high, and, correspondingly,  $G/B$  is low for the Ti-based materials. The highest  $G/B$  values of Fig. 3.7 are about the same as those for Si and Ge<sup>32</sup>, while the values for the Ti-based materials are similar to many metals such as Cu and Al. It should be noted that the values for Si and Ge are polycrystalline averages, since the crystalline values are anisotropic<sup>33</sup>. The values all fall on a straight line since Poisson's ratio can be calculated from the shear and bulk moduli.

It is interesting to compare the present results on  $\text{Ti}_{39.5}\text{Zr}_{39.5}\text{Ni}_{21}$  with earlier ultrasonic results on  $\text{Ti}_{41.5}\text{Zr}_{41.5}\text{Ni}_{17}$ <sup>18</sup>. The bulk modulus with the higher Ni content is about 5% higher and the temperature dependence is essentially unchanged. The shear modulus with the higher Ni content is 3 – 6 % lower, and the temperature dependence is weaker, indicating lower anharmonicity. These features provide constraints on possible interatomic potentials in these novel materials.

The present results on  $\text{Ti}_{39.5}\text{Zr}_{39.5}\text{Ni}_{21}$  give room temperature values of Young's modulus  $E = 100.5$  GPa, the shear modulus  $G = 38.1$  GPa, and Poisson's ratio  $\nu = 0.356$ . Other values for these quantities, based on pressure-volume curves ( $\text{Ti}_{40}\text{Zr}_{40}\text{Ni}_{20}$ ) and conventional tensile testing ( $\text{Ti}_{52.8}\text{Zr}_{26.2}\text{Ni}_{21}$ ), have appeared in the literature:  $E \approx 43$  GPa;  $G \approx 5 - 7$  GPa; and  $\nu \approx 0.48$ <sup>25, 26, 27</sup>. The differences from the ultrasonic results seem to be far too large to attribute to experimental error. The reason for these differences is unknown, although it is interesting to note a previous case of substantial differences of elastic parameters of an Al-based quasicrystal when comparing ultrasonic results with conventional tensile testing<sup>15</sup>.

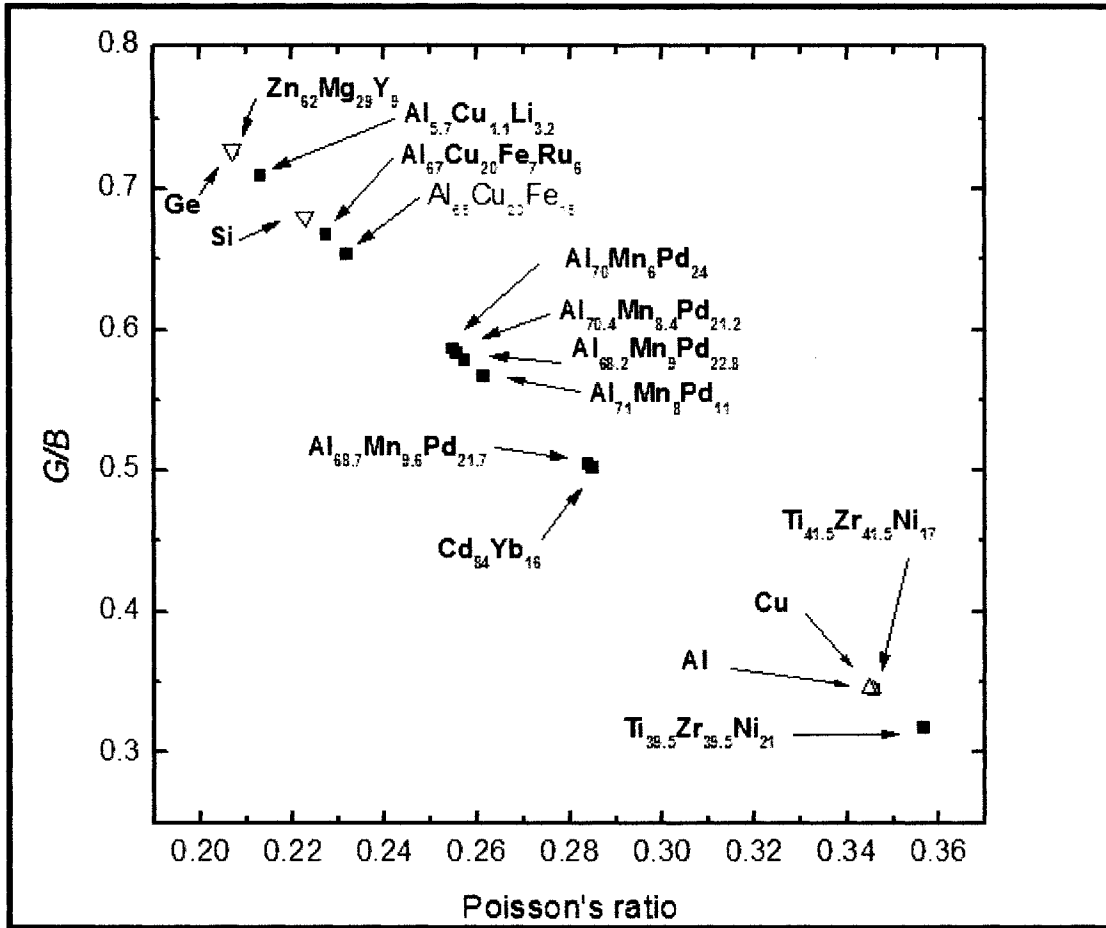


Figure 3.7 Poisson's ratio vs. the ratio of shear modulus/bulk modulus for a number of quasicrystalline materials. Also shown are values for Ge and Si. Data from present work and from Refs. [ 13, 14, 15, 16, 17, 18, 19, 20, 21, 22, 32]..

The long-wavelength phonon contribution to the heat capacity can be calculated from the elastic constants. In the low-temperature limit this contribution is given by

$$C_{ac} = \frac{2\pi^2 k_B^4}{5\hbar^3 v_0^3} T^3 \quad (4)$$

where  $v_0$  is an average sound velocity given by

$$\frac{1}{v_0^3} = \frac{1}{3} \left[ \frac{1}{v_l^3} + \frac{2}{v_t^3} \right] \quad (5)$$

and the longitudinal  $v_l$  and transverse  $v_t$  sound velocities are calculated from

$$v_l = \sqrt{\frac{C_{11}}{\rho}} \text{ and } v_t = \sqrt{\frac{C_{44}}{\rho}}. \text{ In these equations } \rho \text{ is the density, } T \text{ is the temperature}$$

and  $k_B$  is Boltzmann's constant. The values of the zero-temperature velocities from

the Varshni fit parameters are  $v_l = 5.23 \times 10^3$  m/s and  $v_t = 2.48 \times 10^3$  m/s, resulting

in  $v_0 = 2.79 \times 10^3$  m/s (By comparison,  $v_0 = 2.89 \times 10^3$  m/s for *i*-phase

Ti<sub>41.5</sub>Zr<sub>41.5</sub>Ni<sub>17</sub><sup>18</sup>). Using these values, the acoustic contribution to the low

temperature molar specific heat for *i*-phase Ti<sub>39.5</sub>Zr<sub>39.5</sub>Ni<sub>21</sub> is found to be  $C_{ac}/T^3 = 6.12$

$\times 10^{-5}$  J/mole K<sup>4</sup>. ( $C_{ac}/T^3 = 5.64 \times 10^{-5}$  J/mol K<sup>4</sup> was reported for *i*-phase

Ti<sub>41.5</sub>Zr<sub>41.5</sub>Ni<sub>17</sub>.)

It is common practice to describe the acoustic contribution to the heat capacity in terms of a Debye temperature  $\theta_D$ . The usual definition, involving the number of atoms per unit cell, is ambiguous in a quasicrystal. Following Ref. 17 we simply define a Debye temperature as

$$\theta_D = \left[ 6\pi^2 \frac{N}{V} \right]^{1/3} \frac{\hbar}{k_B} v_0 \quad (6)$$

where  $N/V$  is the number of atoms per unit volume. Using the zero-temperature  $v_0$  calculated above gives a Debye temperature of  $\theta_D = 316.7$  K. The Debye temperature for *i*-phase Ti<sub>41.5</sub>Zr<sub>41.5</sub>Ni<sub>17</sub> has been calculated from the earlier reported parameters as  $\theta_D = 324.6$ K. For comparison the Debye temperatures of the constituent elements are: Ti (396.1 K), Zr (212.13 cubic, 293.2 K hexagonal), and Ni (452.38K)<sup>34</sup>.

The internal friction (ultrasonic loss) was measured for a number of resonances by fitting the resonance line shapes to a Lorentzian expression<sup>35</sup> to determine the  $Q$ . The results are given in Fig. 3.8 for three different frequencies, showing that the loss increases with temperature above 150 K. All three frequencies have a dependence on the elastic constant  $C_{44}$  greater than 90%.

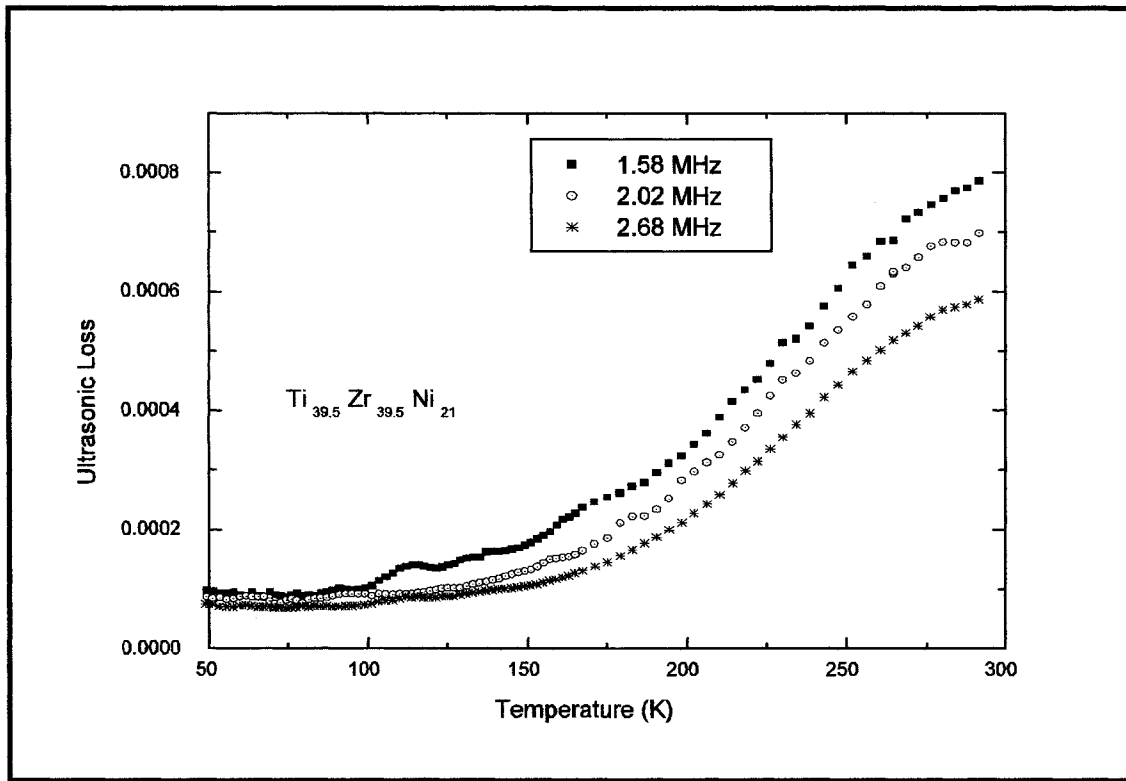


Figure 3.8 Ultrasonic loss of  $i$ -phase  $\text{Ti}_{39.5}\text{Zr}_{39.5}\text{Ni}_{21}$  versus temperature

Two rather general mechanisms for loss are the thermoelastic effect<sup>36</sup> and the Akhieser mechanism<sup>37</sup>. Both depend on  $\omega\tau$  where  $\omega$  is the angular frequency of the ultrasonic vibration and  $\tau$  is the relevant relaxation time for each case. For the present temperatures and frequencies, we are in the  $\omega\tau \ll 1$  limit, in which case the internal friction  $Q^{-1}$  is proportional to  $\omega\tau$ . We expect the thermoelastic effect to be much smaller than the effects of Fig. 3.8 based on two factors: the effect depends on a

volume change which is almost absent for the nearly-pure shear modes of Fig. 3.8; and rough estimates of the relevant parameters<sup>36</sup> also indicate that the effect is negligible for the present case. Ultrasonic attenuation in a AlPdMn quasicrystal - but at much higher frequencies, 10 – 40 GHz, than the present results – has been attributed to the Akhieser mechanism<sup>38</sup>. Extrapolation to the present frequencies indicates that the Akhieser mechanism contribution is far too small to account for the results of Fig. 3.8. In fact, for a given temperature, the loss of Fig. 3.8 does not increase with  $\omega$ , but decreases. The data of Fig. 3.8 have the appearance of the onset of a thermally activated loss peak. Unfortunately, it was not possible to extend the present measurements to higher temperatures to explore this possibility. An internal friction peak in an AlPdMn quasicrystal was found at about 400 K (although for considerably lower measuring frequencies than the present results) and attributed to local atomic movements, perhaps phason jumps<sup>39</sup>. Measurements at higher temperatures for the present material are needed to further characterize the loss.

### 3.4 Conclusions

Resonant ultrasound spectroscopy was used to measure the elastic constants of an icosahedral  $\text{Ti}_{39.5}\text{Zr}_{39.5}\text{Ni}_{21}$  quasicrystal over the temperature range 3-292K. The results were in general agreement with earlier ultrasonically-derived values for *i*-phase  $\text{Ti}_{41.5}\text{Zr}_{41.5}\text{Ni}_{17}$ . In particular, the room-temperature values for the Young's modulus, the shear modulus, and Poisson's ratio are in general agreement with the earlier ultrasonic results, but differ strongly from reported results on similar materials obtained by pressure-volume measurements and conventional mechanical testing.

The reason for this disagreement is unknown. In comparison to many other *i*-phase materials, the ultrasonic measurements show that the TiZrNi materials have a low shear modulus to bulk modulus ratio, and a high Poisson's ratio. These results suggest that the interatomic bonding in the TiZrNi materials differs substantially from that in many of the other *i*-phase materials. A Debye temperature of 316.7 K was calculated from the low-temperature elastic constants, which permits the calculation of the long-wavelength acoustic contribution to the heat capacity. The internal friction increases rather strongly in the temperature range of 150 – 300 K, suggestive of a thermally activated process. Further measurements at higher temperatures are needed to explore this effect.

## References

- <sup>1</sup> D. Sheckman, I. Blech, D. Gratias, J.W. Cahn, Phys. Rev. Lett. **53**, 1951 (1984).
- <sup>2</sup> R.G. Henning, K.F. Kelton, A.E. Carlsson, C.L. Henly, Phys. Rev. B **67** (2003).
- <sup>3</sup> E. Abe, Y. Yan, S. Pennycook, Nature Materials **3** 759 (2004).
- <sup>4</sup> P.M. Ossi, *Disordered Materials, An Introduction* (Springer, Berlin, 2003).
- <sup>5</sup> K.F. Kelton, W.J. Kim, R.M. Stroud, Appl. Phys. Lett., **70** (24) 3230 (1997).
- <sup>6</sup> R.M. Stroud, A.M. Viano, P.C. Gibbons, K.F. Kelton, S.T. Misture, Appl. Phys. Lett. **69** (20), 2998 (1996).
- <sup>7</sup> P.C. Gibbons, R.G. Henning, V.T. Huett, K.F. Kelton, J. Non-Cryst. Solids **334&335**, 461-465 (2004).
- <sup>8</sup> T.M. Tritt, M.L. Wilson, A.L. Johnson, S. LeGault, R. Stroud, 16<sup>th</sup> Int. Conf. on Thermoelectrics (1997).
- <sup>9</sup> Y.K. Kuo, J.R. Lai, C.H. Huang, C.S. Lue, S.T. Lin, J. Phys.: Condens. Matter **15**, 7555-7561 (2003).
- <sup>10</sup> <http://www.stephencollins.net/Web/Penrose/Default.aspx>.
- <sup>11</sup> G.A.M. Reynolds, B. Golding, A.R. Kortan, J.M. Parsey, Phys. Rev. B **41**, 1194 (1990).
- <sup>12</sup> S. Sathish, A. Kulik, G. Gremaud, Solid State Commun. **77** 403 (1991).
- <sup>13</sup> Y. Amazit, M. de Boissieu, A. Zarembovitch, Europhys. Lett. **20** 703 (1992).
- <sup>14</sup> P.S. Spoor, J.D. Maynard, A.R. Kortan, Phys. Rev. Lett. **75** (19) 3462 (1995).
- <sup>15</sup> K. Tanaka, Y. Mitarai, M. Koiwa, Phil. Mag. A **73** 1715 (1996).
- <sup>16</sup> P. Djemia, F. Ganot, C. Dugautier, and M. Quilichini, Solid State Commun. **106** 459 (1998).
- <sup>17</sup> M.A. Chernikov, H.R. Ott, A. Bianchi, A. Migliori, T.W. Darling, Phys. Rev. Lett. **80** (2), 321-324 (1998).
- <sup>18</sup> K. Foster, R.G. Leisure, J.B. Shaklee, J.Y. Kim, K.F. Kelton, Phys. Rev. B **59** 11132 (1999).
- <sup>19</sup> R. Sterzel, C. Hinkel, A. Haas, A. Langsdorf, G. Bruls, W. Assmus, Europhys. Lett. **49** 742 (2000).
- <sup>20</sup> J. Y. Duquesne and B. Perrin, Physica B **316-317** 317 (2002).
- <sup>21</sup> C.A. Swenson, I.R. Fisher, N.E. Anderson, Jr., P.C. Canfield, A. Migliori, Phys. Rev. B, **65** 184206 (2002).
- <sup>22</sup> J. Schreuer, W. Steurer, T.A. Lograsso, D. Wu, Phy. Mag. Lett., **84** (10), 643-653 (2004).
- <sup>23</sup> W. Steurer, J. Non-Crystall. Sol. **334&335** 137 (2004).
- <sup>24</sup> K.F. Kelton, Int. Mater. Rev. **38**, 105 (1993).
- <sup>25</sup> U. Ponkratz, R. Nicula, A. Jianu, E. Burkel, J. Phys.: Condens. Matter, **12** 8071-8080 (2000).
- <sup>26</sup> U. Ponkratz, R. Nicula, A. Jianu, E. Burkel, Ferroelectrics **250** 269 (2001).
- <sup>27</sup> J.B. Qiang, Z.N. Yu, H.G. Huang, et al., Acta Physica Sinica **54** (4), 1909-1913 (2005).
- <sup>28</sup> Per Bak, Phys. Rev. Lett. **54** 1517 (1985).
- <sup>29</sup> R.G. Leisure and F.A. Willis, J. Phys.: Condens. Matter **9** 6001 (1997).
- <sup>30</sup> Y.P. Varshni, Phys. Rev. B. **2** (10), 3952 (1970).

- 
- <sup>31</sup> H. Ledbetter, in: R.P. Reed, A.F. Clark (Eds.), *Materials at Low Temperatures*, American Society for Metals, Metals Park, OH, (1983).
- <sup>32</sup> G. Simmons and H. Wang, 1971, *Single crystal elastic constants and calculated aggregates: a handbook* (Cambridge: M.I.P. Press).
- <sup>33</sup> J.J. Wortman and R.A. Evans, *J. Appl. Phys.* **36**, 153 (1965).
- <sup>34</sup> H. Ledbetter and S. Kim in , *Handbook of elastic properties of solids, liquids, and gases*, Vol. II, M. Levy, H.E. Bass, and R.R. Stern, eds. (Academic Press, San Diego, 2001), Chapt. 7.
- <sup>35</sup> R.G. Leisure, K. Foster, J.E. Hightower, and D.S. Agosta, *Materials Science and Engineering A* **370**, 34 (2004).
- <sup>36</sup> R. Truell, C. Elbaum, and B. Chick, *Ultrasonic methods in solid state physics* (Academic Press, New York, 1969), p. 180.
- <sup>37</sup> A. Akhieser, *J. Phys. (USSR)* **1**, 277 (1939).
- <sup>38</sup> J.-Y. Duquesne and B. Perrin, *Phys. Rev. B* **68**, 134205 (2003).
- <sup>39</sup> B. Damson, M. Weller, M. Feuerbacher, B. Grushko and K. Urban, *J. Alloys Compounds* **310**, 184 (2000).

## **Chapter 4**

### **Nanocrystalline palladium (nc-Pd)**

- 4.1 Introduction
- 4.2 Experimental details
- 4.3 Results and discussion
- 4.4 Conclusions
- References

#### **4.1 Introduction**

The study of materials with microstructures on the scale of nanometers is the subject of a large number of research investigations. In particular, the elastic properties of several nanocrystalline materials have been studied using various experimental techniques<sup>1, 2, 3, 4, 5, 6</sup>. Particles of nanometer-scale size, films of nanometer-scale thickness, and materials with nanometer-scale average grain size all produce physical properties with desirable impact on modern technologies<sup>7</sup>.

Nanocrystalline materials have a lower density than perfect crystals with the same chemical composition because nanocrystals have a reduced atomic density at the grain interfaces<sup>4, 6, 8, 9</sup>. Nanocrystals also contain more defects, in the form of dislocations, vacancies, and voids, than their corresponding coarse-grained forms<sup>1</sup>.

In ordinary polycrystalline materials, less than 1% of the atoms occupy lattice positions within one lattice parameter of a grain boundary. Approximately 50% of

the atoms in a nanocrystal with an average grain size of 5 nm are found within a lattice parameter of a grain surface. For an average grain size of 20 nm, this value is approximately 15%, while at the upper limit of 100 nm average grain size, approximately 3% of the atoms are within a lattice parameter of the grain surface. Atoms that form the surface of grains experience different interatomic coupling forces than atoms internal to the grain boundary. The higher percentage of atoms in nanocrystals that exist in this condition, as well as the spatial arrangement of the variations in the structure of the grains, when compared to perfect single crystals and polycrystals results in different elastic properties as quantified by the elastic constants<sup>3, 5, 6, 10</sup>. While average grain size has a significant impact on the physical properties of a nanocrystal, it has been shown that the method of preparation and thermo-mechanical history of the sample also have an effect<sup>10, 11, 12, 13</sup>. Grain boundaries also have a large impact on the properties of nanocrystals due to the large strains they induce within the crystallites. Elastic moduli measured for nanocrystals are values which have been averaged over the interior of the grains and the grain surface where the interatomic distances are larger<sup>3, 6, 12</sup>.

The atomic structure of nanocrystals differs from that of crystals and glasses. The interatomic spacing of the atoms forming the grain boundaries depend upon the random orientation of a grain with respect to its neighbors, so the atoms on the grain boundaries either do not exhibit short-range order, or exhibit a highly reduced degree of short range order, with periodicity and atomic density varying from grain to grain. The atomic structure of the grain boundary, which has a large impact on the

properties of the material, depend upon the consolidation parameters of the sample<sup>7, 9, 10, 14, 15</sup>. Nanocrystalline materials can exhibit grain size growth at ambient temperature due to excess free energy in the grain boundaries<sup>7, 14, 16</sup>. Grain growth may be stabilized by introducing a second material into the evaporation phase of material generation, thereby forming a second phase of crystallites within the mix<sup>9</sup>. The crystallites of the second phase serve as pinning sites for the grain boundary dislocations and provide solute drag effects, both of which inhibit grain growth<sup>7</sup>.

## 4.2 Experimental details

The nc-Pd and ncPdSi materials were prepared by inert gas condensation and compacted into a pellet *in-situ* at compaction pressure of 4800 psi. The melt purity was 99.95% Pd and 99.99% Si. X-ray measurements indicated an initial nc-Pd average grain size of  $20.5 \text{ nm} \pm 2.9 \text{ nm}$ , and the grains grew to an average of 80-100 nm within the first 48 hours at room temperature. Initial average grain size for the nc-PdSi material, which contained 0.5 at% of Si, was 14.7 nm. Both materials were stored in liquid nitrogen when not in use. X-ray line broadening measurements taken after the sample were prepared and the RUS runs completed indicated little or no further grain growth in nc-Pd and an average grain size of 22 nm in nc-PdSi.

The samples were cut from small, thin disks on a low speed diamond saw. In order to reduce grain size growth room temperature adhesives were used in the polishing processes. Highly accurate parallelepiped samples were produced using fine grit polishing disks and 3  $\mu\text{m}$  diamond paste. Sample dimensions are listed in

table 4.1. The samples used in this study are polycrystalline and therefore elastically isotropic, requiring two independent elastic constants to describe linear elasticity <sup>8</sup>.

Table 4.1 Dimensions of nc-Pd and nc-PdSi samples.

	A (cm)	B (cm)	C (cm)	Density (gm/cm <sup>3</sup> )
nc-Pd	$0.0506 \pm 2.1 \times 10^{-5}$	$0.1035 \pm 2.3 \times 10^{-5}$	$0.1259 \pm 2.0 \times 10^{-5}$	$11.0946 \pm 0.06$
nc-PdSi	$0.0375 \pm 7.1 \times 10^{-6}$	$0.1141 \pm 1.0 \times 10^{-5}$	$0.1355 \pm 7.9 \times 10^{-6}$	$11.7332 \pm 0.004$

### 4.3 Results and discussion

The lowest twenty-one resonant frequencies were measured to determine the elastic constants  $C_{11}$  and  $C_{44}$  of nc-Pd and nc-PdSi. The temperature-dependent results are presented in terms of the bulk modulus  $B$  (Fig. 4.1), and the shear modulus  $G$  (Fig. 4.2), where  $B = C_{11} - \frac{4}{3}C_{44}$  and  $G = C_{44}$ . Room temperature values for nc-Pd are  $B = 114.1$  GPa and  $E = 38.6$  GPa, with an rms error in the data fit of 0.3968%. The room temperature values for the silicon stabilized form, nc-PdSi, are  $B = 179.0$  GPa and  $E = 45.6$  GPa, with an rms error of 0.3441%. Both the bulk and shear moduli in nc-Pd decrease almost linearly with increasing temperature from 4 K to approximately 210 K, and from approximately 260 K to 300 K. In the region  $T \approx 210$ -260 K, both moduli exhibit an increase in their rate of change due to anelastic relaxation of the grain boundaries in this temperature range. This effect is absent in the nc-PdSi sample. Figures 4.1 and 4.2 also display the polycrystalline averages of the elastic constants of Pd, calculated from the single crystal elastic constants <sup>17</sup> using the Hershey-Kröner-Eshelby averaging method <sup>18</sup>. The

temperature dependence of the nc-Pd have values that are 31.5-40.0% lower for the bulk modulus and 17.8-18.6% lower for the shear modulus when compared to pc-Pd over the temperature range covered by this study. A lowering of the elastic constants is expected in nanocrystalline materials due to the increased number of grain boundary interfaces compared to coarse-grained forms<sup>5,10</sup>. The silicon stabilized form, nc-PdSi, exhibits a bulk and shear modulus temperature dependence nearly identical to pc-Pd, with bulk modulus values 4.4-5.8% lower than pc-Pd, and shear modulus values 3.7-4.9% lower.

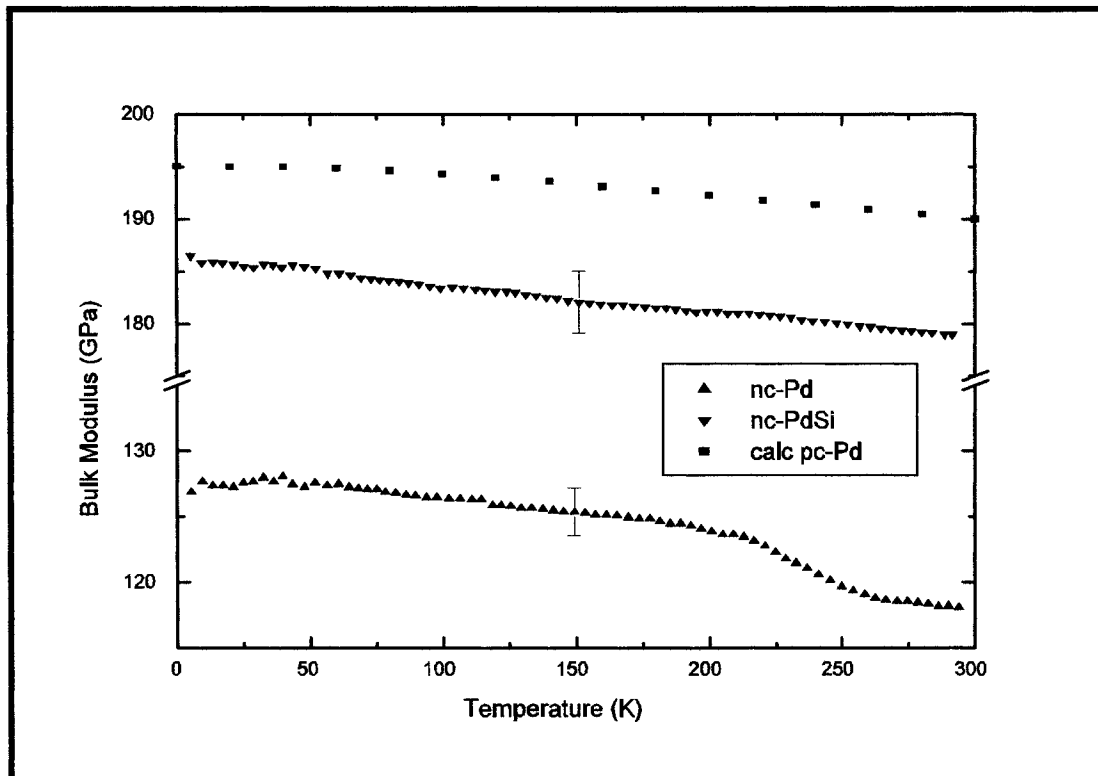


Fig. 4.1 Bulk modulus of nc-Pd and nc-PdSi versus temperature. A representative error bar for the absolute accuracy is shown. The error was computed based on the quality of the fits and errors in mass and dimension measurements. The relative error is much smaller and represented by the scatter in the data.

The elastic constants were not corrected for thermal contraction because thermal expansion data is not available for these materials. X-ray diffraction studies

have shown that the thermal expansion coefficient of nanocrystalline Pd would not differ significantly from that of polycrystalline Pd <sup>19</sup>. Assuming similar thermal contraction of the nanocrystal compared to palladium over the temperature range 4.2-300K, the effect of the thermal contraction would be to increase the elastic constants approximately 0.079 % at 4 K over the values reported in Figs. 4.1 and 4.2 <sup>20</sup>. The accuracy of the shear modulus is higher than that for the bulk modulus because 15 of the first 22 resonances have a dependence on  $C_{44}$  of 90% or higher. The fourth, eleventh and thirteenth resonances in this set have the strongest  $C_{11}$  dependence, 22%, 13% and 22% respectively.

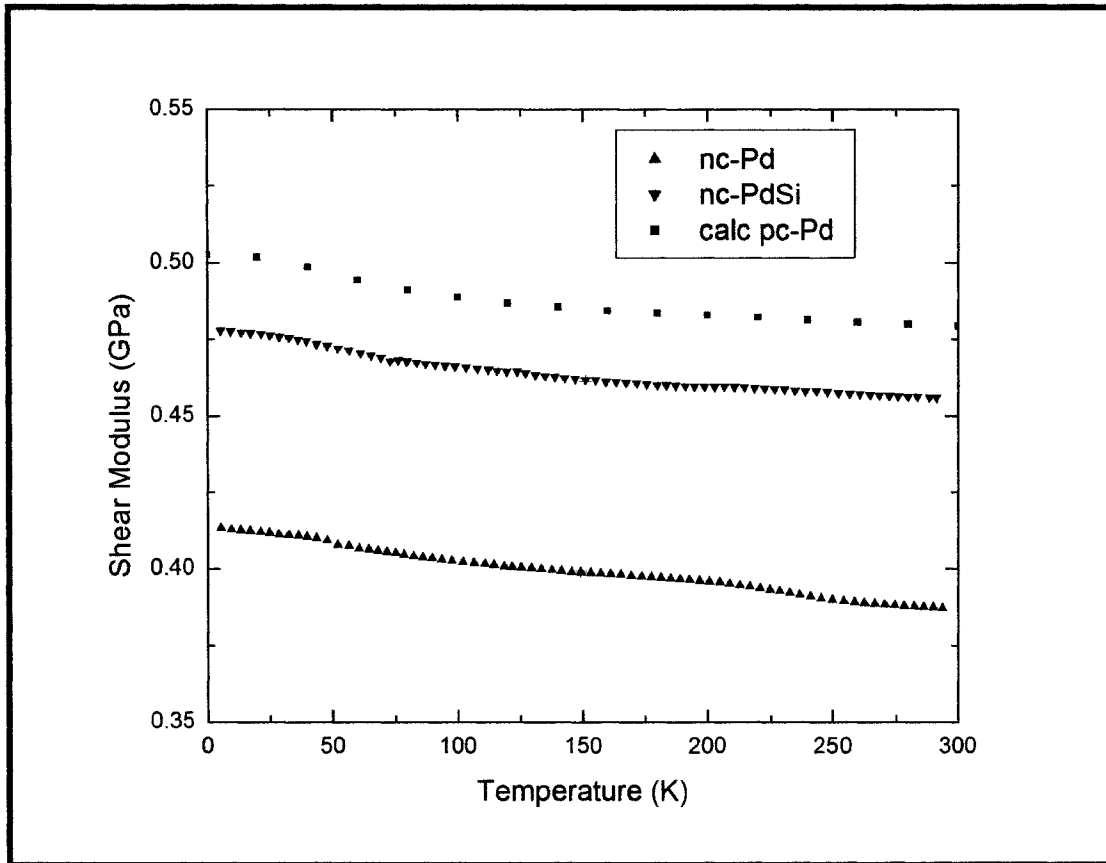


Fig. 4.2 Shear modulus of nc-Pd and nc-PdSi versus temperature. The absolute error of 0.1% is too small to show on the plot.

The temperature dependence of the elastic constants of single crystal and polycrystalline Pd is unusual<sup>17</sup>. Neither of these materials exhibit behavior that is consistent with the semi-empirical Varshni expression<sup>21</sup>, which predicts the elastic constants should vary as  $T$  at high temperature, and approach zero degrees with zero slope. Some of the elastic constants of single crystal Pd exhibit a slight positive curvature, with a minimum at approximately 120 K. This effect has been attributed to the temperature dependence of the contribution to the shear constants from the electron holes in the  $4d$  band<sup>20</sup> and as the contribution of a polarization term, which is negative and which depends upon the magnetic susceptibility  $\chi$ <sup>22</sup>. The calculated polycrystalline averages do not display this minimum, but the behavior is anomalous due to the  $C_{44}$  contribution to the shear and bulk moduli. nc-PdSi displays the same general behavior as pc-Pd in the temperature dependence of its elastic moduli.

Other useful elastic quantities can be calculated from the elastic constants.

Figure 4.3 displays the temperature dependence of Young's modulus  $E$ , given by

$$E = C_{44} \left[ \frac{3C_{11} - 4C_{44}}{(C_{11} - C_{44})} \right] \quad (8)$$

Young's modulus exhibits the same general temperature dependence as the shear modulus. Poisson's ratio  $\nu$ , given by

$$\nu = \frac{C_{11} - 2C_{44}}{2(C_{11} - C_{44})} \quad (9)$$

is displayed in Fig. 4.4. It is fairly constant for nc-PdSi (increasing slightly with increasing temperature) over the temperature range reported here, while nc-Pd shows a decrease with increasing temperature from approximately 210-260K. This decrease

corresponds to the change in the rate of decrease with increasing temperature in the shear modulus.

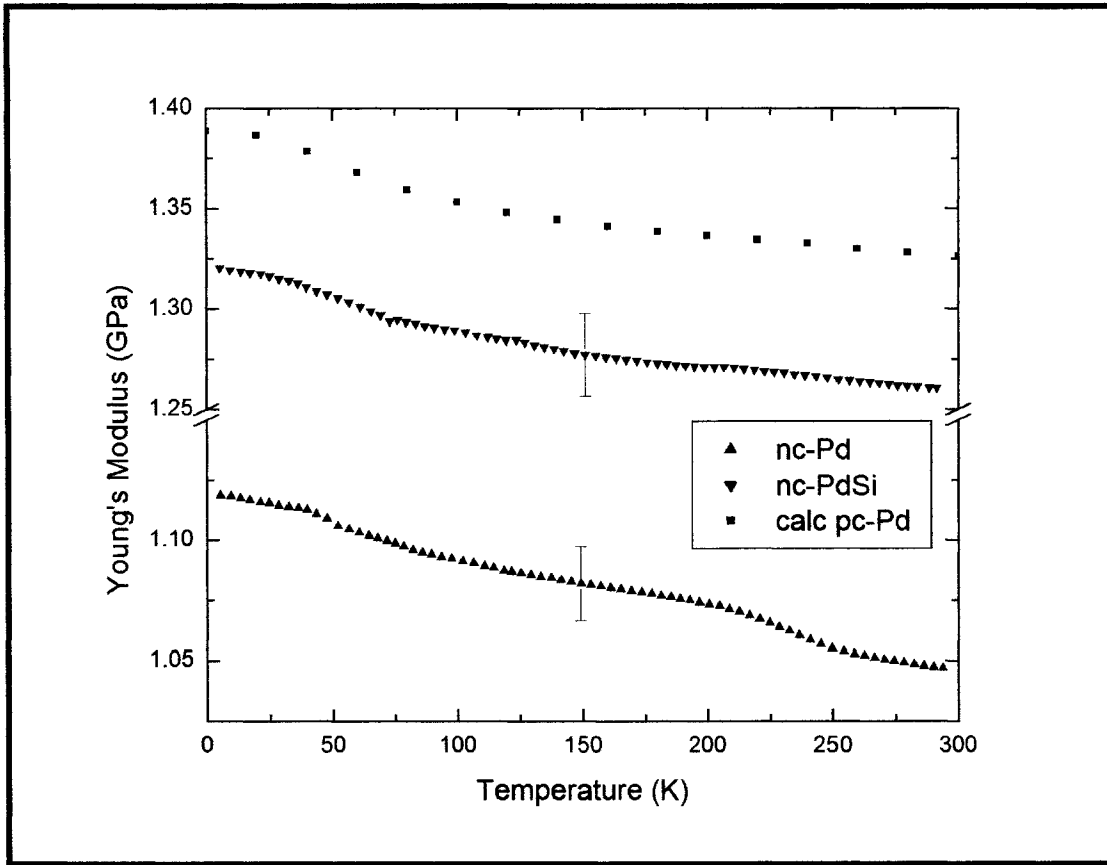


Fig. 4.3 Young's modulus nc-Pd and nc-PdSi versus temperature. The absolute error is based on the errors for figs. 4.1 and 4.2.

It is interesting to compare the present results on nc-Pd with earlier elastic constant measurements on similar materials. Table 4.2 compares the reported values of the shear modulus  $G$  and Young's modulus  $E$  for the current study and earlier studies. Despite average grain sizes 10-20 times larger than those in the earlier studies, the nc-Pd values reported here compare favorably to the values reported in the other studies.

Table 4.2 Comparison of room temperature shear modulus and Young's modulus of nc-Pd to earlier studies.

Reference	Avg. Grain Size (nm)	$G$ (GPa)	$E$ (GPa)
2	15	42.5	115.5
3	5-15	35	
5	8	32	88
current	80-100	38.6	104.0

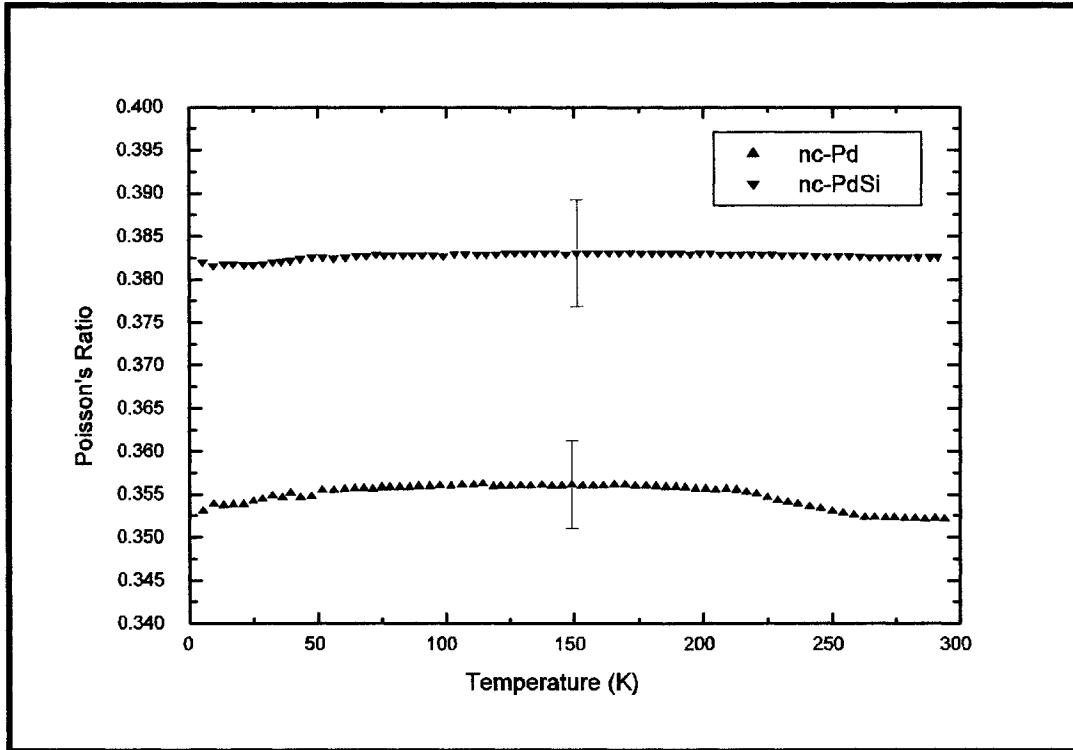


Fig. 4.4 Poisson's ratio of nc-Pd and nc-PdSi versus temperature. A representative error bar is displayed.

The anelastic relaxation of the grain boundaries produce a temperature dependent shift of the elastic constants and resonant frequencies in the temperature region where the elastic constants are changing from the low temperature unrelaxed constant,  $c_U$ , to the high temperature relaxed constant,  $c_R$ . In a real crystal, the strain cannot respond instantaneously to the applied stress, and the elasticity is described by complex elastic constants. In the low temperature region where  $\omega\tau \gg 1$ , the maximum out of phase condition exists between stress and strain, and the complex

elastic constant is approximately equal to  $c_U$ . In the high temperature region where  $\omega\tau \ll 1$ , the minimum out of phase condition exists between stress and strain, and the complex elastic constant is approximately equal to  $c_R$ <sup>23</sup>. In nc-Pd, the loss is due to movement or reorientation of the grain boundaries<sup>24, 25, 26, 27</sup>. The temperature dependent shift is given by

$$\delta c = \Delta c \frac{\omega^2 \tau^2}{1 + \omega^2 \tau^2} \quad (1)$$

and

$$\delta f = \frac{f_0}{2} \frac{\Delta c}{c} \frac{\omega^2 \tau^2}{1 + \omega^2 \tau^2} \quad (2)$$

where  $\Delta c = c_U - c_R$ ,  $c$  is an elastic constant,  $\omega$  is the ultrasonic angular frequency,  $\tau$  is the effective relaxation time of the anelastic process and  $f_0$  is the resonant frequency at room temperature<sup>23, 28</sup>. The quantity  $\frac{\Delta c}{c}$  is often referred to as the relaxation

strength. The relaxation time is described by the Arrhenius relation

$$\tau = \tau_0 \exp\left(\frac{E_a}{k_B T}\right) \quad (3)$$

where  $E_a$  is the activation energy.

The anelastic relaxation of the grain boundaries is attributed to a distribution of possible relaxation mechanisms with slightly different activation energies, since the local environments of the atoms on the grain surfaces are different from atom to atom. The temperature dependent frequency shift was fit by assuming a Gaussian distribution of activation energies

$$G(E, E_a, \sigma) = \frac{1}{\sigma\sqrt{\pi}} \exp\left(-\frac{(E - E_a)^2}{\sigma^2}\right) \quad (4)$$

and fitting the frequency with

$$f(T, E_a, \sigma) = \int_{E_a - 3\sigma}^{E_a + 3\sigma} \frac{f_0 \left( \frac{\Delta c}{c} \right) \omega^2 \tau^2(T, E) G(E, E_a, \sigma)}{1 + \omega^2 \tau^2(T, E)} dE \quad (5)$$

The result of this fit for the room temperature resonance of  $f_0 = 1.138$  MHz is displayed in Fig. 4.5 and yields values of  $E_a = 0.78$  eV,  $\tau_0 = 5.56 \times 10^{-24}$  s,  $\sigma = 0.09$  eV, and  $\Delta c/c = 8.80 \times 10^{-3}$ .

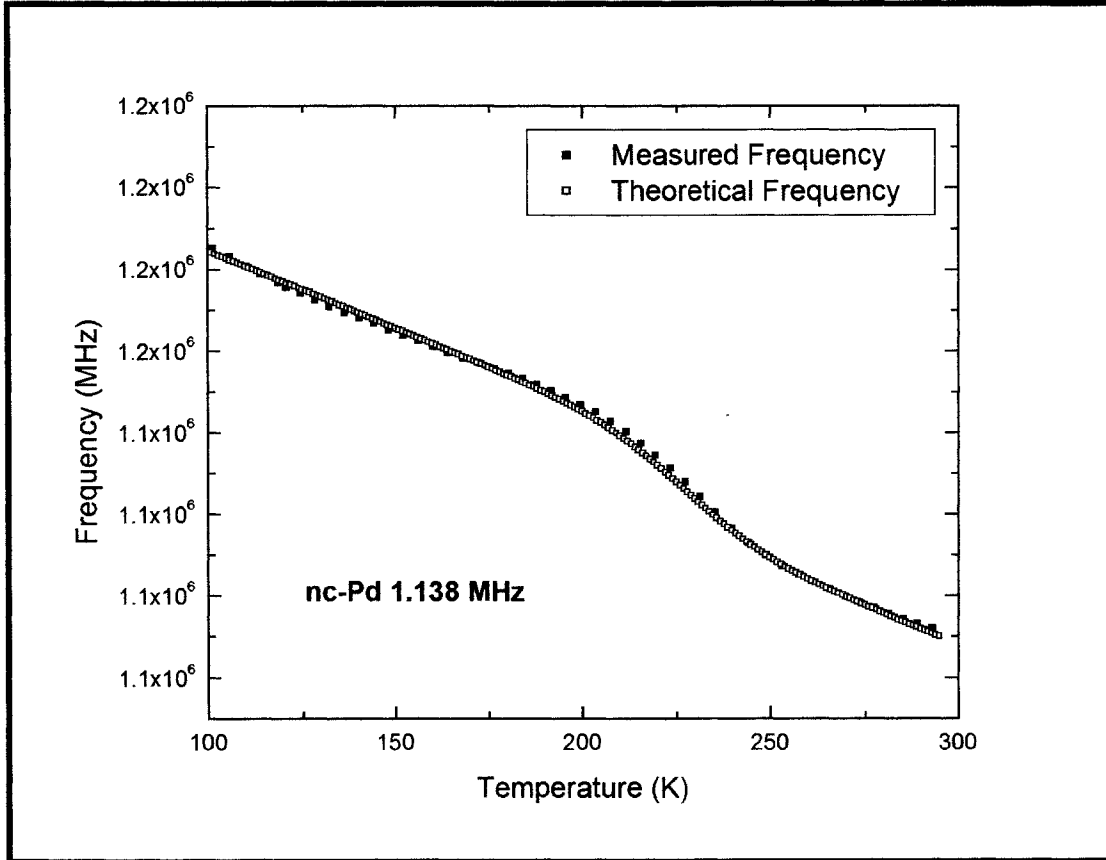


Fig. 4.5 Measured and theoretical frequency versus temperature for the room temperature resonance of  $f_0 = 1.138$  MHz. Fitting parameters are  $E_a = 0.78$  eV,  $\tau_0 = 5.56 \times 10^{-24}$  s,  $\sigma = 0.09$  eV,  $\Delta c/c = 8.80 \times 10^{-3}$ .

The ultrasonic loss peaks were fit using a Debye expression for the ultrasonic loss,  $Q^{-1}$ , given by

$$Q^{-1} = \left( \frac{\Delta c}{c} \right) \frac{\omega \tau}{1 + \omega^2 \tau^2} \quad (6)$$

where  $Q$  is the quality factor of the resonant frequency line shape. The ultrasonic loss was further refined by the same procedure for fitting the temperature dependence of the resonant frequencies

$$Q^{-1}(T, E_a, \sigma) = \int_{E_a - 3\sigma}^{E_a + 3\sigma} \left( \frac{\Delta c}{c} \right) \frac{\omega \tau(T, E) G(E, E_a, \sigma)}{1 + \omega^2 \tau^2(T, E)} dE \quad (7)$$

The same set of fitting parameters used in Eq. (5),  $f_0 = 1.138$  MHz,  $E_a = 0.78$  eV,  $\tau_0 = 5.56 \times 10^{-24}$  s,  $\sigma = 0.09$  eV, and  $\Delta c/c = 8.80 \times 10^{-3}$ , was used to calculate the fitting curve from Eq. (7), and the result is displayed in Fig. 4.6. The calculated curve agrees with the actual curve fairly well and verifies that the parameters calculated from Eq. (5) accurately describe the anelasticity of the nc-Pd sample. The value for  $\tau_0$  has little physical significance and most likely results from averaging over multiple loss process that can couple rather than a simple superposition of multiple uncoupled processes<sup>29</sup>.

The value of 0.78 eV for activation energy agrees fairly well with studies of nc-Al, which reported activation energies for a loss peak near 180K of 0.8 eV and 1.4 eV<sup>27</sup>. The absence of the loss peak in the nc-PdSi sample, where silicon atoms occupy space between the palladium grains, indicates that the loss mechanism is a grain boundary effect. The loss peak in nc-Pd is most likely caused by grain boundary sliding and reorientation, although there may be a contribution from ordering of the disordered grain boundaries<sup>24, 25</sup>.

The ultrasonic loss for nc-Pd shows a peak centered near 264 K, while nc-PdSi does not show any loss peak, as illustrated in Fig. 4.6. Small internal friction

peaks have been reported for nc-Pd at 120, 220 and 400 K<sup>3</sup>. The 120 K peak has been attributed to a dislocation Bordoni relaxation with an activation energy of 0.26 eV. The 400 K peak is attributed to either viscous sliding of grain boundaries or dislocation motion, and an activation energy of 0.3 eV was measured<sup>3</sup>. Niblett-Wilks and Bordoni relaxations, with activation energies of 0.16 eV and 0.27 eV respectively, have been reported for single crystal Pd<sup>30</sup>. The temperature of the center of the loss peaks for nc-Pd shift to higher temperatures with higher resonant frequency, which is characteristic of a thermally activated loss process.

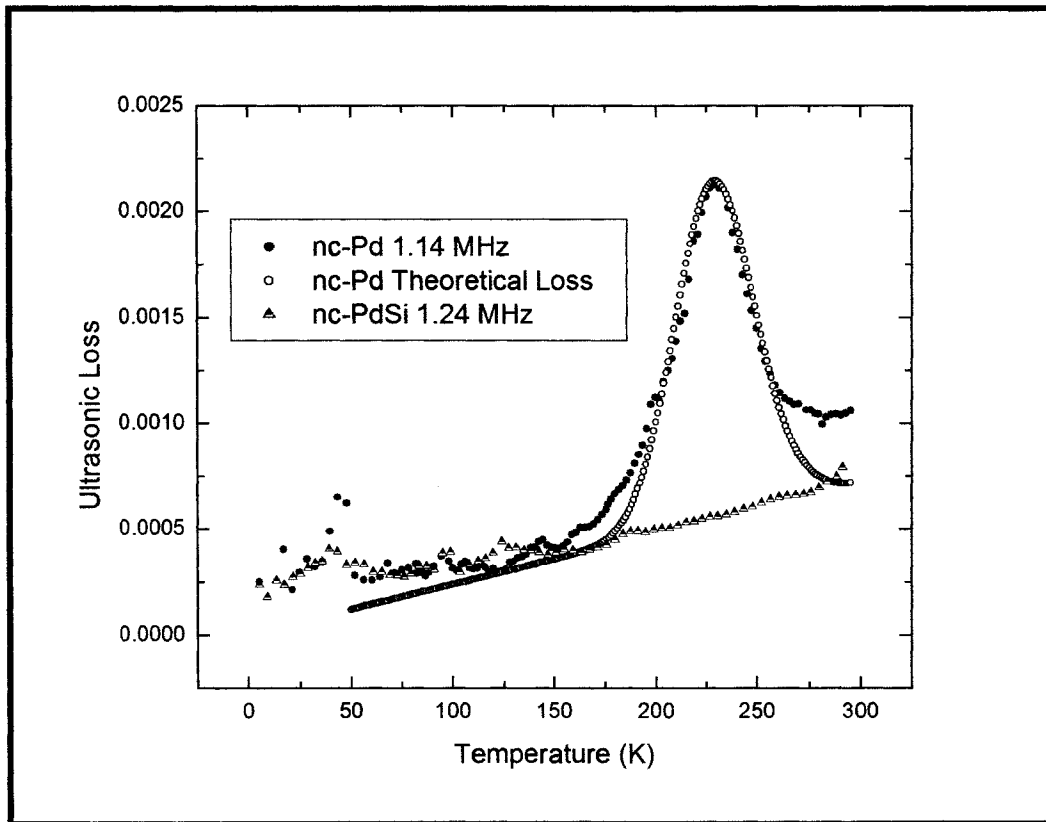


Fig. 4.6 Measured and theoretical ultrasonic loss versus temperature for the room temperature resonance of  $f_0 = 1.138$  MHz (nc-Pd) and measured loss versus temperature for  $f_0 = 1.240$  MHz (nc-PdSi). Fitting parameters are  $E_a = 0.78$  eV,  $\tau_0 = 5.56 \times 10^{-24}$  s,  $\sigma = 0.09$  eV,  $\Delta c/c = 8.80 \times 10^{-3}$ .

## 4.4 Conclusions

The elastic constants of nanocrystalline palladium (nc-Pd) and silicon-stabilized nanocrystalline palladium (nc-PdSi) were measured in the temperature range 4-300K using the technique of Resonant Ultrasound Spectroscopy. The results for nc-Pd were compared to earlier measurements of the bulk modulus and Young's modulus for similar nanocrystalline forms of Pd. These results were also compared to the polycrystalline averages for Pd, calculated from the single crystal values. The measured bulk modulus for nc-Pd is 35.1-40.0% lower than corresponding values calculated for polycrystalline Pd. The measured shear modulus is 17.8-18.6% lower than pc-Pd. The elastic moduli for nc-Pd exhibit significant anelastic effects, while the elastic moduli for nc-PdSi do not. A loss peak centered near 264 K in nc-Pd is suppressed in nc-PdSi, indicating the loss mechanisms are due to grain boundary effects. The center frequency of the loss peaks show a temperature shift, with higher frequency peak centered at higher temperatures, indicating a thermally activated process. The room temperature elastic constant values reported here compare favorably with values reported in earlier studies, despite average grain sizes that are 10-20 times larger. A non-physical attempt frequency, calculated from curve fitting of a loss peak and the temperature dependence of a resonant frequency, is attributed to a distribution of coupled loss mechanisms with different activation energies due to differing local atomic environments at the grain surfaces.

## References

- <sup>1</sup> R.R. Yadav, D.K. Pandey, *Mat. Lett.*, **59**, 564-569 (2005).
- <sup>2</sup> M. J. Lang, M. Duarte-Dominguez, R. Birringer, R. Hempelmann, H. Natter and W. Arnold, *NanoStruc. Mat.*, **12**, 811-816 (1999).
- <sup>3</sup> M. Weller, J. Diehl and H.-E. Schaefer, *Phil. Mag. A*, **63** (3), 527-533 (1991).
- <sup>4</sup> H.E. Schaefer, R. Würschum, R. Birringer, H. Gleiter, *J. Less-Comm. Met.*, **140**, 161-169 (1988).
- <sup>5</sup> D. Korn, A. Morsch, R. Birringer, W. Arnold and H. Gleiter, *J. de Physique*, **49** (1988).
- <sup>6</sup> X.R. Zhang, X.Y. Qin, G.S. Cheng and L.D. Zhang, 1996 IEEE Ultrasonics Sym., 515-518 (1996).
- <sup>7</sup> H. Gleiter, *Acta mater.* **48**, 1-29 (2000).
- <sup>8</sup> H. Gleiter, H.E. Schaefer, R. Würschum, and R. Birringer, *J. Less-Common Metals* **140**, 161-169 (1988).
- <sup>9</sup> R. Birringer, *Mat. Sci. and Eng.*, **A117**, 33-34 (1989).
- <sup>10</sup> J. Weismüller, *Mat. Sci. and Eng.*, **A179/A180**, 102-107 (1994).
- <sup>11</sup> H. Gleiter, *J. Less-Common Met.*, **140**, 161-169 (1988).
- <sup>12</sup> C.E. Krill and R. Birringer, *Mat. Sci. Forum*, **225-227**, 263-274 (1996).
- <sup>13</sup> A. Tschöpe, R. Birringer and H. Gleiter, *J. Appl. Phys.* **71**, 5394-5394 (1992).
- <sup>14</sup> J. Weismüller, *Proc. 22<sup>nd</sup> Risø Int. Sym. On Mat. Sci.*, 155-176 (2001).
- <sup>15</sup> J. Löffler and J. Weismüller, *Phys. Rev. B*, **52** (10), 7076-7093 (1994).
- <sup>16</sup> R. Würschum, K. Reimann, S. Grub, A. Kübler, P. Scharwaechter, W. Frank, O. Kruse, H.D. Carstjen and H.-E. Schaeffer, *Philos. Mag. B*, **76** (4), 407-417 (1997).
- <sup>17</sup> D.K. Hsu and R.G. Leisure, *Phys. Rev. B*, **20** (4), 1339-1344 (1979).
- <sup>18</sup> H.M. Ledbetter, *J. Phys. D: Appl. Phys.*, **13**, 1879-1884 (1980).
- <sup>19</sup> J.A. Eastman, M.R. Fitzsimmons, and L.J. Thompson, *Philisop. Mag. B* **66** (5), 667-696 (1992).
- <sup>20</sup> J.A. Rayne, *Phys. Rev.* **118** (6), 1545-1549 (1960).
- <sup>21</sup> Y.P. Varshni, *Phys. Rev. B*, **2** (10), 3952-3958 (1970).
- <sup>22</sup> C. Weinmann and S. Steinmann, *Solid State Commun.*, **15**, 281 (1974).
- <sup>23</sup> A. Migliori and J.L. Sarrao, *Resonant Ultrasound Spectroscopy*, Wiley, New York (1997).
- <sup>24</sup> E. Bonetti, E.G. Campari, L. DelBianco, L. Pasquini, and E. Sampaolesi, *Nanostruct. Mat.*, **11** (6), 79-720 (1999).
- <sup>25</sup> H. Tanimoto, S.Sakai, and H. Mizubayashi, *Mat. Sci. Eng. A*, **370**, 135-141 (2004).
- <sup>26</sup> E. Bonetti and G. Valdre, *Phil. Mag.*, **B68**, 967 (1993).
- <sup>27</sup> B. Cai, Q.P. Kong, P. Cui, H.T. Cong and X.K. Sun, *Scripta Mater.* **44**, 1043-1048 (2001).
- <sup>28</sup> K. Foster, J.E. Hightower, R.G. Leisure, A.V. Skripov, *J. Phys.: Condens. Matter*, **13**, 7327 (2001).
- <sup>29</sup> A.S. Nowick in *Progress in Metal Physics vol. 4*, edited by Bruce Chalmers, Pergamon Press LTD, London (1953).
- <sup>30</sup> G. Hauptmann, W. Ulfert and H. Kronmüller, *Mat. Sci. Forum* **119-121**, 171-176 (1993).

## Chapter 5

### **bcc Ta<sub>0.33</sub>V<sub>0.67</sub> random alloy**

- 5.1 Introduction
- 5.2 Experimental details
- 5.3 Results and discussion
- 5.4 Conclusions
- References

#### **5.1 Introduction**

Random alloys are metallic compounds which do not exhibit chemical ordering of its component atoms; any lattice position may be inhabited by any of the chemical species comprising the compound. In this study I compare the temperature dependence of the elastic constants of a random alloy, bcc Ta<sub>0.33</sub>V<sub>0.67</sub> to a form with identical relative amounts of chemical species, the Laves-phase C15 TaV<sub>2</sub>. Laves-phase materials form a sub-group of the topologically close packed (TCP) compounds, and are further subdivided into C14 (hexagonal), C15 (cubic) or C36 (mixed) structures. C15 intermetallic compounds are of technological interest due to their low densities, high melting temperatures, and their ability to absorb hydrogen <sup>1</sup>. TaV<sub>2</sub> has a maximum hydrogen absorbed to metal atom ratio of approximately 0.60, while the bcc form has a value of approximately 1.65 for this ratio <sup>2</sup>. Hydrogen

absorbed in the C15 and bcc forms form a solid solution. Laves-phase forms generally have a higher packing density than the bcc form<sup>3</sup>, and differences in the elastic properties of these two compounds are expected. The theoretical density of bcc Ta<sub>0.33</sub>V<sub>0.67</sub>, based on lattice parameter<sup>4</sup>  $a_0 = 3.1273 \times 10^{-10}$  m, is 10.190 g/cm<sup>3</sup>, and the measured density for the material used in this study is 10.195 g/cm<sup>3</sup>. The theoretical density of C15 TaV<sub>2</sub>, calculated from the room temperature lattice parameter<sup>7</sup> is 10.249 g/cm<sup>3</sup>, and the measured density reported in reference 7 is 9.815 g/cm<sup>3</sup>.

The shear modulus and Young's modulus of C15 TaV<sub>2</sub> exhibit an unusual temperature dependence over the temperature range 4-435 K, increasing with increasing temperature. This effect is attributed to electronic effects associated with symmetries in the C15 structure, which produce doubly degenerate electron energy levels. The model used to explain this effect depends strongly on the difference between the energy of the double-degeneracy level and the Fermi level<sup>7</sup>. The purpose of this study was to measure elastic constants of the random alloy form, bcc Ta<sub>0.33</sub>V<sub>0.67</sub>, and compare their temperature dependence to the results for TaV<sub>2</sub>. The symmetries of the random alloy structure are not the same as the Laves-phase C15 structure, so a different, less anomalous temperature dependence is expected. In addition, a Snoek-type loss peak was measured for C15 TaV<sub>2</sub>H<sub>x</sub>, despite the absence of this peak for hydrogen in single crystal Ta<sup>5</sup>. The inequality of the tetrahedral interstitial sites in bcc Ta<sub>0.33</sub>V<sub>0.67</sub> is expected to display a Snoek-type relaxation peak when hydrogen is absorbed in the material. Ultrasonic loss for bcc Ta<sub>0.33</sub>V<sub>0.67</sub>H<sub>0.045</sub> was measured in this study and compared to C15 TaV<sub>2</sub>H<sub>x</sub>.

## 5.2 Experimental details

The random alloy, bcc  $\text{Ta}_{0.33}\text{V}_{0.67}$ , was prepared by arc melting appropriate amounts of high purity metals in a helium atmosphere <sup>6</sup>. The ultrasonic sample was cut from a small cylinder of material on a low speed diamond saw. The rough cube resulting from the saw cuts was carefully hand polished into a highly accurate parallelepiped, with dimensions 1.16 mm x 1.19 mm x 3.31 mm and a mass of 0.18 g. The sample of bcc  $\text{Ta}_{0.33}\text{V}_{0.67}$  used in this study is polycrystalline. Polycrystalline materials are elastically isotropic; only two independent elastic constants are required to describe the linear elasticity. The RUS technique was used to derive the elastic constants  $C_{11}$  and  $C_{44}$ .

## 5.3 Results and discussion

The lowest twenty-three resonant frequencies were measured to determine the elastic constants  $C_{11}$  and  $C_{44}$  of bcc  $\text{Ta}_{0.33}\text{V}_{0.67}$ . The temperature dependence of the bulk modulus  $B$  of  $\text{ZrV}_2$  is displayed in Fig. 5.1, where

$$B = C_{11} - \frac{4}{3}C_{44} \quad (1)$$

The room temperature value was determined to be  $B = 171.8$  GPa, with an rms fitting error of 0.1997%. The behavior of the bulk modulus is linear, decreasing with increasing temperature in the temperature region ~5-300 K, and approaching 0 K with zero slope, corresponding to the behavior of most metals. Figure 5.1 also displays the temperature dependence of the bulk modulus for the Laves-phase  $\text{TaV}_2$  <sup>7</sup>, which has a reported room temperature value of  $B = 194$  GPa, 13.2% higher than bcc  $\text{Ta}_{0.33}\text{V}_{0.67}$ .

The temperature dependence of the elastic constants can be modeled by the Varshni expression <sup>8,9</sup>

$$C(T) = C(0) - \frac{s}{\exp\left(\frac{T_E}{T}\right) - 1} \quad (2)$$

where  $C(0)$  is the value of the elastic constant at zero temperature,  $T_E$  the effective Einstein temperature, and  $s$  an adjustable parameter related to the strength of the anharmonic interactions. This expression is based on the assumption that the thermal phonons responsible for the anharmonic effects can be represented approximately by  $T_E$ . The solid lines in Figs. 5.1, 5.2 and 5.3 represent a fit of Eq. 2 to the data. The fit parameters are given in Table 5.1. The bulk modulus of bcc  $\text{Ta}_{0.33}\text{V}_{0.67}$  exhibits strong agreement with the Varshni expression over the entire measurement temperature range.

Table 5.1 Varshni expression fitting parameters for Bulk Modulus ( $B$ ), Shear Modulus ( $G$ ) and Young's Modulus ( $E$ ).

	$C(0)$ (GPa)	$s$ (GPa)	$T_E$ (K)	$\chi^2$
<b><math>B</math></b>	$175.13 \pm 0.08$	$1.79 \pm 0.52$	$126.5 \pm 31$	0.064
<b><math>E</math></b>	$149.74 \pm 0.06$	$1.63 \pm 0.22$	$68.9 \pm 9$	0.016
<b><math>G</math></b>	$55.76 \pm 0.07$	$0.61 \pm 0.09$	$66.4 \pm 9$	0.003

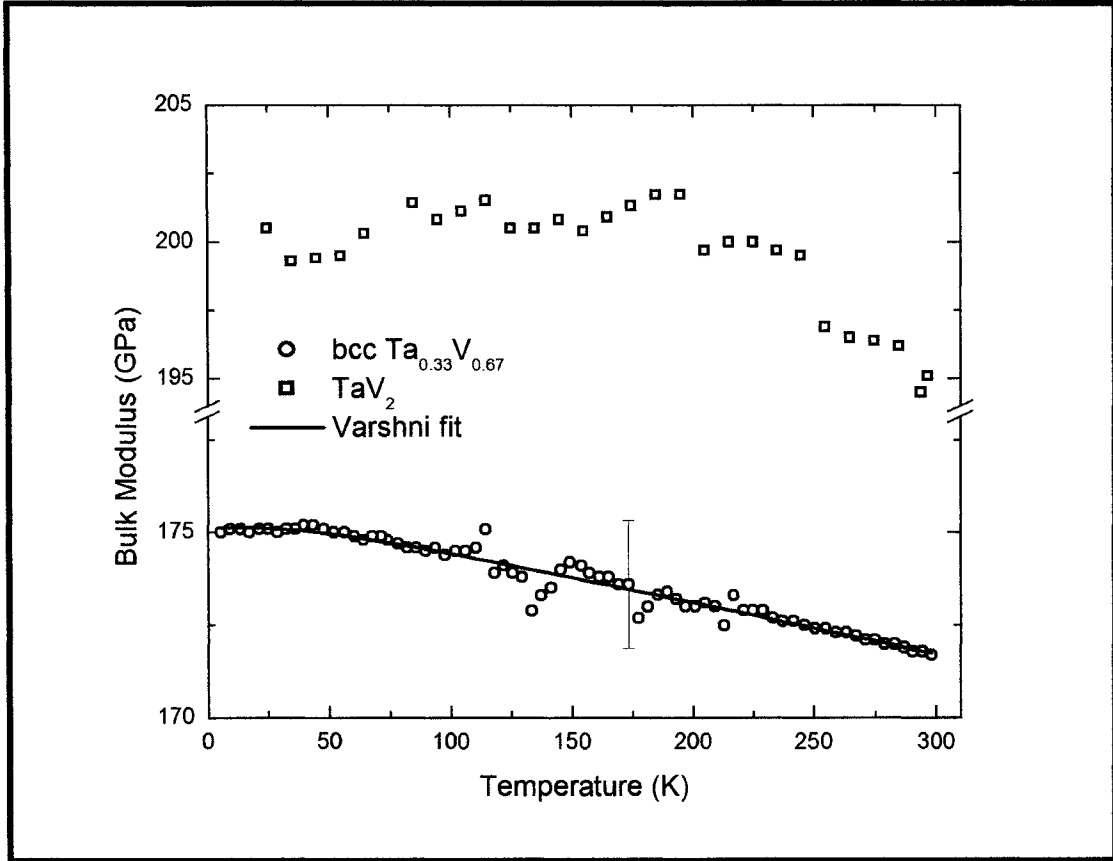


Fig. 5.1 Temperature dependence of the bulk modulus of bcc  $Ta_{0.33}V_{0.67}$ . The error was computed based on the quality of the fits and errors in mass and dimension measurements. The relative error is much smaller and represented by the scatter in the data.

The temperature dependence of the shear modulus,  $G$ , and Young's modulus,  $E$ , of bcc  $Ta_{0.33}V_{0.67}$  are displayed in Fig. 5.2, where

$$G = C_{44} \quad (3)$$

and

$$E = C_{44} \left[ \frac{3C_{11} - 4C_{44}}{(C_{11} - C_{44})} \right]. \quad (4)$$

The room temperature values were determined to be  $G = 52.9$  GPa and  $E = 143.8$  GPa. The accuracy of the shear modulus is higher than that for the bulk modulus because 20 of the first 23 resonances have a dependence on  $C_{44}$  of 92 % or higher.

The thirteenth and twentieth resonances in this set have the strongest  $C_{11}$  dependence, 13% and 15% respectively. Figure 5.2 also displays Varshni fits for both quantities using equation 2. The Varshni curve does not fit either of these data curves well, indicating a small anomaly in the temperature dependence of the  $C_{44}$  elastic constant. This deviation is attributed to electronic contributions to the strain energy, where acoustically produced strains can shift the energies of conduction-band minima. A redistribution of electron states can result in a lower Fermi energy, thereby reducing the electronic contribution to the crystal's free energy. This process impacts the elastic constants, which are the second derivative of internal energy with respect to strain<sup>10</sup>.

Figure 5.3 compares the temperature dependence of the shear modulus for bcc  $\text{Ta}_{0.33}\text{V}_{0.67}$  and C15  $\text{TaV}_2$ . Figure 5.4 compares the temperature dependence of the Young's modulus for bcc  $\text{Ta}_{0.33}\text{V}_{0.67}$  and C15  $\text{TaV}_2$ . Both the shear modulus and Young's modulus for  $\text{TaV}_2$  exhibit anomalous behavior over the temperature range reported here, increasing with increasing temperature. It has been demonstrated that for C15  $\text{TaV}_2$ , there are degeneracies in the electronic energy levels due to symmetries in the C15 structure that reside near the X point of the Brillouin zone. This affects the electronic energy levels under strain, and has a strong effect on the  $C_{44}$  elastic constant<sup>11</sup>.

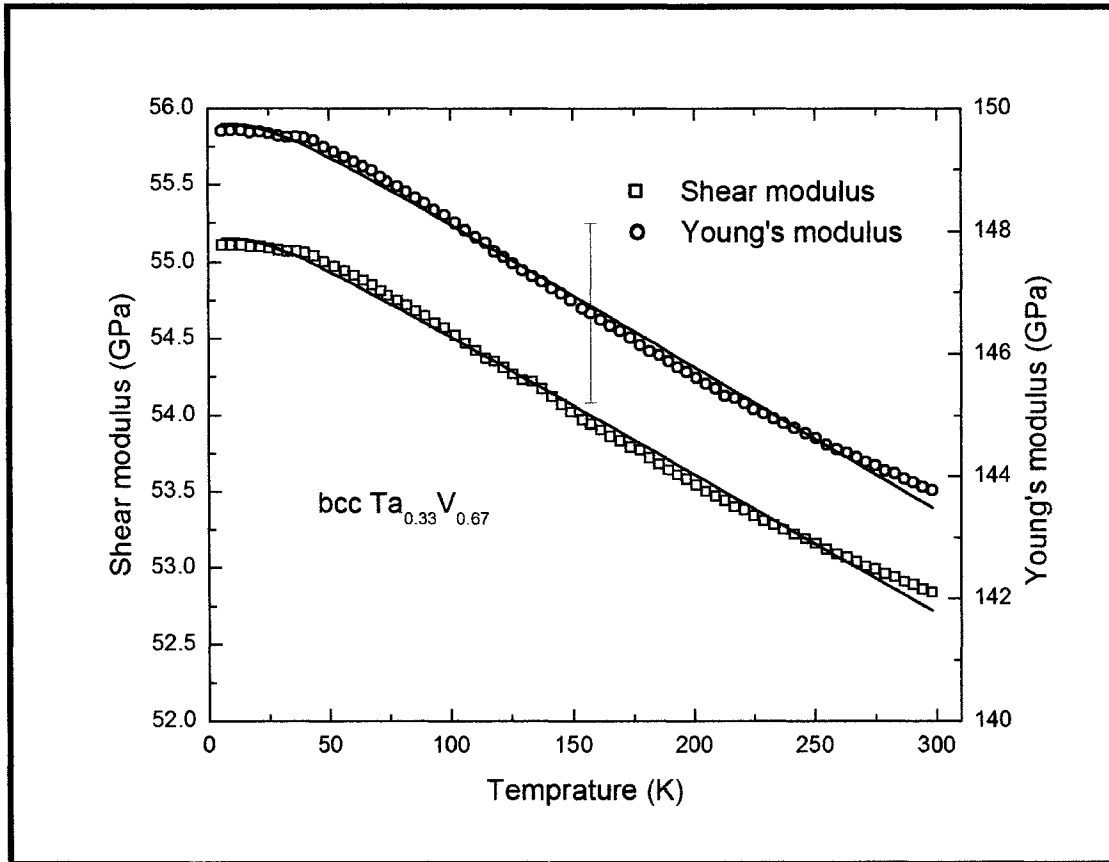


Fig. 5.2 Temperature dependence of the shear modulus and Young's modulus of bcc Ta<sub>0.33</sub>V<sub>0.67</sub>. The absolute error of 0.1% for the shear modulus is too small to show on the plot. The solid lines represent Varshni fits of the data.

Other useful elastic quantities can be calculated from the elastic constants.

Poisson's ratio  $\nu$ , given by

$$\nu = \frac{C_{11} - 2C_{44}}{2(C_{11} + C_{44})} \quad (5)$$

is displayed in Fig. 5.5.  $\nu$  is nearly temperature independent for bcc Ta<sub>0.33</sub>V<sub>0.67</sub>, and decreases with increasing temperature for C15 TaV<sub>2</sub>, which is opposite the behavior of most materials.

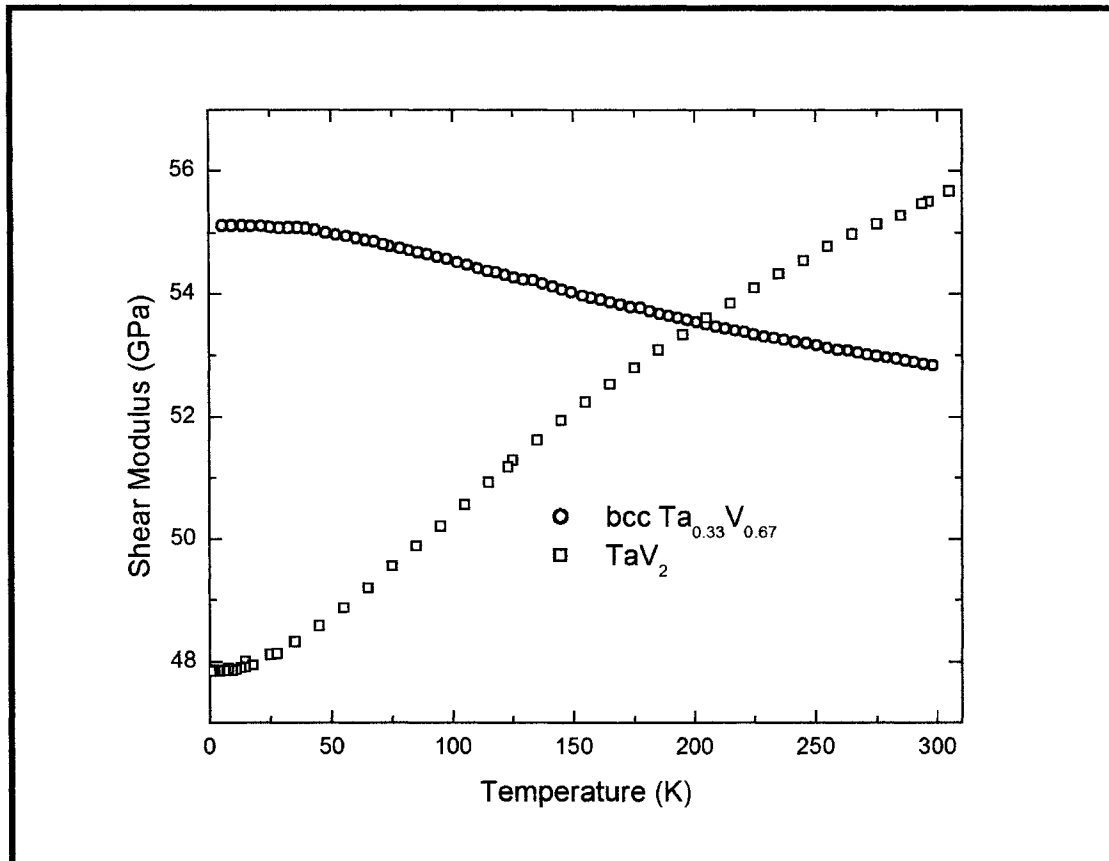


Figure 5.3 Comparison of the shear modulus,  $G$ , for bcc Ta<sub>0.33</sub>V<sub>0.67</sub> and C15 TaV<sub>2</sub>.

The elastic constants were not corrected for thermal contraction because thermal expansion data are not available for these materials; room temperature dimensions were used in the analysis. Metals such as Ta and V have a total thermal contraction between room temperature and 4 K between 0.1 and 0.2 %<sup>12</sup>. Assuming a comparable thermal contraction for these materials, the effect of the thermal contraction would be to increase the elastic constants approximately 0.10-0.20 % at 4 K over that reported in Figs. 5.1 through 5.5.

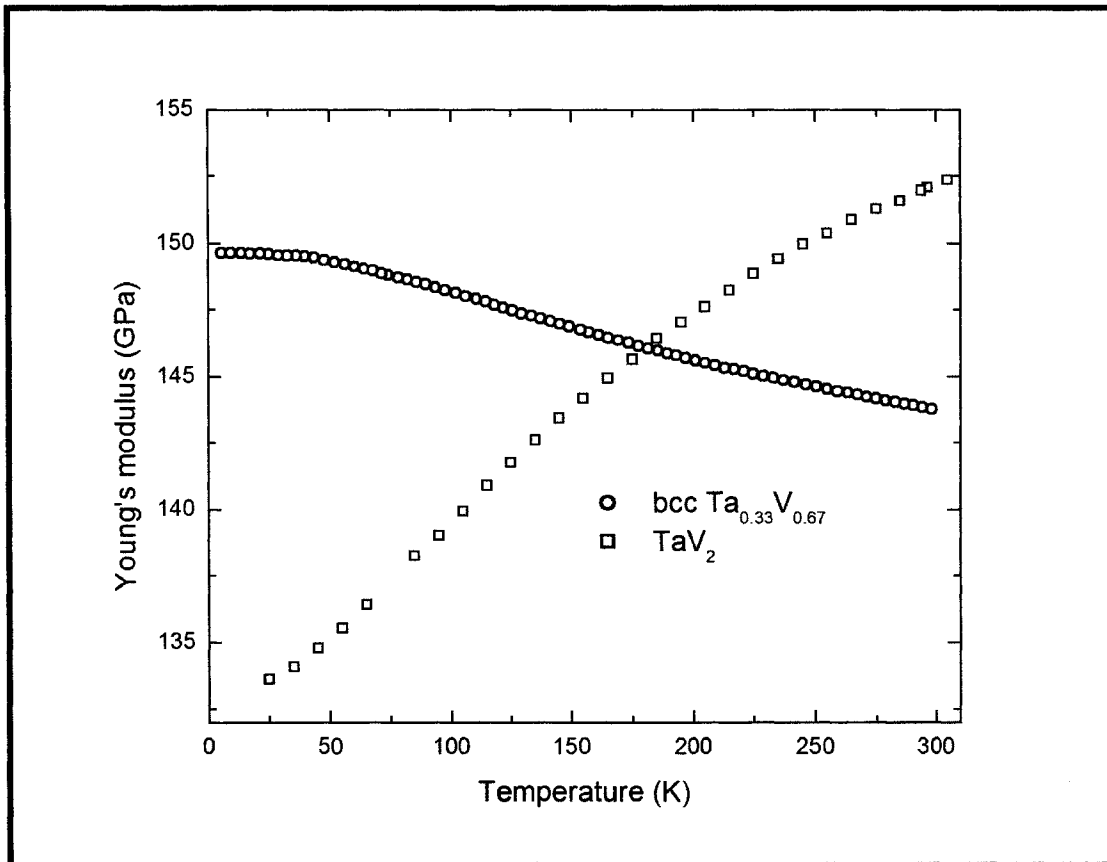


Figure 5.4 Comparison of the Young's modulus,  $E$ , for bcc  $Ta_{0.33}V_{0.67}$  and C15  $TaV_2$ .

Figure 5.6 displays the temperature dependence of the ultrasonic loss (internal friction) for bcc  $Ta_{0.33}V_{0.67}$ , bcc  $Ta_{0.33}V_{0.67}H_{0.045}$  and C15  $TaV_2$ . While the quality of the data was not high enough to permit a detailed analysis of the loss, the data do show that the hydrogenated random alloy sample exhibits a loss peak, centered somewhere in the neighborhood of 170 K, the C15 sample exhibits a loss peak near 250 K<sup>13</sup>, and the bcc sample without hydrogen does not any significant ultrasonic loss.

The loss in bcc  $Ta_{0.33}V_{0.67}H_{0.045}$  is caused by the hopping of hydrogen atoms from one interstitial site to another. The quality of the RUS scans was not high enough to make an accurate determination of the effect on the elastic constants by the

addition of hydrogen. Hydrogen absorbed in C15 TaV<sub>2</sub> increased the magnitude of the shear and Young's moduli, and generally decreased the magnitude of the bulk modulus and Poisson's ratio. Hydrogen also eliminated the anomalous temperature behavior of the shear and Young's moduli<sup>7, 12</sup>. The added electrons from the absorbed hydrogen raise the Fermi level, resulting in a normal temperature dependence of the shear and Young's moduli. Heat capacity measurements of C15 TaV<sub>2</sub>H<sub>x</sub> and TaV<sub>2</sub>D<sub>x</sub> show evidence of a low temperature phase transition<sup>14</sup>, although the C15 structure is maintained as low as 4 K for all hydrogen concentrations<sup>15</sup>.

The ultrasonic loss peaks may be modeled using a Debye expression for the ultrasonic loss,  $Q^{-1}$ , given by

$$Q^{-1} = \left( \frac{\Delta c}{c} \right) \frac{\omega \tau}{1 + \omega^2 \tau^2} \quad (6)$$

where  $\Delta c/c$  is the relaxation strength and  $Q$  is the quality factor of the resonant frequency line shape. The loss peak will be a maximum for  $\omega \tau = 1$ . The lower temperature of the bcc loss peak indicates a faster motion of the hydrogen atoms than in the Lave-phase C15 form.

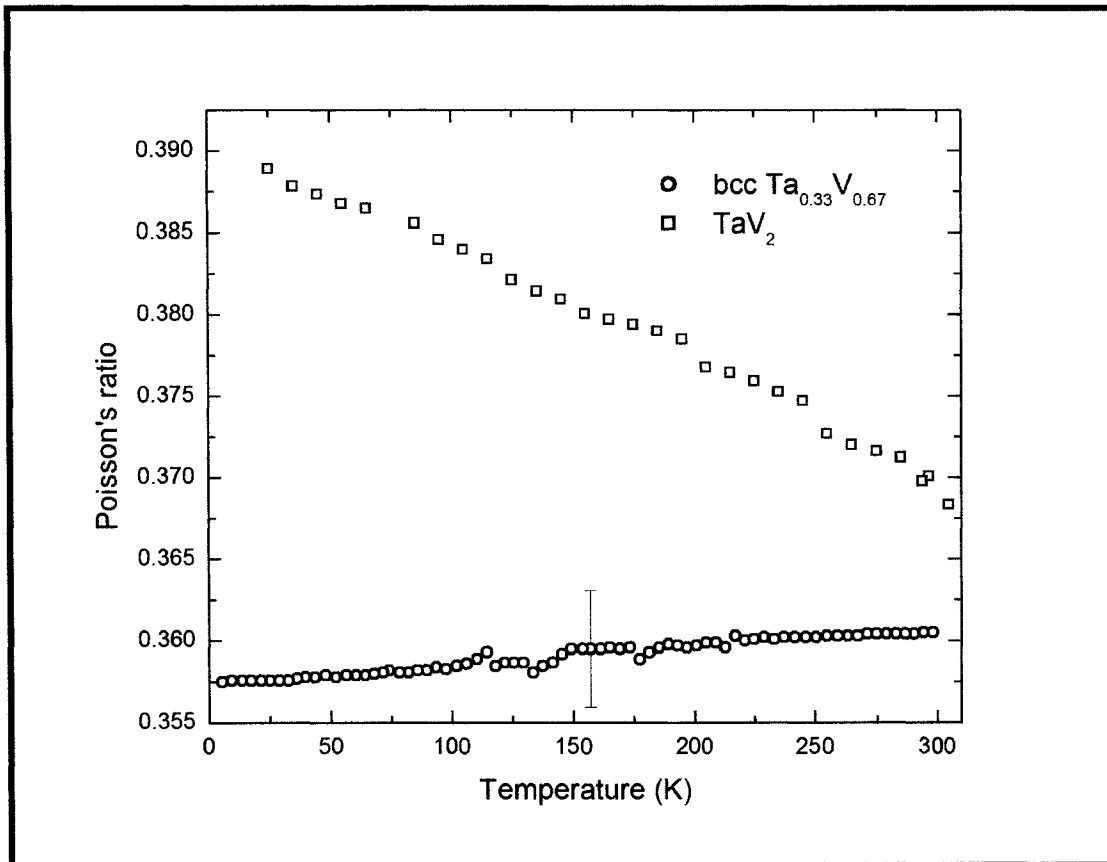


Fig. 5.5 Temperature dependence of Poisson's ratio of bcc Ta<sub>0.33</sub>V<sub>0.67</sub> and C15 TaV<sub>2</sub>. A representative error bar for the absolute accuracy is shown.

In the C15 Laves-phase structure, hydrogen atoms occupy interstitial sites. These sites have a tetrahedral symmetry, and of the three types of tetrahedral sites (as defined by the surrounding atoms) in the C15 structure, the *g* sites surrounded by two A atoms and two B atoms are usually the sites occupied by hydrogen. In TaV<sub>2</sub>H<sub>x</sub>, all of the hydrogen atoms occupy *g* sites<sup>16,17</sup>. The *g* sites form hexagonal structures, and these hexagons are linked together in another hexagonal structure. In TaV<sub>2</sub>H<sub>x</sub>, two scales of hydrogen motion have been observed. A fast localized motion of hydrogen moving from one *g* site to another *g* site, and a slower motion of hydrogen

moving from one hexagon to another, have been measured with RUS, nuclear magnetic resonance and quasielastic neutron scattering<sup>18, 19, 20, 21, 22, 23, 24</sup>.

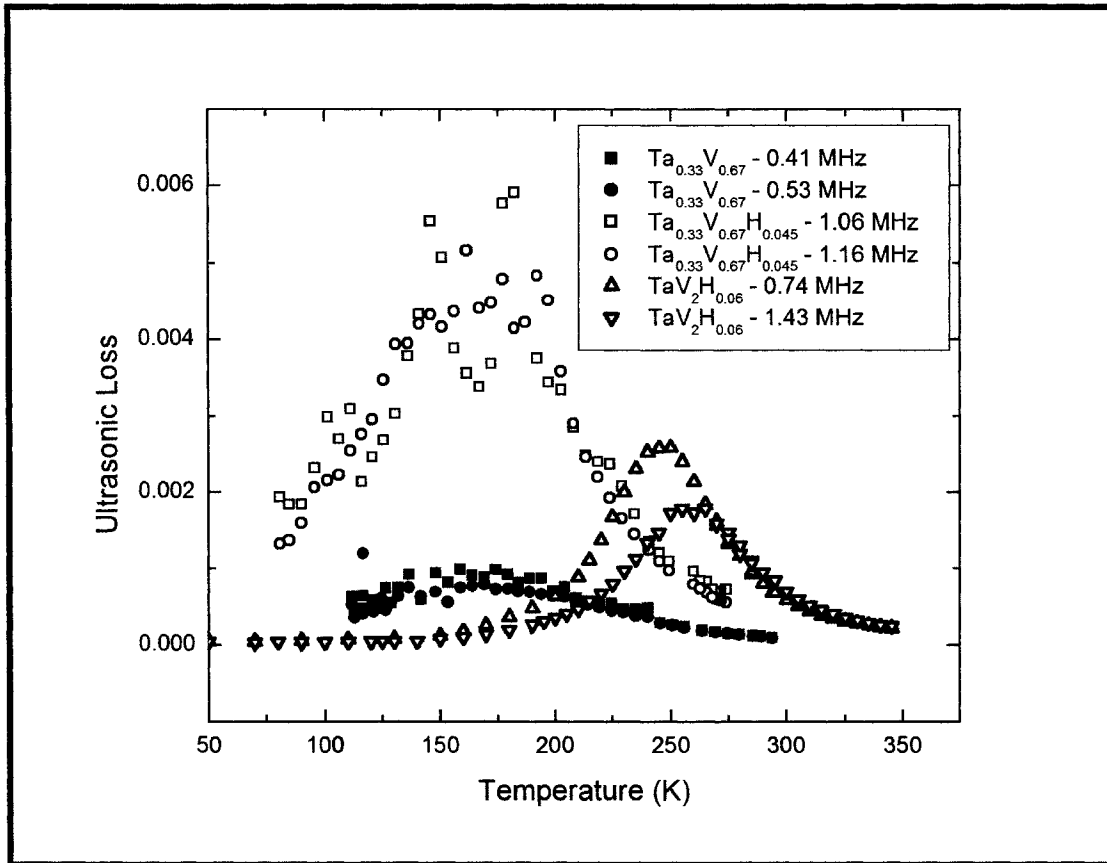


Fig. 5.6 Ultrasonic loss (internal friction) for bcc  $Ta_{0.33}V_0$ , bcc  $Ta_{0.33}V_{0.67}H_{0.045}$  and C15  $TaV_2H_{0.06}$  as a function of temperature.

The symmetry of the tetrahedral interstitial sites in C15 compounds satisfy the conditions of the Snoek effect, in which nearby sites respond differently to an applied stress, resulting in anelastic relaxation of the interstitial atoms<sup>13</sup>. This effect is not observed for hydrogen in single crystal Ta, although it is observed for heavier interstitial atoms. The most likely explanation for the suppression of the Snoek effect in Ta is that the hydrogen atoms exert forces on the host lattice atoms that maintain a cubic stress field despite tetragonal symmetry of the tetrahedral sites<sup>5</sup>.  $TaV_2H_x$

exhibits ultrasonic loss peaks associated with the movement of the hydrogen atoms among interstitial  $g$  sites<sup>13</sup>.

The interstitial sites in bcc  $\text{Ta}_{0.33}\text{V}_{0.67}$  are inequivalent due to the disordered nature of the crystal structure, and the strain field due to the interstitial hydrogen atoms is not expected to be cubic. Neighboring tetrahedral sites in the bcc alloy should respond differently to an applied stress, satisfying the condition of the Snoek effect<sup>13</sup>. Ultrasonic loss due to anelastic relaxation is expected and observed for hydrogen in this material. Nuclear magnetic resonance studies indicate that a distribution of relaxation mechanisms, with a corresponding distribution of relaxation times, exist in bcc  $\text{Ta}_{0.33}\text{V}_{0.67}\text{H}_x$ <sup>25</sup>.

## 5.4 Conclusions

The temperature dependence of the elastic constants of bcc  $\text{Ta}_{0.33}\text{V}_{0.67}$  was measured in the temperature range 5-300 K. These results were compared to similar studies of Laves-phase C15  $\text{TaV}_2$ . The temperature dependence of the bulk modulus of bcc  $\text{Ta}_{0.33}\text{V}_{0.67}$  exhibits strong agreement with the semi-empirical Varshni expression, while the shear modulus and Young's modulus deviate significantly from this theoretical curve. This behavior is attributed to the anomalous behavior of the  $C_{44}$  elastic constant due to electronic effects. Laves-phase C15  $\text{TaV}_2$  also exhibits an anomalous temperature dependence of  $G$  and  $E$ , but where  $\text{TaV}_2$  exhibits a decreasing modulus with decreasing temperature, bcc  $\text{Ta}_{0.33}\text{V}_{0.67}$  exhibits an increasing modulus with decreasing temperature. The symmetries found in the C15 structure, which produce doubly degenerate electron energy levels very close to the Fermi level, do

not exist in bcc  $\text{Ta}_{0.33}\text{V}_{0.67}$ . The electronic effects which strongly impact the  $C_{44}$  elastic constant in C15  $\text{TaV}_2$  are highly suppressed in the random alloy form, resulting in a temperature dependence of the shear and Young's moduli that are only slightly anomalous and which display a more normal behavior. The bcc form is also able to absorb almost three times as much hydrogen than the Laves-phase C15 form. Ultrasonic loss associated with the movements of hydrogen atoms between interstitial tetrahedral sites is observed for bcc  $\text{Ta}_{0.33}\text{V}_{0.67}\text{H}_{0.045}$  in the 170 K temperature region, and is not observed for bcc  $\text{Ta}_{0.33}\text{V}_{0.67}$ . The ultrasonic loss is attributed to the Snoek effect. The loss peaks for  $\text{TaV}_2\text{H}_{0.06}$  occur near 250 K, indicating a faster rate of hydrogen motion for the bcc random alloy.

## References

- 
- <sup>1</sup> F. Chu, T.E. Mitchell, S.P.Chen, M. Sob, R. Siegl, and D.P. Pope, *J. of Phase Equilibria*, **18** (6), 536-543 (1997).
  - <sup>2</sup> J.F. Lynch, *J. of Less-Common Metals*, **74**, 455 (1980).
  - <sup>3</sup> P. Haasen, *Physical Metallurgy, 3<sup>rd</sup> Ed.*, (Cambridge University Press, Cambridge, 1996), Chapter 6.
  - <sup>4</sup> A.L. Shilov, et. al., *Russian J. of Inorg. Chem.*, **45** (9), 1402 (2002).
  - <sup>5</sup> J. Buchholz, J. Völkl and G. Alefeld, *Phys. Rev. Lett.*, **30** (8), 318-321 (1973).
  - <sup>6</sup> A.V. Skripov, M. Yu. Belyaev, A.P. Stepanov, L.N. Padurets and E.I. Sokolova, *J. Alloys and Compounds*, **190**, 171-179 (1993).
  - <sup>7</sup> K. Foster, J.E. Hightower, R.G. Leisure, and A.V. Skripov, *Phil. Mag. B*, **80** (9), 1667-1679 (2000).
  - <sup>8</sup> Y.P. Varshni, *Phys. Rev. B*, **2** (10), 3952 (1970).
  - <sup>9</sup> H. Ledbetter, in: R.P. Reed, A.F. Clark (Eds.), *Materials at Low Temperatures*, American Society for Metals, Metals Park, OH, (1983).
  - <sup>10</sup> J.J. Hall, *Phys. Rev.*, **161** (3), 756-761 (1967).
  - <sup>11</sup> K. Foster, J.E. Hightower, R.G. Leisure, and A.V. Skripov, *Phys. Rev. B*, **65**, 094108 (2002).
  - <sup>12</sup> G. K. White, *Experimental techniques in low-temperature physics* (Clarendon, Oxford, 1968).
  - <sup>13</sup> K. Foster, R.G. Leisure, and A.V. Skripov, *J. Phys.: Condens. Mater*, **11**, 799-806 (1999).

- 
- <sup>14</sup> A.V. Skripov, A.V. Mirmelshtein, M.Yu. Belyaev, *Solid State Comm.*, **81** (8), 689-691 (1992).
- <sup>15</sup> K. Foster, J.E. Hightower, R.G. Leisure and A.V. Skripov, *J. Phys. Condens. Matter*, **13**, 7327-7341 (2001).
- <sup>16</sup> V.A. Somenkov and A.V. Irdova, *J. Less-Common Met.*, **101**, 481 (1984).
- <sup>17</sup> P. Fischer, F. Fauth, A.V. Skripov, A.A. Podlesnyak, L.N. Padurets, A.L. Shilov and B. Ouladdiaf, *J. Alloys and Compounds*, **253/254**, 282 (1997).
- <sup>18</sup> A.V. Skripov, M. Pionke, O. Randle and R. Hempelmann, *J. Phys. Condens. Matter*, **11**, 1489 (1999).
- <sup>19</sup> K. Foster, R.G. Leisure and A.V. Skripov, *J. Phys. Condens. Matter*, **11**, 799 (1999).
- <sup>20</sup> R.C. Bowman, B.D. Craft, A. Attalla and J.R. Johnson, *Int. J. Hydrogen Energy*, **8**, 801 (1983).
- <sup>21</sup> A.V. Skripov, S.V. Rychkova, M. Yu. Belyaev and A.P. Stepanov, *J. Phys. Condens. Matter*, **2**, 7195 (1990).
- <sup>22</sup> A.V. Skripov, M. Yu. Belyaev, S.V. Rychkova and A.P. Stepanov, *J. Phys. Condens. Matter*, **3**, 6227 (1991).
- <sup>23</sup> A.V. Skripov, M. Yu. Belyaev, S.V. Rychkova and A.P. Stepanov, *J. Phys. Condens. Matter*, **1**, 2121 (1989).
- <sup>24</sup> A.V. Skripov, J.C. Cook, C. Karmonik and R. Hempelmann, *J. Phys. Condens. Matter*, **8**, 1319 (1996).
- <sup>25</sup> A.V. Skripov, M. Yu. Belyaev, A.P. Stepanov, L.N. Padurets and E.I. Sokolova, *J. Alloys and Compounds*, **190**, 171-179 (1993).

## Chapter 6

### ZrV<sub>2</sub>

- 6.1 Introduction
- 6.2 Experimental details
- 6.3 Results and discussion
- 6.4 Conclusions
- References

#### 6.1 Introduction

ZrV<sub>2</sub> is a Laves-phase (C15) compound with interesting physical properties. In addition to an ability to absorb hydrogen, ZrV<sub>2</sub> is superconducting at 8.3 K, making it one of the highest  $T_c$  superconductors of the binary cubic Laves-phase compounds<sup>1</sup>. At room temperature, ZrV<sub>2</sub> can absorb hydrogen and form a solid solution ZrV<sub>2</sub>H<sub>x</sub>, where  $0 \leq x \leq 6$ <sup>2,3</sup>. When cooled to approximately 123 K, polycrystalline ZrV<sub>2</sub> undergoes a second-order phase transition from C-15 cubic to rhombohedral<sup>4</sup>, and exhibits an internal friction peak just below the transformation temperature<sup>5</sup>. Some investigators report the phase transition as first-order based on hysteresis in resistivity, neutron diffraction or other parameters<sup>6,7</sup>, while others base their conclusion on the measurement of a small latent heat<sup>8,9</sup>. Other investigators have reported the phase transition as second-order due to a measured discontinuity in the inverse of Young's modulus and no discontinuity in volume at 123 K<sup>10</sup>. Pure

single-crystal forms of  $ZrV_2$  do not exhibit a structural phase transition when cooled from room temperature to 10 K<sup>11</sup>. Earlier studies have found anomalous behavior in the elastic constants, electrical resistivity, internal friction, and magnetic susceptibility near the transition temperature<sup>1, 5, 10, 12</sup>.

Some Laves-phase materials, such as  $HfV_2$  exhibit a Martensitic phase transition when cooled, while others, such as  $TaV_2$  do not. The structural phase transition in  $ZrV_2$  may be Martensitic, but where these transitions are usually described as first order, the experimental results presented here indicate a second-order transition for  $ZrV_2$ . A Martensitic phase transition is a reversible transformation of a crystal into a crystallographically different structure, and which can be treated in terms of displacement only. A Martensitic transition is usually initiated by a change in temperature, and the high temperature form is designated as austenite and the low temperature form martensite. In addition to a volume change, the lattice deformation produces a shape change in the transforming region, usually producing needle or plate shaped grains. A Martensitic transformation is an important component in the process of hardening of steel.

These transformations are diffusionless and involve no change in composition, occurring by nucleation and growth. In some cases, the transformation begins at a given temperature ( $T_s$ ) and as the temperature is lowered, the relative amount of the martensite increases until a final temperature ( $T_f$ ) is reached. In other cases, the transformation occurs at a single temperature and proceeds almost instantaneously (burst transition). The total deformation essentially consists of a shear parallel to an undistorted plane, and proceeds at close to the speed of sound in the material. The

distances between the atoms don't change significantly. The nearest neighbors remain the same. A simplified illustration of a Martensitic transformation is presented in Figure 6.1.

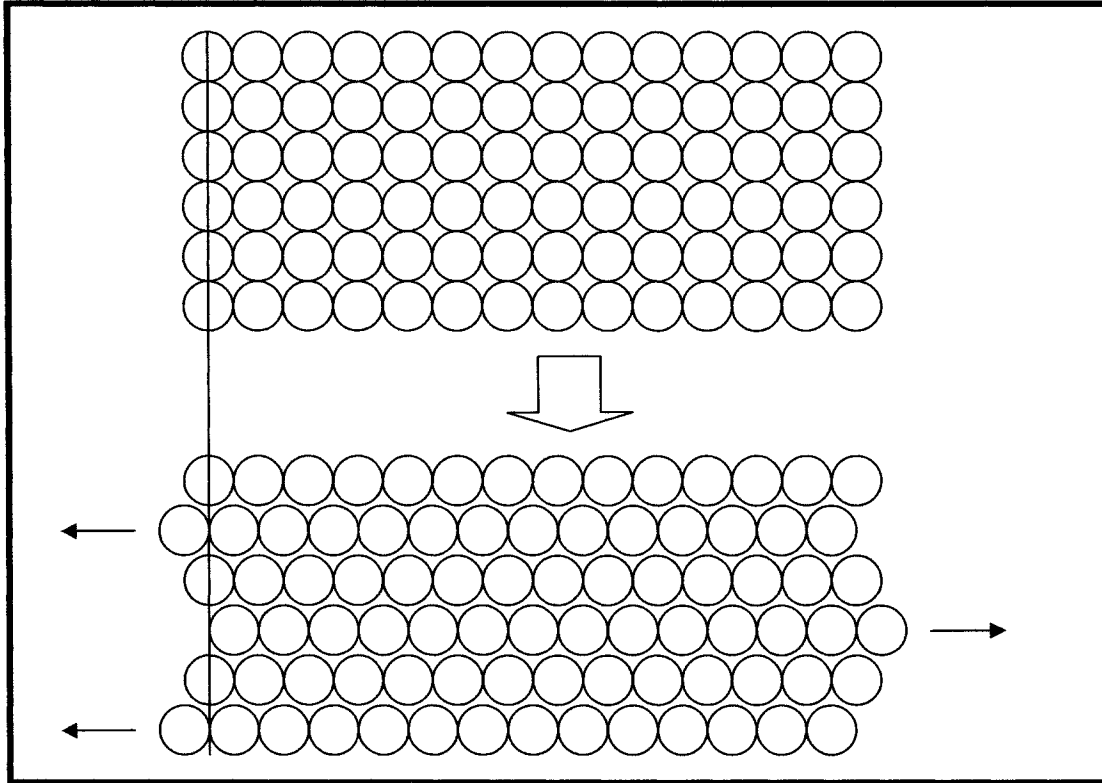


Fig. 6.1 Simplified illustration of a Martensitic transformation. The vertical line was inserted to indicate which of the atomic planes have not changed.

An actual Martensitic transition is more complicated than what is illustrated in Fig. 6.1. Atoms do move cooperatively in such as transition, but multiple atomic planes may be involved in each shear-like motion. In addition, the actual transformation may involve a slip (as illustrated above) or a twinning process. Twins are formed by a pure shear with respect to a mirror plane or rotation axis. Slip and twinning preserves the original crystal structure, but twinning reproduces the

structure with a change in orientation<sup>13, 14</sup>. Fig. 6.2 illustrates twinning in a two-dimensional lattice.

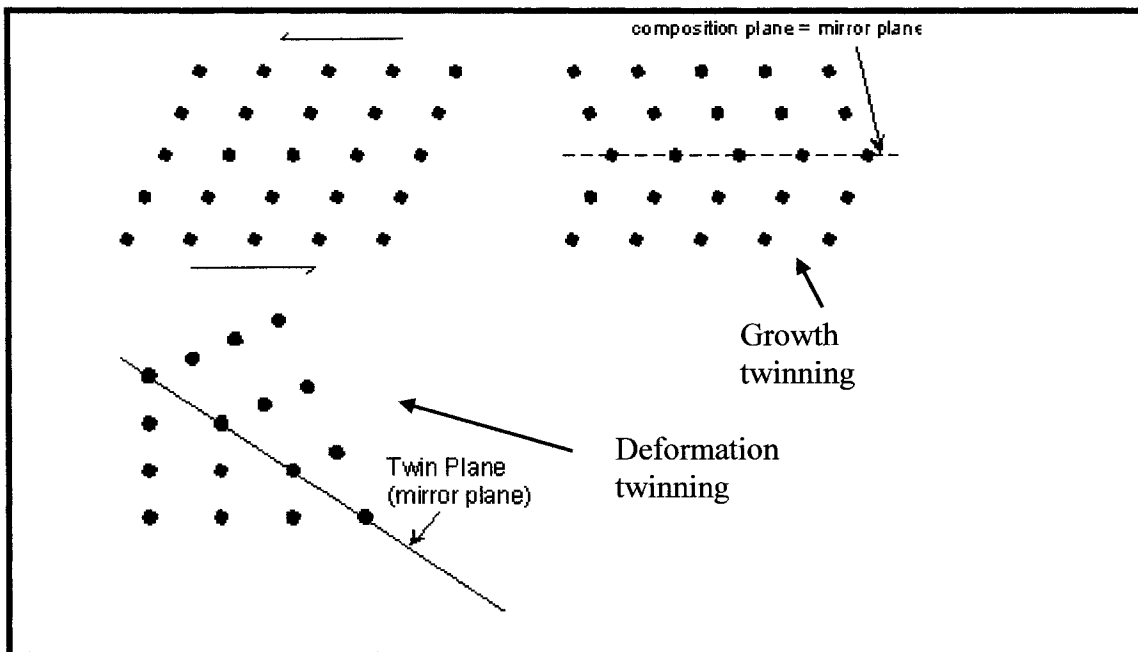


Fig. 6.2 Two-dimensional example of twinning<sup>15</sup>. *Growth twins* are the result of an interruption or change in the lattice during formation or growth due to a possible deformation from a larger substituting ion. *Transformation twins* are the result of a change in crystal system during cooling as one *form* becomes unstable and the crystal structure must re-organize or *transform* into another more stable form. *Deformation* or *gliding twins* are the result of stress on the crystal after the crystal has formed<sup>16</sup>.

An important application of some materials that undergo Martensitic phase transformations, and which exhibit long-range order and very little hysteresis when warmed, is shape memory alloys. In a shape memory alloy, a specimen which has undergone a Martensitic transformation is deformed while still at the low temperature, it reassumes its original shape when it is reheated to temperatures above that for the reverse transformation. These materials deform in such a way that the slips and twins orient in such a way as to maximize the strain. These strains are reversible when the materials is heated, reverting to the original austenite form. These materials are useful in aeronautical applications, surgical tools, electrical

actuators and sensors, and musical wires<sup>14,17,18</sup>. Materials that exhibit the shape memory effect include Ag-Cd 44/49 at.% Cd, Au-Cd 46.5/50 at.% Cd, Cu-Al-Ni 14/14.5 wt.%, Al and 3/4.5 wt.% Ni, Cu-Sn approx. 15 at.% Sn, Cu-Zn 38.5/41.5 wt.% Zn, Cu-Zn-X (X = Si,Sn,Al) a few wt.% of X, In-Ti 18/23 at.% Ti, Ni-Al 36/38 at.% Al, Ni-Ti 49/51 at.% Ni, Fe-Pt approx. 25 at.% Pt, Mn-Cu 5/35 at.% Cu, Fe-Mn-Si, Pt alloys, Co-Ni-AL, and Co-Ni-Ga<sup>19</sup>.

A sample of  $ZrV_2$  was studied in the Ultrasonics Lab at Colorado State University using the technique of Resonant Ultrasound Spectroscopy (RUS). The temperature dependence of the elastic constants exhibit anomalous behavior from room temperature to the phase transition temperature  $T_c \approx 123$  K. An internal friction (ultrasonic loss) peak was also observed, centered about the transition temperature.

## 6.2 Experimental details

Several ultrasonic samples were cut from a small cylinder of material on a low speed diamond saw. The rough cubes resulting from the saw cuts were carefully hand polished into highly accurate parallelepipeds using fine grit polishing disks.

The sample of  $ZrV_2$  used in this study is polycrystalline. Polycrystalline materials are elastically isotropic; only two independent elastic constants are required to describe the linear elasticity. The RUS technique was used to derive the elastic constants  $C_{11}$  and  $C_{44}$ .

### 6.3 Results and discussion

The lowest twenty-six resonant frequencies were measured to determine the elastic constants  $C_{11}$  and  $C_{44}$  of  $ZrV_2$ . The signal quality of all of the cryostat runs began to deteriorate below approximately 130 K due to softening of the shear modes. The RMS error in the elastic constant fits continued to rise with decreasing temperature, making measurements below about 111 K unusable. The RMS error is 0.2063% at room temperature and gradually increases with decreasing temperature to 0.2915% AT 144 K. The RMS error increases at a higher rate below this temperature, rising to 0.3548% at 129 K and 0.5009% at 111 K. Below 111 K, several resonances were not distinguishable from the background signal and others were of too low an amplitude to make an accurate measurement of the center frequency of the line shape feasible. Any statement of the values of the elastic constants below 111 K would be highly inaccurate for this data.

The temperature dependence of the bulk modulus  $B$  of  $ZrV_2$  is displayed in Fig. 6.3, where  $B = C_{11} - \frac{4}{3}C_{44}$ . The room temperature value was determined to be  $B = 135.1$  GPa. An earlier study calculated a theoretical value of  $B = 162$  GPa based on total energy vs. volume curves<sup>20</sup>. The behavior of the bulk modulus is linear, increasing with decreasing temperature in the temperature region  $\sim 170$ -300 K, corresponding to the behavior of most metals. From 170 K to the Martensitic phase transition temperature,  $T_m \approx 123$  K, the bulk modulus increases at a rapid rate with decreasing temperature, then decreasing rapidly below  $T_m$ . The quality and resolution of the data are not sufficient to determine if there is a discontinuous change in  $B$  at the phase transition. An enhanced RUS experimental setup, or another measurement

technique will be needed to characterize the low temperature behavior of  $B$  for  $ZrV_2$ . The results presented here are consistent with the anomalous behavior of the elastic constants of other materials that exhibit Martensitic transformations such as  $NiTi$ <sup>21</sup>.

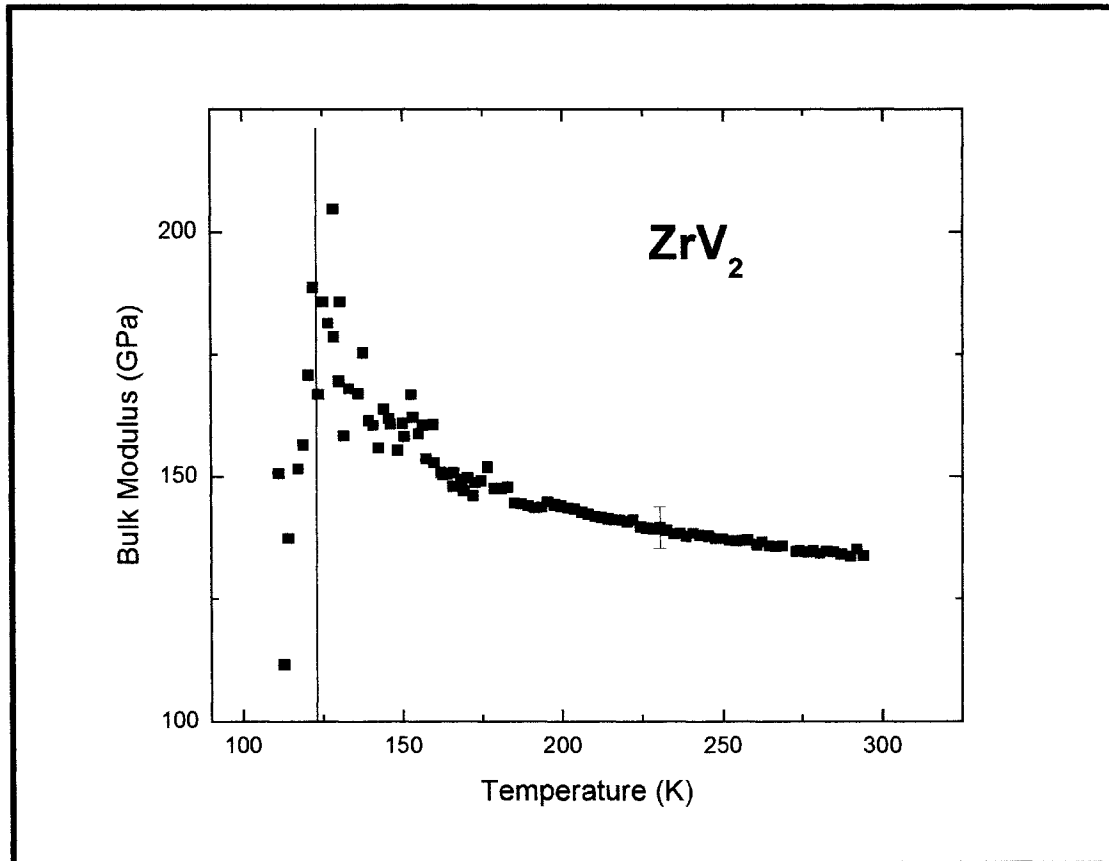


Fig. 6.3 Temperature dependence of the bulk modulus of  $ZrV_2$ . The vertical line indicates the approximate temperature of the Martensitic phase transition. A representative error bar for the absolute accuracy is shown, valid for the temperature range 144-300 K. The error below 144 K would be significantly higher. The error was computed based on the quality of the fits and errors in mass and dimension measurements. The relative error is much smaller and represented by the scatter in the data.

The temperature dependence of the shear modulus  $G$  of  $ZrV_2$  is displayed in Fig. 6.4, where  $G = C_{44}$ . The form of the shear modulus is extended below the 100 K experimental limit by calculating  $G$  from the square of the temperature dependence of a frequency for a mode that depends 100% on  $C_{44}$ .  $G$  exhibits anomalous temperature

dependence over the entire range studied, decreasing with decreasing temperature until  $T_m$  is reached, then increasing rapidly with decreasing temperature. The accuracy of the shear modulus is higher than that for the bulk modulus because all of the first 26 resonances have a dependence on  $C_{44}$  of 92 % or higher. The ninth and twenty-ninth resonances in this set have the strongest  $C_{11}$  dependence, 6.8 % and 5.1 % respectively.

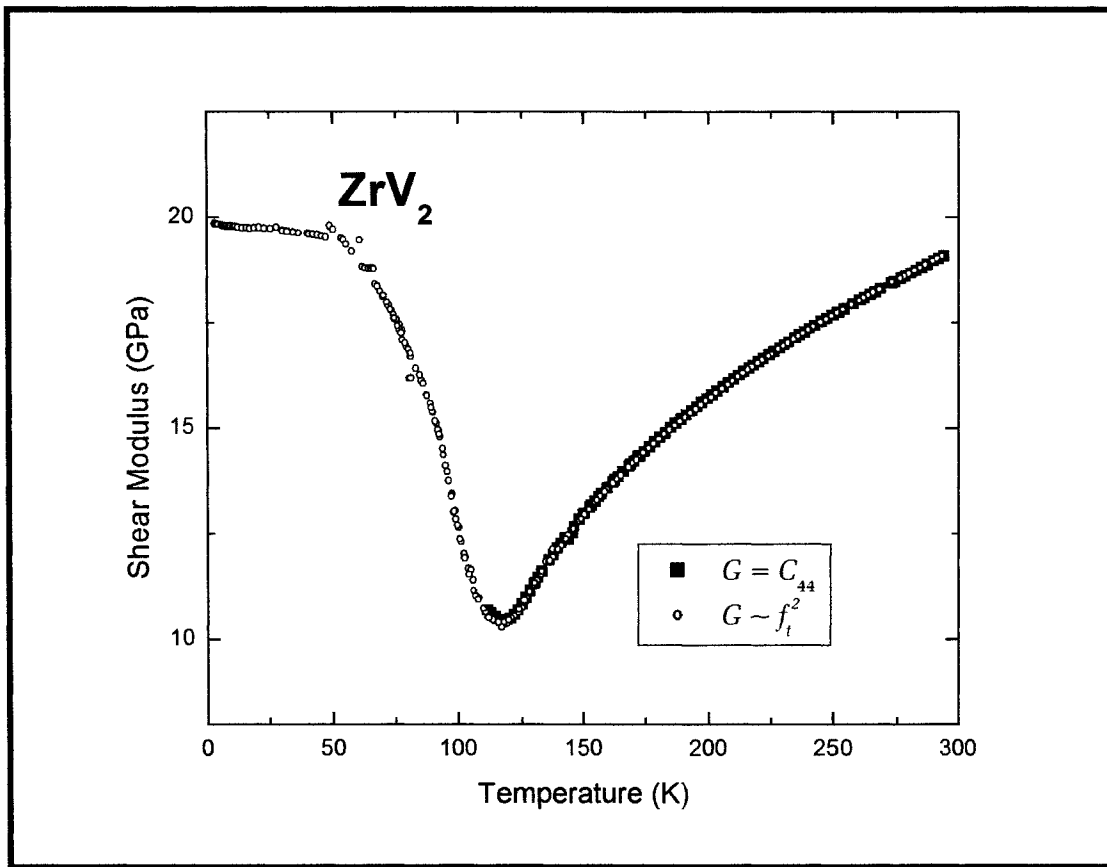


Fig. 6.4 Temperature dependence of the shear modulus of  $ZrV_2$ . The absolute error of 0.1% is too small to show on the plot.

The change in the shear modulus is continuous through the phase transition temperature, providing experimental evidence of a second-order structural phase transition. If the phase transition is first-order, a sharper, discontinuous change in the

shear modulus would be expected<sup>22</sup>. Additional evidence for a second-order transition is found in the temperature dependence of the resonant frequencies. Figures 6.5 and 6.6 display the temperature dependence of the first eight resonant frequencies of the  $ZrV_2$  sample. Hysteresis is not exhibited between the measurements taken as the sample was cooled compared to the measurements taken when the sample is warmed. The cooling and heating rates were approximately 5 K per 8-12 minutes.

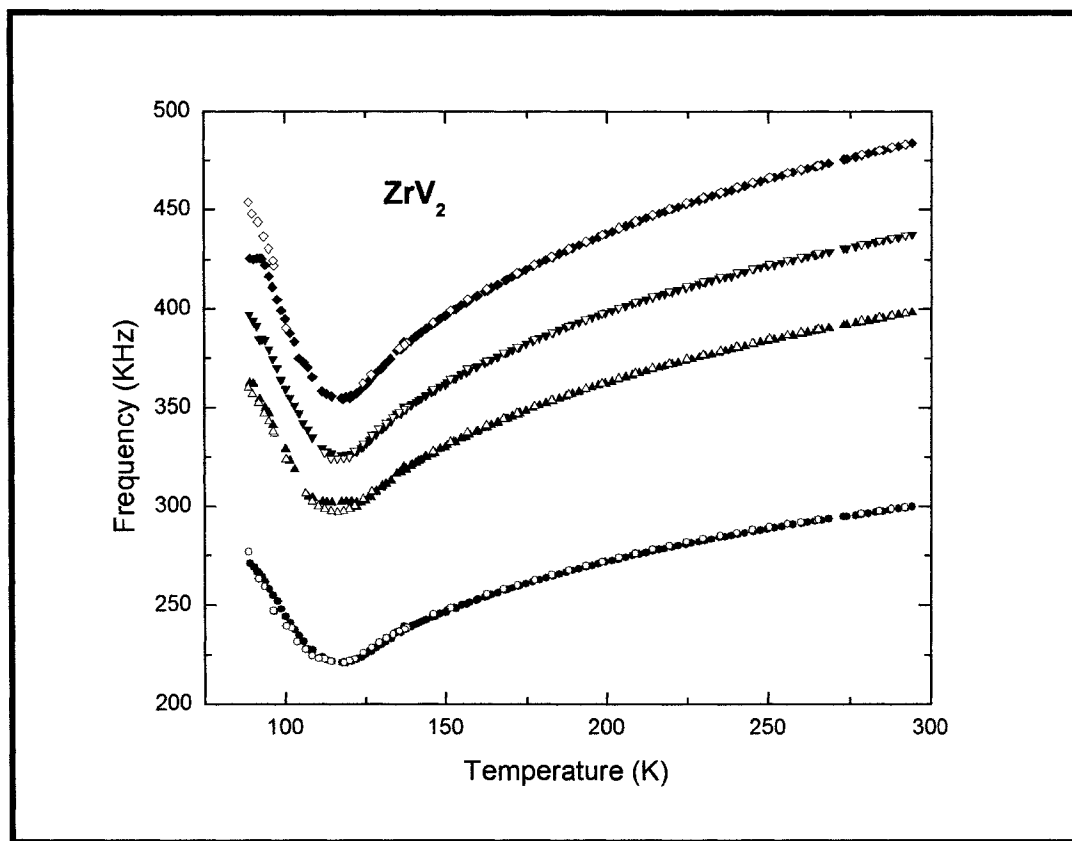


Fig. 6.5 Temperature dependence of the first four resonant frequencies of the  $ZrV_2$  sample. Filled symbols represent measurements warming the sample and open symbols measurements cooling the sample.

Other useful elastic quantities can be calculated from the elastic constants.

Figure 6.7 displays the temperature dependence of Young's modulus  $E$ , given by

$$E = C_{44} \left[ \frac{3C_{11} - 4C_{44}}{(C_{11} - C_{44})} \right]. \quad (1)$$

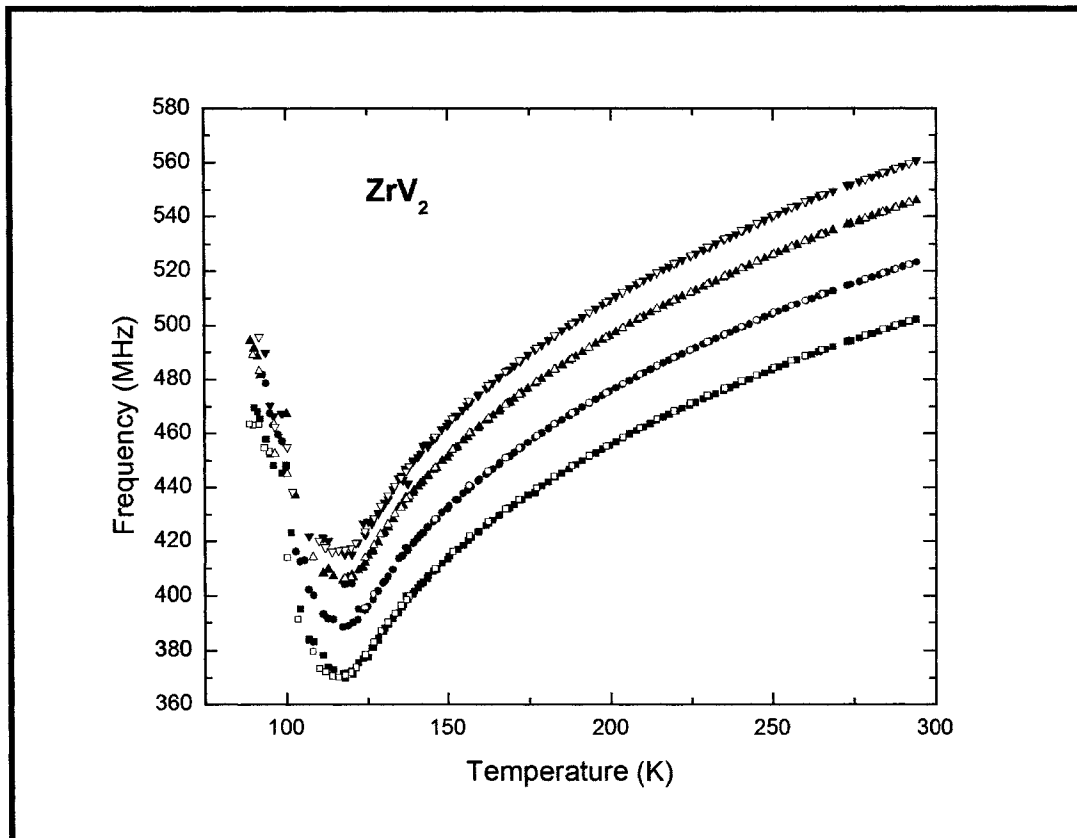


Fig. 6.6 Temperature dependence of the fifth through eight resonant frequencies of the  $ZrV_2$  sample. Filled symbols represent measurements warming the sample and open symbols measurements cooling the sample.

Young's modulus exhibits the same general temperature dependence as the shear modulus.  $E$  exhibits the same, anomalous behavior as  $G$ . Poisson's ratio  $\nu$ , given by

$$\nu = \frac{C_{11} - 2C_{44}}{2(C_{11} - C_{44})} \quad (2)$$

is displayed in Fig. 6.8.  $\nu$  exhibits the same general behavior as  $B$ .

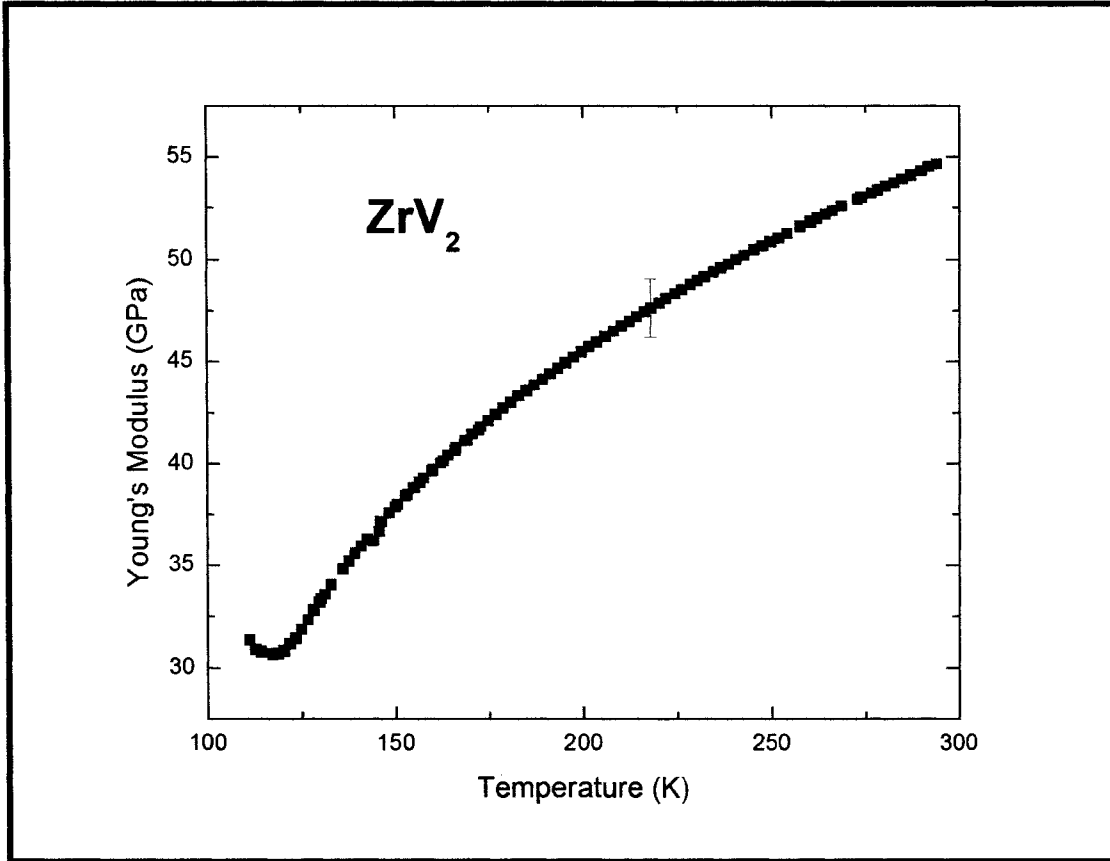


Fig. 6.7 Temperature dependence of the Young's modulus of  $ZrV_2$ . . A representative error bar for the absolute accuracy is shown.

The shape of the curve of the temperature dependence of  $E$  agrees with an earlier elastic properties study of  $ZrV_2$  using measurements of the longitudinal vibrations of samples cemented to a quartz crystal <sup>5</sup>. The values reported in that study differ significantly from those reported here. I measure  $E = 54.5$  GPa at room temperature compared to  $E \approx 31$  GPa in reference 5. At the phase transition temperature, I measure  $E_{\min} \approx 30.7$  GPa, while reference 5 reports  $E_{\min} \approx 11$  GPa.

The transition temperature in reference 5 is approximately 20 K lower than what is reported here.

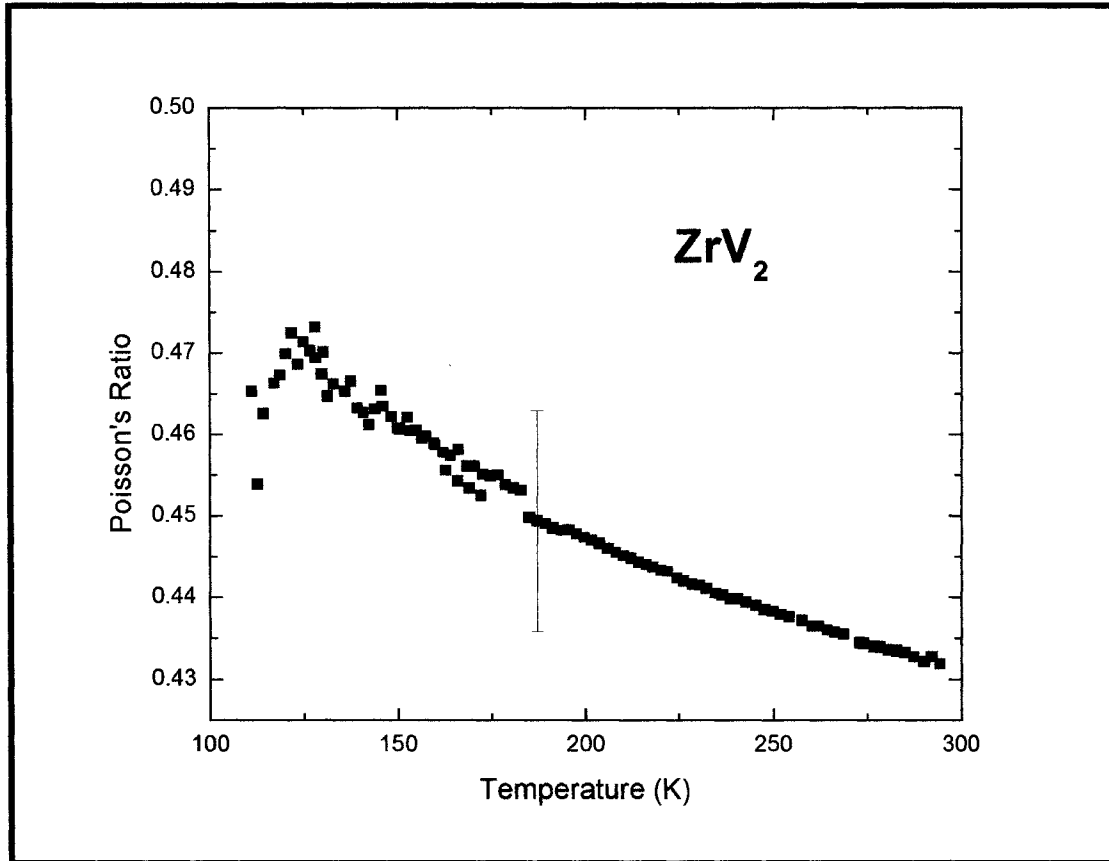


Fig. 6.8 Temperature dependence of Poisson's ratio of  $ZrV_2$ . . A representative error bar for the absolute accuracy is shown.

The internal friction (ultrasonic loss) was measured for a number of resonances by fitting the resonance line shapes to a Lorentzian expression<sup>23</sup> to determine the  $Q$ . Low signal amplitude made accurate measurement of the  $Q$  of most resonance line shapes difficult. However, the first resonance, which has a  $C_{44}$  dependence of 100% had sufficient amplitude to measure the ultrasonic loss through the entire measurement temperature range, 4-300 K. The results are given in Fig. 6.9.

The loss peak is associated with the anelastic response of the phase transition to the ultrasonic strain.

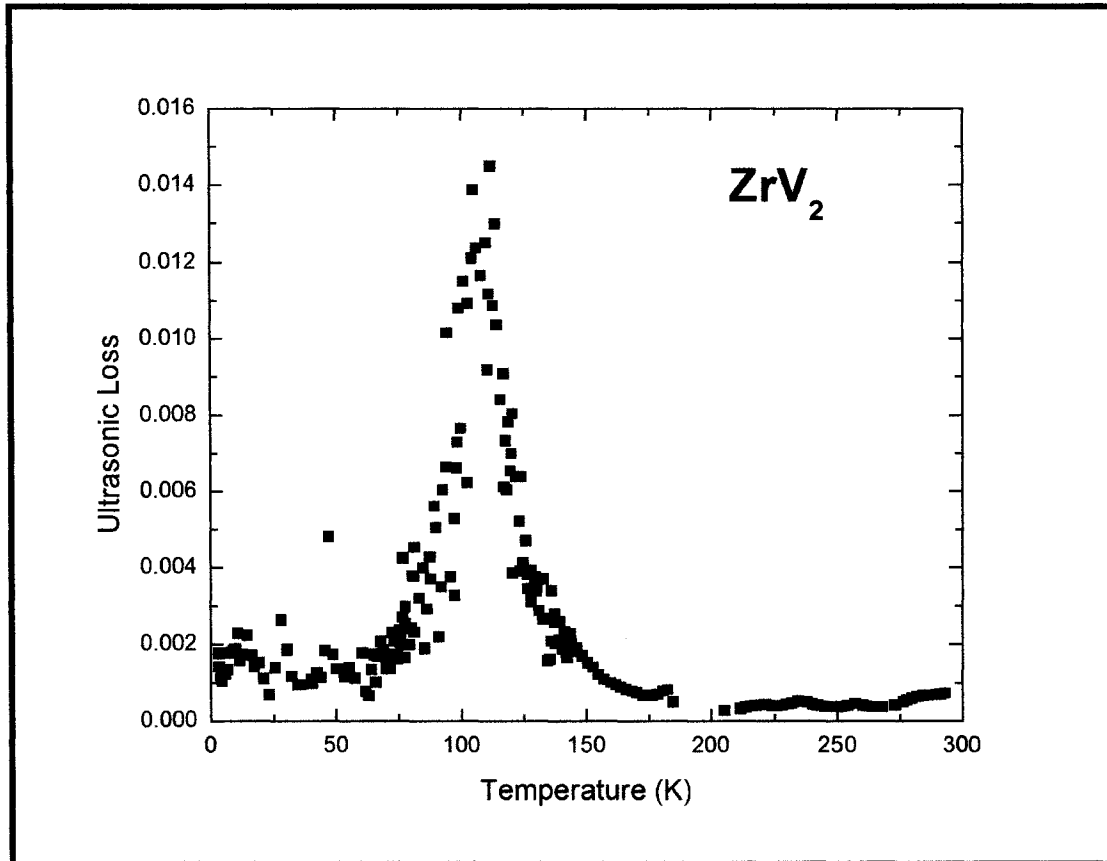


Fig. 6.9 Temperature dependence of the ultrasonic loss (internal friction) of the first resonant frequency, 0.30 MHz of  $ZrV_2$ .

The elastic constants were not corrected for thermal contraction; room temperature dimensions were used in the analysis. The thermal expansion coefficient remains fairly constant between  $T_m$  and room temperature and exhibits anomalous behavior through the phase transition region<sup>8</sup>. This effect may contribute to the loss of signal quality below 130 K.

A pulse-echo study of polycrystalline  $ZrV_2$  reported unusual temperature dependence for the longitudinal sound velocity<sup>11</sup>. The sound velocity decreases with

decreasing temperature to the phase transition point, then rises steeply with decreasing temperature, and a minimum value of  $v_l \approx 4.18 \times 10^3$  m/s is reported. The data in this study will not produce an accurate measurements of  $v_l$ , but it is estimated that

$$v_l = \sqrt{\frac{c_{11}}{\rho}} \quad (3)$$

will yield a minimum  $v_l$  in the neighborhood of  $5.3 \times 10^3$  m/s.

It is common practice to describe the acoustic contribution to the heat capacity in terms of a Debye temperature  $\theta_D$ . The Debye temperature is

$$\theta_D = \left[ 6\pi^2 \frac{N}{V} \right]^{1/3} \frac{\hbar}{k_B} v_0 \quad (4)$$

where  $N/V$  is the number of atoms per unit volume,  $v_0$  is an average sound velocity given by

$$\frac{1}{v_0^3} = \frac{1}{3} \left[ \frac{1}{v_l^3} + \frac{2}{v_t^3} \right] \quad (5)$$

and the longitudinal  $v_l$  and transverse  $v_t$  sound velocities are calculated from equation 3 and

$$v_t = \sqrt{\frac{C_{44}}{\rho}} \quad (6)$$

In these equations  $\rho$  is the density,  $T$  is the temperature and  $k_B$  is Boltzmann's constant. Using the room temperature values to calculate  $v_0$  gives a Debye temperature of  $\theta_D = 229.5$  K. The Debye temperature for  $ZrV_2$  has been reported in

earlier studies as  $\theta_D = 233 \text{ K}$ <sup>24</sup> and  $\theta_D = 219 \text{ K}$ <sup>9</sup>. For comparison the Debye temperatures of the constituent elements are: Zr (212.13 K cubic, 293.2 K hexagonal), and V ( 388.8 K)<sup>25</sup>.

## 6.4 Conclusions

The temperature dependence of the elastic constants of polycrystalline  $\text{ZrV}_2$  was measured in the temperature range 100-300 K. The elastic constants exhibit anomalous behavior over this temperature range, but do not exhibit discontinuities in the second derivative of the free energy with respect to strain (elastic constants), evidence that the phase transition from the C15 cubic to rhombohedral form is second-order. The lack of hysteresis in the temperature dependence of the resonant frequencies when warmed and cooled provides additional evidence of the second-order nature of the phase transition. Ultrasonic loss was measured for the first resonant frequency and displays a peak centered at the transition temperature,  $T_m$ . Differences in the values of the some of the quantities reported here, such as Young's modulus and longitudinal sound velocity at the phase transition temperature, and those reported in earlier studies are attributed to the higher accuracy of the RUS technique compared to earlier techniques and differences in material preparation and annealing methods. Calculations of the Debye temperature using room temperature elastic constants agree well with results published by earlier studies.

## References

- <sup>1</sup> A.C. Lawson, Phys. Lett., **36A** (1), 8 (1971).
- <sup>2</sup> C. Geibel, W. Goldacker, H. Keiber, V. Oestreich, H. Rietschel, and H. Wühl, Phys. Rev. B, **30** (11), 6363-6367 (1984).
- <sup>3</sup> D.P. Shoemaker and C.B. Shoemaker, J. Less-Common Metals **68**, 43 (1979).
- <sup>4</sup> Ö. Rapp and G. Benediktsson, Phys. Lett., **74A** (6), 449-452 (1979).
- <sup>5</sup> T.R. Finlayson, E.J. Lanston, M.A. Simpson, E.E. Gibbs and T.F. Smith, J. Phys. F: Metal Phys., **8** (11), 2269-2278 (1978).
- <sup>6</sup> D.E. Moncton, Solid State Comm., **13**, 1779-1782 (1973).
- <sup>7</sup> M. Levison, C. Zahradnik, R. Bergh, M.L.A. MacVicar and J. Bostock, Phys. Rev. Lett., **41** (13), 899-903 (1978).
- <sup>8</sup> E.M. Gololobov, V.F. Malishevskii, Zh.M. Tomilo, and P.A. Kofman, Inorganic Mat., **18** (11), 1580-1582 (1982).
- <sup>9</sup> Ö. Rapp and L.J. Vieland, Phys. Letters, **36A**, 369 (1971).
- <sup>10</sup> J.E. Doherty and D.F. Gibbons, Phys. Stat. Sol. (b), **44**, K5 (1971).
- <sup>11</sup> M. Levison, C. Zahradnik, R. Bergh, M.L.A. MacVicar, and J. Bostock, Phys. Rev. Lett., **41** (13), 899-902 (1978).
- <sup>12</sup> V.M. Pan, I.E. Bulakh, A.L. Kasatkin and A.D. Shevchenko, J. Less-Common Metals, **62**, 157-166 (1978).
- <sup>13</sup> K. Otsuka and C.M. Wayman, *Shape Memory Materials*, K. Otsuka and C.M. Wayman, eds. (Cambridge University Press, Cambridge; New York, 1998).
- <sup>14</sup> P. Haasen, *Physical Metallurgy*, (Cambridge University Press, Cambridge; New York, 1996).
- <sup>15</sup> <http://www.tulane.edu/~sanelson/eens211/twinning.htm>.
- <sup>16</sup> [http://en.wikipedia.org/wiki/Crystal\\_twinning](http://en.wikipedia.org/wiki/Crystal_twinning).
- <sup>17</sup> <http://www.msm.cam.ac.uk/phase-trans/2002/encyclopedia.article.2001.pdf>.
- <sup>18</sup> H.K.D.H Bhadeshia, *Worked Examples in the Geometry of Crystals*, (Institute of Materials, London, 2001), 51-69.
- <sup>19</sup> [http://en.wikipedia.org/wiki/Shape\\_memory\\_alloy](http://en.wikipedia.org/wiki/Shape_memory_alloy).
- <sup>20</sup> F. Chu, T.E. Mitchell, S.P. Chen, M.Sob, M. Sob, R. Siegl, and D.P.Pope, J. of Phase Equil., **18** (6), 536-543 (1997).
- <sup>21</sup> T.M. Brill, S. Mittelbach, W. Assmus, M. Müllner, and B. Lüthi, J. Phys.: Condens. Matter, **3**, 9621-9627 (1991).
- <sup>22</sup> R.G. Leisure, S. Kern, F.R. Drymiotis, H. Ledbetter, A. Migliori and J.A. Mydosh, Phys. Rev. Lett. **95**, 075506 (2005).
- <sup>23</sup> R.G. Leisure, K. Foster, J.E. Hightower, and D.S. Agosta, Materials Science and Engineering A **370**, 34 (2004).
- <sup>24</sup> T. Takashima and H. Hayashii, Japan J. Appl. Phys., **12** (10), 1659-1660 (1973)
- <sup>25</sup> H. Ledbetter and S. Kim in , *Handbook of elastic properties of solids, liquids, and gases*, Vol. II, M. Levy, H.E. Bass, and R.R. Stern, eds. (Academic Press, San Diego, 2001), Chapter 7.

## **Chapter 7**

### **Conclusions**

The experimental technique Resonant Ultrasound Spectroscopy (RUS) was used to examine the elastic and anelastic properties of several novel materials. The results presented here demonstrate the strength of RUS in working with materials that other techniques, which are used to determine elastic constants and measure ultrasonic loss, may not be able to accommodate. Nanocrystalline and quasicrystalline materials are difficult to produce, and the amount of material available to make a sample is often small. The sample making technique used in RUS was extended in this study to be able to handle very small sample sizes and to work with samples that are sensitive to high temperature. This study also demonstrates the ability of RUS to extract information on internal processes such as structural phase transitions, and details such as activation energy for anelastic processes.

Materials with very fine grain sizes, nanocrystals, are currently a very active area of research. Average grain sizes of 100 nm or less have a significant impact on the physical properties of these materials and modern technological advances in engineering, medicine and other areas have been designed to take advantage of some of these properties. The very small sample size necessitated by the difficulty in producing large amounts of many of the nanocrystalline forms has forced new

procedures for sample preparation to be developed. Grain growth in nanocrystals exposed to ambient temperatures for long periods of time or when heated made water-soluble, room temperature adhesives in the polishing process mandatory. Construction of new shim sets and adaptation of the wet polishing technique to dry polishing were also necessary.

RUS was used to measure the elastic constants of nanocrystalline palladium (nc-Pd) and silicon-stabilized nanocrystalline palladium (nc-PdSi) in the temperature range 4-300K. The results for nc-Pd were compared to earlier measurements of the bulk modulus and Young's modulus for similar nanocrystalline forms of Pd. The values presented in this study for the elastic moduli are in good agreement with earlier studies. Differences in the reported moduli can be attributed to the larger grain size in my samples (80-100 nm vs. 5-15 nm), and to possible differences in the production and thermal history of the material.

These results were also compared to the polycrystalline averages for Pd, calculated from the single crystal values. Lower values for the elastic moduli are predicted due to the increased contribution of the grain boundaries where the atomic density is lower than in the interior of the grains. The measured bulk modulus for nc-Pd is 35.1-40.0% lower than corresponding values calculated for polycrystalline Pd. The measured shear modulus is 17.8-18.6% lower than pc-Pd.

The elastic moduli for nc-Pd exhibit significant anelastic effects, while the elastic moduli for nc-PdSi do not. A loss peak centered near 264 K in nc-Pd is suppressed in nc-PdSi, indicating the loss mechanisms are due to grain boundary effects. It is expected that the production method for nc-PdSi results in nanometer

scale grains of Pd with small grains of Si in the intergrain space, resulting in suppressions of grain sliding and grain reorientation. The center frequency of the loss peaks show a temperature shift, with higher frequency peak centered at higher temperatures, indicating a thermally activated process. An attempt frequency calculated from curve fitting of a loss peak and the temperature dependence of a resonant frequency, is attributed to a distribution of coupled loss mechanisms with different activation energies due to differing local atomic environments at the grain surfaces.

Quasicrystalline materials have been called a new form of condensed matter. These materials exhibit perfect long-range translational order but exhibit an aperiodic structure. These structures produce rotational symmetries (5-fold, 8-fold, 10-fold, 12-fold) that are forbidden by standard periodic structures. RUS was used to measure the elastic constants of an icosahedral  $\text{Ti}_{39.5}\text{Zr}_{39.5}\text{Ni}_{21}$  quasicrystal over the temperature range 3-292K. The results were in general agreement with earlier ultrasonically-derived values for *i*-phase  $\text{Ti}_{41.5}\text{Zr}_{41.5}\text{Ni}_{17}$ . In particular, the room-temperature values for the Young's modulus, the shear modulus, and Poisson's ratio are in general agreement with the earlier ultrasonic results, but differ strongly from reported results on similar materials obtained by pressure-volume measurements and conventional mechanical testing. The reason for this disagreement is unknown. In comparison to many other *i*-phase materials, the ultrasonic measurements show that the TiZrNi materials have a low shear modulus to bulk modulus ratio, and a high Poisson's ratio. These results suggest that the interatomic bonding in the TiZrNi materials differs substantially from that in many of the other *i*-phase materials. A

Debye temperature of 316.7 K was calculated from the low-temperature elastic constants, which permits the calculation of the long-wavelength acoustic contribution to the heat capacity. The internal friction increases rather strongly in the temperature range of 150 – 300 K, suggestive of a thermally activated process. Further measurements at higher temperatures are needed to explore this effect.

RUS was also used to measure the elastic constants and ultrasonic loss in a random alloy, a metallic compound which does not exhibit chemical ordering of its component atoms; any lattice position in a random alloy may be inhabited by any of the chemical species comprising the compound. The temperature dependence of the elastic constants of the bcc  $\text{Ta}_{0.33}\text{V}_{0.67}$  random alloy was measured in the temperature range 5-300 K. These results were compared to similar studies of Laves-phase C15  $\text{TaV}_2$ . The temperature dependence of the bulk modulus of bcc  $\text{Ta}_{0.33}\text{V}_{0.67}$  exhibits strong agreement with the semi-empirical Varshni expression, while the shear modulus and Young's modulus deviate significantly from this theoretical curve. This behavior is attributed to the anomalous behavior of the  $C_{44}$  elastic constant due to electronic effects. Laves-phase C15  $\text{TaV}_2$  also exhibits an anomalous temperature dependence of  $G$  and  $E$ , but where  $\text{TaV}_2$  exhibits a decreasing modulus with decreasing temperature, bcc  $\text{Ta}_{0.33}\text{V}_{0.67}$  exhibits an increasing modulus with decreasing temperature. The symmetries found in the C15 structure, which produce doubly degenerate electron energy levels very close to the Fermi level, do not exist in bcc  $\text{Ta}_{0.33}\text{V}_{0.67}$ . The electronic effects which strongly impact the  $C_{44}$  elastic constant in C15  $\text{TaV}_2$  are highly suppressed in the random alloy form, resulting in a

temperature dependence of the shear and Young's moduli that are only slightly anomalous and which display a more normal behavior.

The bcc form is also able to absorb almost three times as much hydrogen than the Laves-phase C15 form. Ultrasonic loss associated with the movements of hydrogen atoms between interstitial tetrahedral sites is observed for bcc  $\text{Ta}_{0.33}\text{V}_{0.67}\text{H}_{0.045}$  in the 170 K temperature region, and is not observed for bcc  $\text{Ta}_{0.33}\text{V}_{0.67}$ . The ultrasonic loss is attributed to the Snoek effect. The loss peaks for  $\text{TaV}_2\text{H}_{0.06}$  occur near 250 K, indicating a faster motion for hydrogen in the bcc random alloy. The results presented here, obtained from measurements made with the Resonant Ultrasound Spectroscopy technique, contribute to the basic understanding of the properties of nanocrystals, quasicrystals and random alloys. All of these types of materials have application to modern technologies, and new applications of these materials are announced almost every month. The accuracy of the results presented here is high and demonstrate the strength of RUS as an experimental technique for the study of elastic properties and ultrasonic loss in a variety of materials.

## Appendix 1

### Derivation of the modulus defect

A perfectly elastic material will not exhibit internal friction, since stress and strain are always in phase. Elastic scattering will shift resonance frequencies but does not remove energy from the system and will therefore not affect the  $Q$  of the resonance. If the response of a strain to an applied stress does not reach equilibrium instantaneously, the material deviates from perfect elasticity and is anelastic. Real materials exhibit a combination of elastic and anelastic responses to stress <sup>1</sup>. In a real material, anelastic effects lead to the conversion of vibrational energy into thermal energy of the lattice, producing ultrasonic loss. Analeastic loss mechanisms include thermoelasticity, stress relaxation across grain boundaries, and stress-induced ordering. The modulus defect is defined as the change in the elastic moduli due to anelasticity <sup>2</sup>.

Anharmonic corrections to the harmonic approximation of the generalized Hooke's Law are required to explain some physical phenomena <sup>3</sup>:

- the behavior of specific heat at high temperature
- broadening of inelastic neutron scattering peaks
- thermal expansion
- temperature dependence of elastic constants
- thermal conductivity

Consider the generalized Hooke's Law for a solid:

$$\sigma_{ij} = \sum_{ijkl} c_{ijkl} \varepsilon_{kl} \quad (1)$$

Now consider a single stress  $\sigma$ , corresponding to a single strain  $\varepsilon$  and the associated elastic constant  $c$ :

$$\sigma = c\varepsilon \quad (2)$$

In a perfect crystal,  $\sigma$  and  $\varepsilon$  are always in phase -  $\varepsilon$  responds instantaneously to  $\sigma$ , and there is no loss. In a real crystal, there is usually a time delay in the response due to the movement of a defect due to the strain, or movement of a light interstitial atom.

We can modify the stress-strain relation to include a simple exponential relaxation with a single relaxation time  $\tau$ <sup>4</sup>.

$$\sigma + \tau \frac{d\sigma}{dt} = c_R \varepsilon + c_U \frac{d\varepsilon}{dt} \quad (3)$$

where  $c_R$  is the relaxed elastic constant and  $c_U$  is the unrelaxed elastic constant. If we apply a sinusoidal stress

$$\sigma(\omega, t) = \sigma(\omega) e^{i\omega t} \quad (4)$$

then

$$\varepsilon(\omega, t) = \varepsilon(\omega) e^{i\omega t} \quad (5)$$

Substitution of equations 4 and 5 into equation 3 yields

$$\sigma(\omega) = \left[ c_U + \frac{c_R - c_U}{1 + \omega^2 \tau^2} + i(c_U - c_R) \frac{\omega \tau}{1 + \omega^2 \tau^2} \right] \varepsilon(\omega) = c^*(\omega) \varepsilon(\omega) \quad (6)$$

In the limit  $\omega\tau \ll 1$ , the stress and strain are in phase and the relaxed elastic constant describes the material. In the limit  $\omega\tau \gg 1$ , the material cannot respond

instantaneously to the stress and the unrelaxed elastic constant describes the material.

Between these two limits, the elastic constant is complex.

It can be shown <sup>4</sup> that the loss,  $Q^{-1}$ , is given by

$$Q^{-1} = \frac{\text{Im}(c^*(\omega))}{\text{Re}(c^*(\omega))} = \frac{\Delta c}{c_U} \frac{\omega\tau}{1 + \omega^2\tau^2} \quad (7)$$

where  $\Delta c = c_U - c_R$ .  $Q^{-1}$  approaches zero in the limits  $\omega\tau \ll 1$  and  $\omega\tau \gg 1$ , and is a maximum for  $\omega\tau = 1$ .

When an interstitial atom moves to another interstitial site, or an atom moves into a lattice vacancy, the frequency of these moves can be described by the Arrhenius relation

$$f = f_0 e^{-\frac{E_A}{k_B T}} \quad (8)$$

where  $E_A$  is the activation energy and  $f_0$  is the attempt rate. For the hopping of interstitial atoms,  $E_A$  is the energy required for the atom to pass over the potential barrier and reach the next interstitial site. For atom-vacancy exchange,  $E_A$  is the barrier energy plus the energy to form a vacancy. Re-writing equation 8 in terms of the relaxation time, and expressing  $E_A$  in units of degrees K

$$\tau = \tau_0 e^{\frac{E_A}{T}} \quad (9)$$

where  $\tau_0$  is the time between attempts. Defining  $T_C$  as the temperature at which the loss is a maximum, we substitute equation 9 into the condition  $\omega\tau = 1$ , and re-arrange terms to obtain

$$\ln(\omega) = -E_A \left( \frac{1}{T_C} \right) - \ln(\tau_0) \quad (10)$$

which is linear in  $1/T_C$ . The slope of the curve obtained by plotting  $\ln(\omega)$  vs.  $1/T_C$  gives the activation energy.

The loss causes a frequency dependent change in the real part of the elastic constant <sup>4</sup>, as illustrated by figure A1.1. Rearranging the terms of the real part of equation 6 yields

$$\delta c = \frac{(c_U - c_R)\omega^2\tau^2}{1 + \omega^2\tau^2} \quad (11)$$

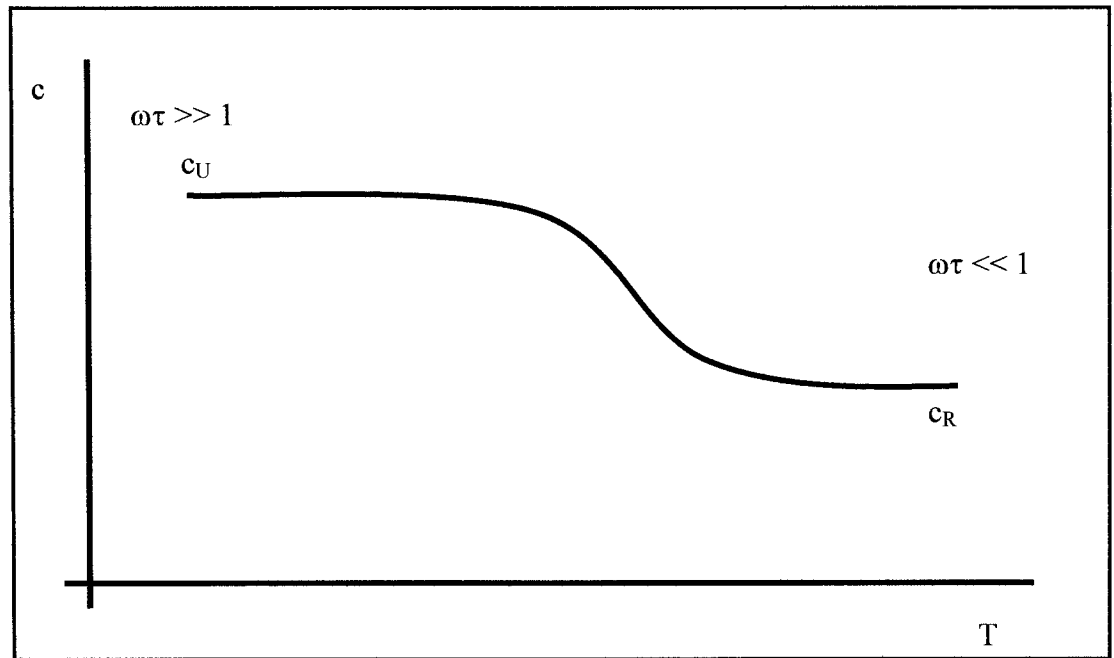


Fig. A1.1 Theoretical temperature dependence of an arbitrary elastic constant, based on equation 11, for a material exhibiting the modulus defect over an arbitrary temperature range.

A change is also seen in the temperature dependence of the resonant frequencies.

Starting from  $f \propto \sqrt{\frac{c}{\rho}}$ , the frequency change is given by

$$\delta f = \frac{f}{2} \frac{\Delta c}{c} \frac{\omega^2\tau^2}{1 + \omega^2\tau^2} \quad (12)$$

The value that is calculated for the attempt time,  $\tau_0$ , is sometimes too short to represent a physical process. This is attributed to a distribution of coupled relaxation mechanisms with different activation energies and attempt frequencies. To simulate slightly different environments experienced by atoms participating in the loss process, a Gaussian distribution of activation energies is used.

$$G(E, E_A, \sigma) = \frac{1}{\sigma\sqrt{\pi}} e^{-\left(\frac{E-E_A}{\sigma}\right)^2} \quad (13)$$

The loss curve is fit using

$$Q^{-1}(T, E_A, \sigma) = \int_{E-5\sigma}^{E+5\sigma} \left(\frac{\Delta c}{c}\right) \frac{\omega\tau(T, E)G(E, E_A, \sigma)}{1 + \omega^2\tau^2(T, E)} dE \quad (14)$$

The frequency fit can be refined using

$$f(T, E_A, \sigma) = \int_{E-5\sigma}^{E+5\sigma} \left(\frac{f_0}{2}\right) \left(\frac{\Delta c}{c}\right) \frac{\omega^2\tau^2(T, E)G(E, E_A, \sigma)}{1 + \omega^2\tau^2(T, E)} dE \quad (15)$$

---

<sup>1</sup> A.S Nowick and B.S. Berry, *Anelastic Relaxation in Crystalline Solids*, Academic Press, New York (1972)

<sup>2</sup> A.S. Nowick in *Progress in Metal Physics Volume 4*, edited by Bruce Chalmers, Pergamon Press LTD, London (1953)

<sup>3</sup> N.W. Ashcroft and N.D. Mermin, *Solid State Physics*, 417-488, Harcourt Brace & Co., Orlando (1976)

<sup>4</sup> R.G. Leisure in *Resonant Ultrasound Spectroscopy*, 137, Wiley, New York (1977)

## Appendix 2

### Isotropy of *i*-phase Quasicrystals

In this appendix I prove that materials with icosahedral symmetry are elastically isotropic. If we represent the elastic constants of a material with icosahedral symmetry, and with respect to a Cartesian coordinate system, in matrix form as  $C_{ijkl}$ , we can restate the elastic constants with respect to rotated set of axes by applying a suitable set of rotation matrices.

$$C_{abcd} = \sum \alpha_{ai} \alpha_{bj} \alpha_{ck} \alpha_{dl} C_{ijkl} \quad (1)$$

A rotation of  $2\pi/5$  about any 5-fold axis is represented by the direction cosines. If we choose the 5-fold axis which is at an angle of  $\tan^{-1}(1/\tau)$  from the  $x$ -axis in the  $xy$ -plane the direction cosines are given by<sup>1</sup>

$$\alpha_{xy} = \frac{1}{2} \begin{pmatrix} \tau & -1/\tau & 1 \\ -1/\tau & 1 & \tau \\ -1 & -\tau & 1/\tau \end{pmatrix} \quad (2)$$

where  $\tau$  is the golden mean and is given by

$$\tau = \frac{\sqrt{5} + 1}{2}$$

To show that materials with icosahedral symmetry are elastically isotropic, I will assume that an elastic constant,  $C_{11}$ , is invariant under such a rotation, and show that the transformation yields elastic constants that are consistent with elastic

isotropy. Expanding the reduced notation for the subscripts of elastic constants,  $C_{11}$  is  $C_{1111}$ .

$$C_{1111} = \sum_{ijkl} \alpha_{1i} \alpha_{1j} \alpha_{1k} \alpha_{1l} C_{ijkl} \quad (3)$$

Performing the sums, expanding all terms, and re-introducing the reduced notation yields a large expression involving the sums of the products of  $\alpha_{ij}$  ( $i, j = 1, 2, 3$ ) and  $C_{kl}$  ( $k, l = 1, 2, 3, 4, 5, 6$ ). Since the 2-fold and 3-fold axes of a cube can be aligned with the 2-fold and 3-fold axes of an icosahedron, an icosahedral solid must have at least cubic symmetry. We can therefore reduce the number of independent elastic constants to three

$$C_{11} = C_{22} = C_{33} \quad C_{44} = C_{55} = C_{66}$$

$$C_{12} = C_{21} = C_{13} = C_{31} = C_{23} = C_{32}$$

with all of the other elastic constants equal to zero. Applying these conditions yields

$$C_{11} = \frac{1}{16} \left[ \tau^4 + \frac{1}{\tau^4} + 1 \right] C_{11} + \frac{1}{8} \left[ 1 + \tau^2 + \frac{1}{\tau^2} \right] C_{12} + \frac{1}{4} \left[ 1 + \tau^2 + \frac{1}{\tau^2} \right] C_{44} \quad (4)$$

It can be shown that  $\tau$  has the following properties:

$$\frac{1}{\tau} = \tau - 1 \quad \text{and} \quad \tau^2 = \tau + 1$$

Applying these properties to equation (4) yields

$$C_{12} = C_{11} - 2C_{44}$$

This is the same relationship between these elastic constants that exists for elastically isotropic materials, since only two independent elastic constants are required.

QED

---

<sup>1</sup> P.S. Spoor and J.D. Maynard in , *Handbook of elastic properties of solids, liquids, and gases*, Vol. II, M. Levy, H.E. Bass, and R.R. Stern, eds. (Academic Press, San Diego, 2001), Chapt. 9.

## **Appendix 3**

### **Transducer Assembly Construction**

One of the key components of the Resonant Ultrasound Spectroscopy experimental setup is the transducer assembly. These components are subject to wear and breakage due to their fragile nature and the necessity to physically move the upper assembly during sample mounting. As samples are mounted and removed, the conducting coating of the upper transducer surface experiences scratching and wear which can increase background signal strength.

Figure A3.1 documents the components of the transducer assembly. The first step in the construction is to build the inner tube. Wooden tubes have been used successfully in the cryostat, but may not be suitable for oven rigs. Recent constructions use Phenolic rods which work well at both high and low temperatures. The diameter of the inner tube is selected to be slightly larger than the diameter of the transducer. The thin rods are drilled through the central axis, and the channel diameter must be large enough to allow the Gortex coaxial cable to pass freely through the tube. A shallow countersink of the end of the inner tube that holds the transducer will improve stability and alignment during the transducer mounting portion of the construction.

The outer conducting tube is selected such that the inner tube fits snugly within it. The length of the outer tube is also usually slightly shorter than the inner

tube, and the transducer end of the inner tube extends out of the outer tube to insure that the transducer face extends beyond the supporting assembly. The outer tube is eventually electrically connected to ground with either conducting silver paint or conducting epoxy and preparation of the outer tube surface may be needed to insure a good electrical connection.

The electrical signals are carried by Gortex-insulated coaxial cable. When cutting a length of cable, 3-4 inches of excess length is sufficient for threading the cable and attaching the connections, and allows for correction of a badly mounted transducer. Stripping the cable is difficult; the outer coating is clear Teflon and the braid is hard to distinguish from the Gortex surrounding the inner conductor. I use an Exacto knife to strip the coax. The goal is to expose enough of the center conductor to allow a small crimp or loop to attach to the bottom transducer surface, and to bring the braided conductor out of the bottom end of the outer conducting tube. At the point where the stripped section ends, gently press the dull side of the knife against the coax and slide the blade along the coax to flatten and loosen the outer coating. As this step is repeated, turning the coax by about 90° each time, the outer coating will eventually crack and separate, and can be removed. The braided conductor is now gently pushed down, separated slightly, and twisted together.

The connection of the center conductor to the transducer face is a difficult process due to the very small components involved. A good assembly requires that the center conductor is attached so that it is as perpendicular to the transducer face as possible so that the transducer face is not badly tilted in the final assembly. The attachment is accomplished using conducting epoxy, which must be cured in the oven

or on a hot plate. John Adams has developed a procedure that works very well. His documentation is included below:

- a. The signal wire is bare and can be coiled with a pig tail coil perpendicular to the wire axis. The diameter of the coil should be about half of the transducers diameter so that it can be centered and attached without being too close to the side of the transducer leading to a short.
- b. Attach the wire to a fairly long thin rod (I use the long wood sticks in the lab) with masking tape.
- c. Set up a stage with a demonstration rod with two clamp arms attached next to the hot plate. Put the thin rod with wire vertical in the two clamps, keeping the bare coiled end down.
- d. Before heating up the hot plate place a thick iron shim (because they are clean, hot plate is sticky with wax) on the top and place chosen transducer on top of the shim. The transducer and the coiled wire can be brought together at this point to ensure they are aligned properly and the coil sits flat.
- e. Raise the stage lifting the coiled wire up high enough to apply epoxy to the wire. With a single bristled brush one can apply the already mixed conducting epoxy. A dab of epoxy on the end of the bristle is easily drawn through the coiled wire. This leaves the dab neatly on the

paint to leak to the inside of the tube and electrically short the transducer. I usually allow the Stycast to thicken for 2-3 hours to reduce the chance it will flow over the transducer face, and apply it with a single hair paint brush or very thin wire. The goal is to seal the edge of the transducer completely, and hold it in place. A small amount of epoxy on the transducer face is acceptable. If epoxy needs to be removed from the transducer face, it may be gently brushed with an acetone-soaked Q-tip or thin brush, then cleaned with distilled water. This process may eventually wear off the transducer's coatings, so it should only be done if necessary and it is better to avoid it if possible. The Stycast requires at least 24 hours to cure.

The braided outer conductor is connected to the outer conducting tube using the conducting epoxy. The assembly is cured in the oven; consult the epoxy data sheets for appropriate curing times and temperatures. The upper transducer face is also electrically connected to the outer tube using conducting silver paint (the conducting epoxy is too thick to produce a smooth surface). Test the electrical connections after the silver paint dries to insure that the top and bottom transducer faces are not electrically connected. If silver paint has leaked to the interior, the assembly may be salvaged by removing the silver paint in a small beaker of acetone placed in the ultrasonic cleaner, then resealing the transducer/tube interface before repainting. Periodic repainting of the transducer faces will help maintain low background signal levels.

The current room temperature and oven rigs in the CSU Ultrasonics Lab were built using commercially built pinducer assemblies. While these assemblies produce good signals and eliminate the need for the assembly process outlined here, there is

no information available from the manufacturer as to the epoxies and solders used in the construction. The effect of high and low temperature on the pinducers will need to be determined by trial and error.

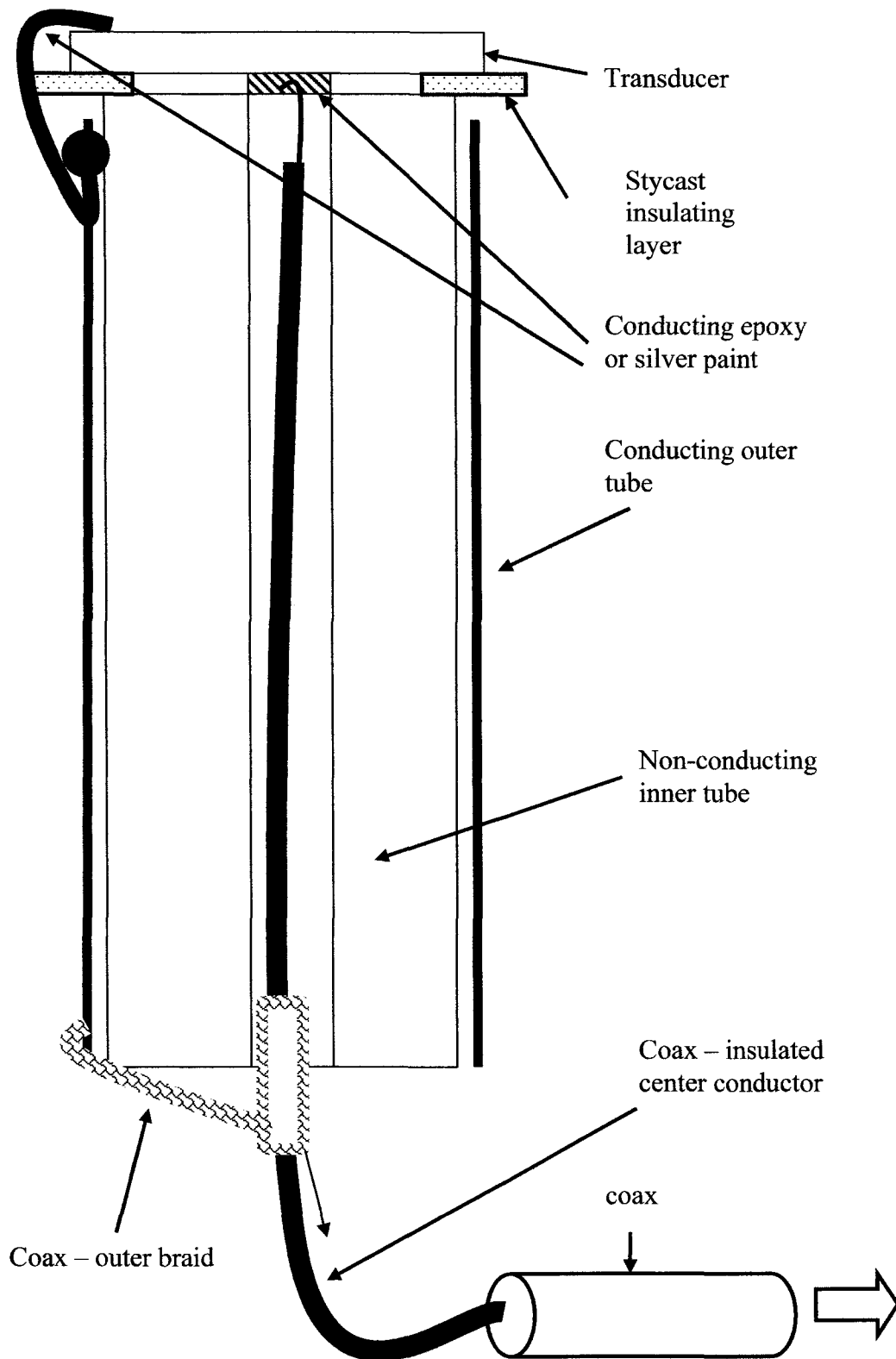


Figure A3.1 Transducer assembly.

